

*What we observe is not nature herself,
But nature exposed to our method of questioning.*

--Werner Heisenberg

*Lord, grant me the Serenity to accept the things I cannot change,
Courage to change the things I can,
and Wisdom to know the difference.*

--Reinhold Niebuhr

University of Alberta

Study of Anisotropic Surface Property of Phyllosilicates by
Atomic Force Microscopy

by

Lujie Yan

A thesis submitted to the Faculty of Graduate Studies and Research
in partial fulfillment of the requirements for the degree of

Doctor of Philosophy

in

Chemical Engineering

Department of Chemical and Materials Engineering

© Lujie Yan
Fall 2013
Edmonton, Alberta

Permission is hereby granted to the University of Alberta Libraries to reproduce single copies of this thesis and to lend or sell such copies for private, scholarly or scientific research purposes only. Where the thesis is converted to, or otherwise made available in digital form, the University of Alberta will advise potential users of the thesis of these terms.

The author reserves all other publication and other rights in association with the copyright in the thesis and, except as herein before provided, neither the thesis nor any substantial portion thereof may be printed or otherwise reproduced in any material form whatsoever without the author's prior written permission.

Abstract

The phyllosilicates are an important class of valuable industrial minerals and play an essential role in many disciplines. The surface properties of phyllosilicate minerals are a topic of crucial importance as they directly affect all industrial aspects in mineral processing. The objective of this research is to investigate the anisotropic surface properties of selected phyllosilicate minerals, focusing on surface charging properties of their basal planes and edge surfaces, and their related particle interactions and rheological properties of particle suspensions.

An ultramicrotome cutting technique was developed to prepare molecularly smooth edge surfaces of phyllosilicates, which allows direct measurement of interaction forces between AFM tips and the prepared surfaces in various electrolyte solutions.

A theoretical model based on the geometry of AFM tip was used to fit the measured force profiles to the classical DLVO theory at different boundary conditions, which allows direct determination of Stern potentials of different phyllosilicate surfaces.

The surface charging behavior of muscovite and talc basal planes and edge surfaces was determined as a function of pH. The basal planes of both muscovite and talc were found to carry a pH-independent permanent negative charge, while the charges on their edge surfaces were highly pH-dependent. The effect of the concentration of two divalent cations: Mg^{2+} and Ca^{2+} on the Stern potential of

different surfaces of phyllosilicate minerals was investigated. The interaction energies of various associations between talc surfaces, such as basal plane-basal plane, edge-edge and basal plane-edge were calculated using the Stern potential values of talc basal planes and edge surfaces obtained from fitting the measured force profiles to the classical DLVO theory. The attractive interaction between talc basal planes and edge surfaces was found to dominate the rheological behavior of talc suspensions.

The findings from this dissertation are anticipated to provide a basis for understanding the colloidal behavior of phyllosilicates in mineral processing and hence better control their process performance.

Acknowledgements

I would like to express my sincere gratitude and appreciation to my supervisors Professor Zhenghe Xu and Professor Jacob H. Masliyah for providing me this great opportunity to fulfill my PhD study overseas. Their invaluable guidance and insistence on excellence enabled me to attain my research goals. It is such a privilege for me to be one of their students.

Many thanks go to Dr. Helmut Gnägi at Diatome Ltd in Switzerland, a guru in microtome cutting technique, for his willingness to test my mineral samples and provide valuable technical advice and discussion on sample preparation and microtome cutting procedure which really facilitated the progress of this project.

I would like to thank Dr. Ming Chen of University of Alberta for his generously sharing the recipe of resin used in sample preparation for microtome cutting and giving the glass knifemaker equipment to our lab to make knives used in microtome cutting.

My gratitude goes to Dr. Shihong Xu for his assistance in SEM imaging and his willingness to help me out when I came to him with some problems of Matlab program in developing the theoretical model and data fitting.

My appreciation goes to Dr. Jingyi Wang for her assistance in contact angle measurement, Dr. Alexander Englert, Dr. Hongying Zhao and Ms. Shaiu-yin Wu for sharing their experiences with AFM at the first stage of my research.

Thanks are also extended to Professor Jan D. Miller at the University of Utah and Professor John Ralston at the University of South Australia for their insightful suggestions during our discussions about my project.

I acknowledge Ms. Lisa Carreiro and Mr. Jim Skwarok for their assistance in managing facilities and recourses.

The financial support from Natural Sciences and Engineering Research Council (NSERC) industrial Research Chair in Oil Sands Engineering is acknowledged.

My deepest gratitude goes to my parents in China. Thanks for their understanding and support on all decisions I have made in my life. Their precious love and absolute faith in me are always my motivation to move forward. Thanks for all friends I met here after I arrived in Canada, especially one of my best, Wei Guo for sharing with me over these years and helping pull me through when the going was tough.

Table of Contents

Chapter 1 Introduction	1
1.1 Mineralogy of phyllosilicates.....	1
1.2 Anisotropic surface properties of phyllosilicates.....	4
1.3 Aims and objectives	6
1.4 Organization of the dissertation	7
1.5 References.....	10
Chapter 2 Literature review.....	11
2.1 Interactions between two surfaces	11
2.1.1 DLVO theory.....	11
2.1.2 Van der Waals interactions	12
2.1.3 Electrostatic double layer interaction.....	12
2.1.4 Derjaguin approximation	16
2.1.5 The effect of surface roughness	20
2.2 Particle association and rheological property	19
2.3 Surface charging characteristic of phyllosilicates.....	23
2.3.1 Zeta potential measurement	24
2.3.2 Potentiometric titration	26
2.3.3 Sum frequency generation spectroscopy.....	27
2.3.4 Atomic force microscopy.....	28
2.4 References.....	32
Chapter 3 Materials, characterization and methods.....	37
3.1 Materials	37
3.2 Preparation of different phyllosilicate surfaces	37

3.2.1	Ultramicrotome cutting technique	37
3.2.2	Characterization of prepared surfaces.....	39
3.3	AFM.....	41
3.3.1	The principle of the AFM	41
3.3.2	AFM imaging.....	42
3.3.3	AFM force measurement	43
3.3.4	AFM tip evaluation	46
3.4	Theoretical model for DLVO calculation	48
3.5	References.....	53

Chapter 4 Determination of anisotropic surface charging characteristics of different phyllosilicates by direct force measurements: Effect of pH.....54

4.1	Introduction.....	54
4.2	Results and discussion	56
4.2.1	Interactions between AFM tip and silica surfaces.....	56
4.2.2	Interactions between AFM tip and talc surfaces	59
4.2.3	Interactions between AFM tip and muscovite surfaces	64
4.2.4	PZC and protonation reactions of different phyllosilicate edge surfaces.....	69
4.3	Summary	74
4.4	References.....	75

Chapter 5 Interaction of divalent cations with basal planes and edge surfaces of phyllosilicate minerals.....78

5.1	Introduction.....	78
5.2	Results and discussion	81
5.2.1	Interactions between AFM tip and silica surfaces	81

5.2.2	Interactions between AFM tip and different muscovite surfaces	86
5.2.3	Interactions between AFM tip and different talc surfaces	89
5.2.4	Stern potentials of different muscovite and talc surfaces	93
5.2.5	Anisotropic surface character of phyllosilicates	95
5.2.6	Effect of different divalent cations.....	98
5.3	Summary	100
5.4	References	102

**Chapter 6 Understanding suspension rheology of phyllosilicates
from direct force measurement using AFM104**

6.1	Introduction.....	104
6.2	Results and discussion	107
6.2.1	Tip calibration	107
6.2.2	Interactions between AFM tip and different talc surfaces	109
6.2.3	Interaction energy between different talc surfaces.....	112
6.2.4	Predicting rheology of talc suspensions.....	115
6.3	Summary	117
6.4	References	119

**Chapter 7 Adsorption and conformation of polysaccharide on
anisotropic phyllosilicates: Effect of ionic strength.....120**

7.1	Introduction.....	120
7.2	Experimental	125
7.2.1	Polysaccharide solution.	125
7.2.2	AFM imaging	126
7.3	Results and discussion	128
7.3.1	Characteristics of CMC.....	128

7.3.2 CMC adsorption on talc basal planes.....	130
7.3.3 CMC adsorption on talc edge surfaces	135
7.3.4 CMC adsorption on silica surfaces	138
7.4 Summary	143
7.5 References.....	144
Chapter 8 Summary	147
8.1 General conclusions	147
8.2 Contributions to original knowledge	149
8.3 Recommendations for further work.....	150
Appendix A Deposition of phyllosilicate particle suspensions.....	151
Appendix B Estimation of surface energy of different phyllosilicate surfaces	155
B.1 Good & Van Oss model	155
B.2 Three-probe-liquid contact angle measurement.....	155
B.3 References	157
Appendix C AFM images of CMC adsorbed onto muscovite basal planes.....	158

List of Figures

Figure 1.1 Crystalline structures of typical phyllosilicates: (a) kaolinite; (b) talc and (c) muscovite	3
Figure 1.2 Schematics of anisotropic phyllosilicate surfaces	4
Figure 1.3 Schematics of the surface groups populating on (a) muscovite and (b) talc basal planes and edge surfaces	5
Figure 2.1 Schematics of an electrical double layer of a charged surface.	13
Figure 2.2 Schematics of the Derjaguin approximation	17
Figure 2.3 Schematics of applying the SEI method to a smooth colloidal probe and rough plate in AFM colloidal probe technique.....	19
Figure 2.4 Modes of particle association in phyllosilicate suspensions: (a) dispersed; (b) face-to-face (FF); (c) edge-to-face (EF) and (d) edge-to-edge (EE)	22
Figure 2.5 Schematics of the effect of pH on the yield stress in terms of particle associations of phyllosilicate minerals.....	23
Figure 3.1 Schematics of preparing the phyllosilicate edge surfaces by the ultramicrotome cutting technique	37
Figure 3.2 Typical FE-SEM images of the talc edge surface prepared by the ultramicrotome cutting technique: (a) taken with lower area resolution but larger scanning area; and (b) taken by zooming in on a small smooth area at a high resolution.	40
Figure 3.3 XPS spectra of talc and muscovite (a) basal plane and (b) edge surface	41
Figure 3.4 Schematics of the components in an AFM experiment	42
Figure 3.5 Typical AFM force curves: (a) “force vs. piezo displacement” curves recorded by AFM and (b) “force vs. separation distance” force profiles converted from (a).	44
Figure 3.6 Typical FE-SEM images of an AFM silicon nitride tip used in this study: (a) plane view; (b) oblique view; and (b1) scanning auger electron spectroscopy analysis on the top end of the tip.....	47

Figure 3.7 Geometry of a model conical AFM tip with spherical apex used for DLVO calculations.....	50
Figure 4.1 Typical (a) AFM image of silica wafer and (b) interaction forces measured between a silicon nitride tip and silica wafer in 1 mM KCl solutions at pH 5.6, 7.9 and 9.9.....	56
Figure 4.2 Comparison of Stern potential values of silicon nitride, determined by fitting of AFM-force profiles, with ζ potential values determined by electrophoresis method	59
Figure 4.3 Typical AFM images of a prepared hydrophobic talc basal plane and an edge surface: (a) Talc basal plane with a mean roughness of 0.355 nm (Rq) over 4 μm^2 ; (b) Talc edge surface with a mean roughness of 0.723 nm (Rq) over 4 μm^2	60
Figure 4.4 Typical interaction force curves (a) between AFM tip and hydrophobic talc basal plane, and (b) between the tip and hydrophilic talc edge surface, measured in 1 mM KCl solutions of different pH values.....	61
Figure 4.5 Comparison of Stern potential values determined in this study by AFM with ζ potential values from Reference for talc (a) basal plane and (b) edge surface.	63
Figure 4.6 Typical AFM images of phyllosilicate planes prepared by microtome cutting technique: (a) muscovite basal plane with a mean roughness of 0.221 nm (Rq) over 4 μm^2 ; (b) muscovite edge surface with a mean roughness of 0.569 nm (Rq) over 4 μm^2	65
Figure 4.7 Typical AFM interaction force curves measured between a tip and muscovite (a) basal plane and (b) edge surface in 1 mM KCl solutions of various pH values.....	68
Figure 5.1 ζ potential of silica particles in 1 mM KCl solutions containing various concentrations of (a) Ca^{2+} and (b) Mg^{2+} at around pH 8.5, determined by electrophoresis method.	82
Figure 5.2 Typical AFM interaction force profiles measured between the AFM silicon nitride tip and the silica wafer surface in 1 mM KCl solutions containing various concentrations of (a) Ca^{2+} and (b) Mg^{2+} at pH 8.5.....	83

Figure 5.3 Comparison of the Stern potential values of AFM silicon nitride tip determined by fitting of AFM-force profiles with ζ potential values determined for silicon nitride nano particles by electrophoresis method in 1 mM KCl solutions containing various concentrations of (a) Ca^{2+} and (b) Mg^{2+} at pH 8.5.....	85
Figure 5.4 Typical AFM interaction force profiles measured between AFM tip and muscovite basal planes in 1 mM KCl solution of various (a) Ca^{2+} and (b) Mg^{2+} concentrations at pH 8.5.....	87
Figure 5.5 Typical AFM interaction force profiles measured between AFM tip and muscovite edge planes in 1 mM KCl solutions containing (a) Ca^{2+} and (b) Mg^{2+} at pH 8.5	88
Figure 5.6 Typical AFM interaction force profiles measured between AFM tip and talc basal planes in 1 mM KCl solutions of various (a) Ca^{2+} and (b) Mg^{2+} concentrations at pH 8.5.	91
Figure 5.7 Typical AFM interaction force profiles measured between AFM tip and talc edge surfaces in 1 mM KCl solutions of various (a) Ca^{2+} and (b) Mg^{2+} concentrations at pH 8.5	92
Figure 5.8 Stern potentials of (a) muscovite and (b) talc basal plane and edge surfaces in 1 mM KCl solution of different Ca^{2+} and Mg^{2+} concentrations at pH 8.5, obtained by fitting the measured AFM force profiles to the classical DLVO theory.....	94
Figure 6.1 (a) Average zeta potential values of talc particles in KCl solutions measured by electrophoresis methods taken from literature; (b) The total interaction energy per unit area of talc particles at different pH in 1 mM KCl solutions calculated using DLVO theory and measured average zeta potential values; (c) The yield stress data of talc particles at different pH in KCl solutions taken from literature	106
Figure 6.2 Typical interaction force profiles measured between AFM tip and silica wafer in 1 mM KCl solutions of different pH values	108
Figure 6.3 Typical force profiles measured between tip and talc (a) basal planes and (b) edge surfaces in 1 mM KCl solutions as a function of aqueous solution pH	111

Figure 6.4 Stern potentials of talc basal planes and edge surfaces extracted by fitting the measured force profiles to the classical DLVO theory.	112
Figure 6.5 The calculated total interaction energy per unit area of various associations of talc surfaces in 1 mM KCl solutions at different pH using Stern potential values derived from AFM colloid probe force measurement and DLVO fit.	113
Figure 7.1 Image processing for determination of CMC coverage on the surface by using Image J: (a) the original AFM image and (b) the corresponding binary (black and white) image for calculation of surface coverage.	127
Figure 7.2 The structure of CMC.	128
Figure 7.3 (a) ζ potentials and (b) corresponding radius of gyration of CMC solutions of different ionic strengths at pH 9.	130
Figure 7.4 In situ AFM images of CMC (50 ppm) adsorbed onto talc basal planes in KCl solutions at pH 9 of different ionic strengths: (a) 1 mM; (b) 10 mM and (c) 100 mM.	133
Figure 7.5 In situ AFM images of CMC (50 ppm) adsorbed onto talc edge surfaces in solutions at pH 9 of different ionic strengths: (a) 1 mM; (b) 10 mM and (c) 100 mM.	136
Figure 7.6 In situ AFM images of CMC (50 ppm) adsorbed onto the silica surface in solutions of pH 9 at different ionic strengths: (a) 1 mM KCl; (b) 10 mM KCl and (c) 100 mM KCl.	141
Figure 7.7 Summary of surface coverage and apparent layer thickness of adsorbed CMC on different surfaces in KCl solutions of different ionic strengths at pH 9.	142
Figure A.1 Schematics of muscovite sheet coated with phyllosilicate particles for microtome cutting and the proposed view of cross section.	151
Figure A.2 SEM images of kaolinite particles deposited on muscovite substrate: (a) large area at low resolution and (b) small area at high resolution.	152
Figure A.3 SEM images of illite particles deposited on muscovite substrate: (a) large area at low resolution and (b) small area at high resolution.	153

Figure A.4 SEM images of montmorillonite particles deposited on muscovite substrate: (a) large area at low resolution and (b) small area at high resolution.....	154
Figure C.1 In situ AFM images of CMC (50 ppm) adsorbed onto muscovite basal planes in KCl solutions at pH 9 of different ionic strengths: (a) 1 mM; (b) 10 mM and (c) 100 mM	158

List of Tables

Table 1.1 Classification of phyllosilicate minerals.	2
Table 2.1 Summary of reported IEP (determined by ζ potential measurements), PZC (determined by potentiometric titration method) and maximum yield stress of phyllosilicates.	21
Table 3.1 The values used for calculation of Hamaker constant A_H	48
Table 4.1 Comparison of best-fitted Stern potential values of silica obtained in this study with corresponding literature values obtained by microelectrophoresis (MEP), streaming potential (SP) and fitting of AFM force profiles.	58
Table 4.2 Comparison of best-fitted Stern potential values of the muscovite basal plane with literature values of mica obtained by microelectrophoresis (MEP) and streaming potential (SP) measurements, and AFM fitting.....	69
Table 4.3 Possible surface groups on muscovite and talc edgesurfaces and corresponding protonation constants ($\log K_H$).....	71
Table 6.1 Comparison of Stern potential, obtained by best-fit of interaction force profiles between a silicon nitrate tip and silica wafer measured using AFM colloid probe force technique with the classical DLVO theory, with corresponding literature values obtained by microelectrophoresis (MEP), streaming potential (SP) and AFM force curve fitting.	109
Table 7.1 R_q surface roughness, apparent layer thickness (PTV distance) and surface coverage of adsorbed CMC (50 ppm) on talc basal planes in KCl solutions of different ionic strengths at pH 9	134
Table 7.2 Contact angles of bare talc basal planes and in the presence of adsorbed CMC (50 ppm) in KCl solutions of different ionic strengths at pH 9.	134
Table 7.3 R_q surface roughness, apparent layer thickness (PTV distance) and surface coverage of adsorbed CMC (50 ppm) on talc edge surfaces in KCl solutions of different ionic strengths at pH 9	137

Table 7.4 Rq surface roughness, apparent layer thickness (PTV distance) and surface coverage of adsorbed CMC (50 ppm) on silica surfaces in KCl solutions of different ionic strengths at pH 9	142
Table B.1 Three probe liquids for measuring the surface energy of phyllosilicates.	142
Table B.2 Contact angles of three probe liquids on different surfaces.	156
Table B.3 Surface energy of different surfaces	156
Table C.1 Rq surface roughness, apparent layer thickness (PTV distance) and surface coverage of adsorbed CMC (50 ppm) on muscovite basal planes in KCl solutions of different ionic strengths at pH 9	159

Nomenclature

U_{Total}	total interaction energy per unit area, J/m ²
U_{VDW}	Van der waals interaction energy per unit area, J/m ²
U_{EDL}	electrostatic interaction energy per unit area, J/m ²
A_H	Hamaker constant, J
ϵ_i	static dielectric constant for materials i
n_i	refractive index for materials i
h	Planck's constant, 6.63×10^{-34} J · S
ν_e	electronic absorption frequency of material, Hz
ψ_s	surface potential, V
ψ_d	Stern potential, V
ζ	zeta potential, V
ψ	electronic potential, V
e	elementary charge, 1.6×10^{-19} C
k_B	Boltzmann constant, 1.38×10^{-23} J/K
T	absolute temperature, K
κ^{-1}	Debye length, m
D	distance, m
F_{EDL}	electrostatic interaction force, N
U	interaction energy per unit area between two bodies of arbitrary shape, J/m ²
$U_A(x)$	interaction energy between two planar plates separated by a gap x, J/m ²

$n \cdot k / n \cdot k $	angle of the curved surface of the body
τ_Y	yield stress, Pa
K_{struc}	network structural factor
ε	relative permittivity of a medium, C/mV
ε_0	permittivity of vacuum, 8.85×10^{-12} C/mV
σ	surface charge density, C/m ²
F_a	Faraday's constant, 9.65×10^4 C/mol
c_a	amount of acid titrant, mol/L
c_b	amount of base titrant, mol/L
c_0	number density of the ions in the bulk
F	interaction force, N

Chapter 1

Introduction

Silicate minerals are the most abundant rock-forming minerals on earth. The phyllosilicates (sheet silicates), as an important class of valuable industrial minerals, play an essential role in many disciplines such as biotechnology, paper making, cosmetics, food processing, tailings management, and processing and utilization of natural resources.

To fundamentally understand the colloidal behaviour of phyllosilicate minerals, it is necessary to study the surface properties of phyllosilicates under various physicochemical conditions of practical relevance. During the past decades, many efforts have been devoted to understanding surface properties of phyllosilicates in relation to their mineral processing. However, due to their small sizes and distinct anisotropic surface character, some of crucial surface properties of phyllosilicates, especially in terms of specific faces, remain unclear.

1.1 Mineralogy of phyllosilicates

The principal structural elements of phyllosilicate are tetrahedral sheet (T) and octahedral sheet (O). T is composed of silicon-oxygen tetrahedron linked to the neighboring tetrahedron by sharing three corners to form a hexagonal network while the fourth corner of each tetrahedron (the apical oxygen) points into and forms part of the adjacent octahedral sheet. O is in the sixfold coordination with oxygens from the tetrahedral sheet and hydroxyl group while individual octahedral is linked laterally by sharing edges.

Based on different layer structure and interlayer cations, phyllosilicates consist of micas, talc, chlorite, serpentine, and clay minerals. The typical mineral in each group with their chemical formulas are shown in Table 1.1 [1-2].

Table 1.1 Classification of phyllosilicate minerals

Mineral group		Typical mineral	Chemical formula
Trilayer (TOT)	Talc-Pyrophyllite	Talc	$Mg_3Si_4O_{10}(OH)_2$
	Mica	Muscovite	$KAl_2(AlSi_3O_{10})(OH)_2$
		Illite	$(K, H_3O)(Al, Mg, Fe)_2(Si, Al)_4O_{10}[(OH)_2, (H_2O)]$
	Chlorite	Clinochlore	$(Mg_5 Al)(AlSi_3)O_{10}(OH)_8$
	Smectite	Montmorillonite	$(Ca, Na)_{0.33}(Al, Mg)_2(Si, Al)_4O_{10}(OH)_2 \cdot nH_2O$
	Vermiculite	Vermiculite	$(Mg, Fe, Al)_3(Al, Si)_4O_{10}(OH)_2 \cdot 4H_2O$
Bilayer (TO)	Kaolinite	Kaolinite	$Al_2Si_2O_5(OH)_4$
	Serpentine	Chrysotile	$Mg_3Si_2O_5(OH)_4$

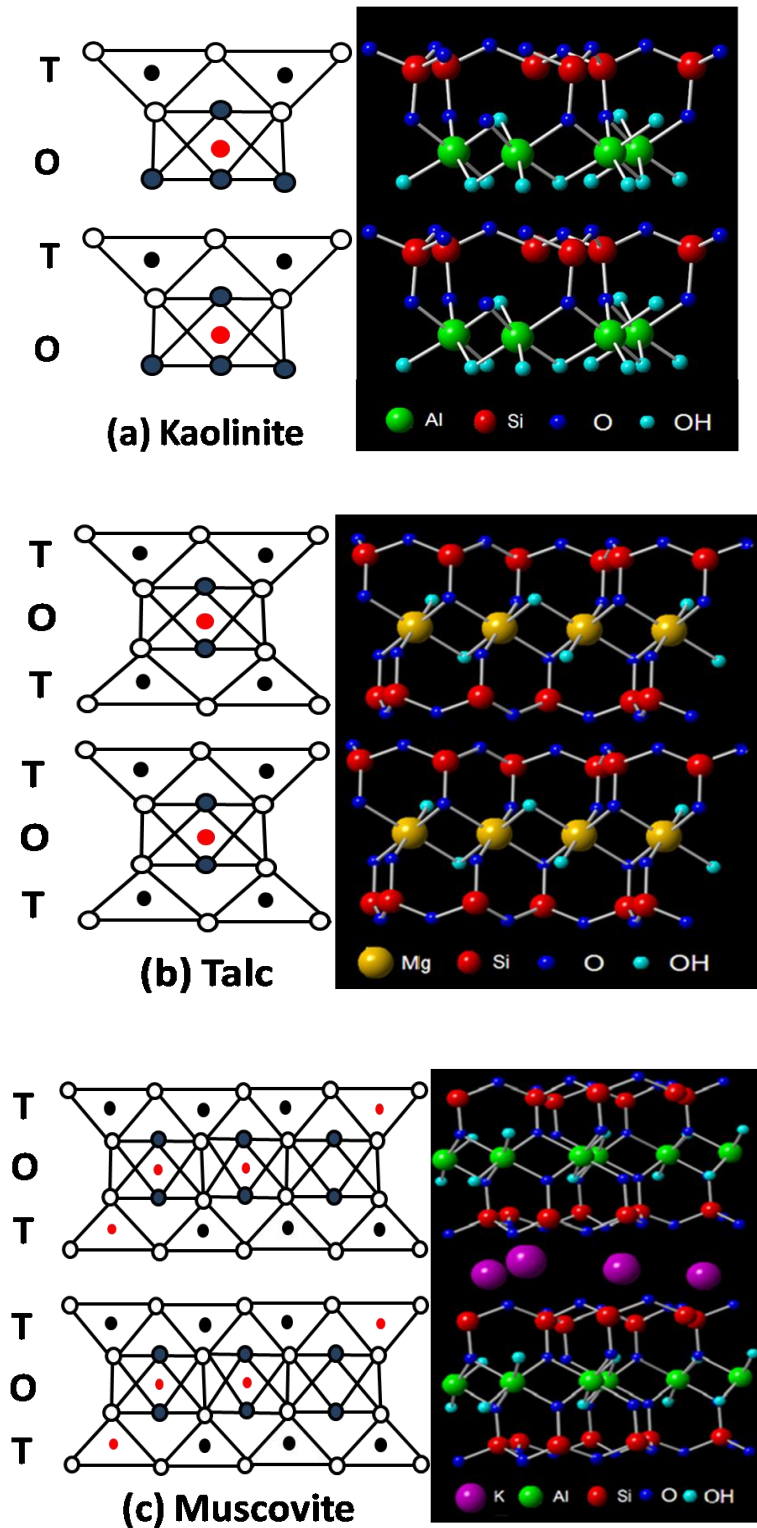


Figure 1.1 Crystalline structures of typical phyllosilicates: (a) kaolinite; (b) talc and (c) muscovite

The individual layers may be joined to each other in a phyllosilicate crystallite by interlayer cations, van der Waals forces, electrostatic forces, and/or by hydrogen bonding [1]. As a typical bilayer (TO) phyllosilicate, the structure of kaolinite is shown in Figure 1.1 (a). Each bilayer sheet of kaolinite is joined by strong hydrogen bonds. The structures of two trilayer (TOT) phyllosilicates (talc and muscovite) are shown in Figure 1.1 (b and c). The elementary sheet of talc consists of a brucite-like O layer sandwiched between two identical silicon-oxygen T layers and each TOT of talc is hold together by van der Waals forces without interlayer cations. The elementary sheet of muscovite consists of a gibbsite-like O layer sandwiched between two T layers. $1/4$ Si^{4+} ions in the T are substituted by Al^{3+} , resulting in negative charges on the T basal plane. Those negative charges are balanced by interlayer K^+ ions.

1.2 Anisotropic surface properties of phyllosilicates

Due to their layered structure, phyllosilicate minerals consist of two types of surfaces: the basal plane and the edge surface, as depicted in Figure 1.2.

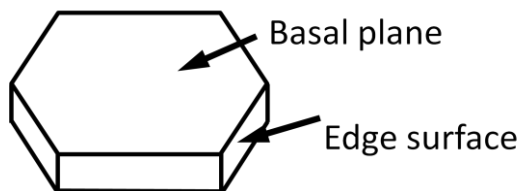


Figure 1.2 Schematics of anisotropic phyllosilicate surfaces

Different surface groups populate on each type of surfaces, which makes phyllosilicate minerals show distinct anisotropic surface properties. We will take two symmetrical TOT layer phyllosilicates (muscovite and talc) as the simplest case for illustration. The siloxane structure ($-\text{Si}-\text{O}-\text{Si}-$) on the T layer has an extremely low affinity for protons in aqueous media over a moderate pH range.

Therefore, this surface group is difficult to be hydrolyzed and estimated to be essentially inert [2]. The basal plane of phyllosilicates is mainly charged by the fixed and permanent isomorphous substitution, which is the replacement of one higher valence atom by lower valence atom of similar size in a crystal lattice without disrupting or changing the crystal structure of the mineral. This substitution can occur at T layer where the Si^{4+} is replaced by Al^{3+} or O layer where Al^{3+} is replaced by divalent or monovalent metal ions such as Mg^{2+} , Fe^{2+} and Zn^{2+} [1, 3]. Both substitutions cause an excess of negative charges on the surface, which are fixed and independent of the physicochemical conditions in the surrounding medium. The degree of isomorphous substitution may vary from mineral to mineral and determines how negatively charged the surfaces are. As shown in Figure 1.3 (a_1), a very high degree of substitution presents on T layer of the muscovite basal plane due to $1/4 \text{Si}^{4+}$ ions are substituted by Al^{3+} , which results in a strongly negatively charged and highly hydrophilic muscovite basal plane with a contact angle of water close to zero [1]. Talc basal plane is usually almost neutral or only slightly negatively charged due to the low degree of substitution as shown in Figure 1.3 (b_1). As a result, the basal plane of talc is fairly hydrophobic with a contact angle of water close to 64° [4].

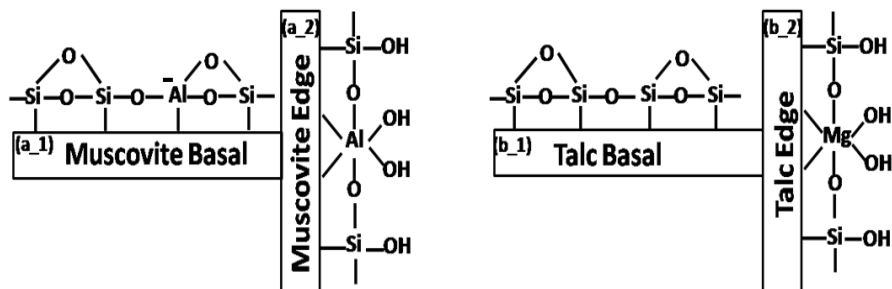
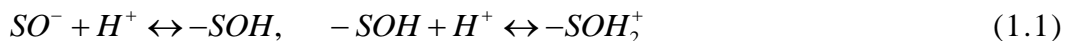


Figure 1.3 Schematics of surface groups populating on basal planes and edge surfaces of (a) muscovite and (b) talc.

On the other hand, unlike the basal plane, the edge surfaces of phyllosilicates are sensitive to the changing of solution pH: positively charged at low pH and negatively charged at high pH. This pH dependent charging behaviour is attributed by amphoteric SOH surface groups on the edge surfaces, which can undergo protonation or deprotonation reactions as expressed in the following equilibria:



As shown in Figure 1.3 (b_1) and (b_2), instead of Al–OH surface group as on the muscovite edge surface, the Mg–OH group populates on the talc edge surface. These two surface species exhibit different protonation constants. Since Mg(OH)₂ has a higher point of zero charge (PZC) value of than Al(OH)₂ of a given pH [5], the talc edge surface is therefore anticipated to be more positively charged than the muscovite edge surface.

Moreover, for more complicated cases, such as kaolinite with asymmetric (TO) structure, besides the different surface properties of basal planes and edge surfaces, a significant difference in both charging behaviour and wettability has been observed on 001 (T) and 00 $\bar{1}$ (O) basal plane surfaces [6, 7].

1.3 Aims and objectives

The overall objective of this study is to develop a methodology which allows us to investigate the anisotropic surface properties of selected phyllosilicates, focusing on muscovite and talc, as representatives of aluminum and magnesium phyllosilicate, respectively. More specific objectives are to:

- develop a technique suitable to prepare smooth edge surfaces of phyllosilicates for probing the surface property at molecular level;

- directly measure the colloidal interaction forces between the probe and basal or edge surfaces of different phyllosilicates using atomic force microscopy (AFM);
- quantitatively evaluate surface charge characteristics of phyllosilicate basal planes and edge surfaces by developing a suitable model to fit the measured interaction forces to theory at different boundary conditions (BC);
- investigate the effect of water chemistry of solutions, including pH and divalent cation concentration on the surface charging behaviour of different phyllosilicates basal planes and edge surfaces;
- predict the interaction energies for various associations between different phyllosilicate surfaces based on the AFM derived electrical surface (Stern) potential of each surface and to interpret the rheology properties of phyllosilicate mineral suspensions;

It is expected that this fundamental research on anisotropic surface properties of phyllosilicates will provide a basis for understanding their colloidal behaviour in mineral processing.

1.4 Organization of the dissertation

The next chapter (Chapter 2) includes a literature review on background and recent research reported in literature on anisotropic surface charge properties of phyllosilicates. The first part concentrates on reviewing theories and governing equations of interactions in colloidal systems, including classical DLVO (Derjaguin -Landau-Verwey - Overbeek) theory, the origin and quantitative expressions of colloidal interactions. The second part focuses on reviewing the previous published work on anisotropic surface charge properties of

phyllosilicates, based on analytical techniques such as electrophoresis, titration, sum frequency generation (SFG) spectroscopy and AFM.

Chapter 3 gives a description on materials and principal methods used during this study. The method to prepare sufficiently smooth edge surfaces of phyllosilicates employing ultramicrotome cutting technique is introduced. As a predominantly adopted experimental technique to investigate the surface property of phyllosilicate surfaces in this study, AFM is introduced in detail in the context of its principles and major functions. The theoretical model developed for interpreting the measured interaction force profiles to surface (Stern) potential of phyllosilicate surfaces is presented as well.

In Chapter 4, followed the methodology presented in Chapter 3, a systematic study on the effect of solution pH on the interaction forces between AFM tip and different phyllosilicate surfaces is discussed. The colloidal forces between the silicon nitride tip and basal planes or edge surfaces are measured using an AFM in simple electrolyte (1 mM KCl) solutions as a function of pH. The Stern potential of the basal planes and edge surfaces in each case is obtained by fitting the measured force profiles with the classical DLVO theory.

Chapter 5 presents a systematic study on the interaction of divalent cations, both Ca^{2+} and Mg^{2+} with basal planes and edge surfaces of phyllosilicate minerals. The colloidal interaction forces between AFM tip and basal planes or edge surfaces are measured using AFM in simple electrolyte (1 mM KCl) solutions of pH 8.5 as a function of divalent cation concentrations. The Stern potential of the basal plane and edge surface in each case is obtained by fitting the measured force profiles with the classical DLVO theory.

In Chapter 6, interaction energies of various associations between anisotropic talc surfaces are calculated using AFM-derived Stern potential values of talc basal planes and edge surfaces. The different interactions between talc basal planes and edge surfaces are discussed in the context of understanding rheological behaviour of talc suspensions.

Chapter 7 presents some preliminary results on polymer adsorption on different talc surfaces.

Chapter 8 summaries the work presented in the dissertation and gives suggestions of future work.

1.5 References

- [1] Bergaya, F., Theng, B. K. G., Lagaly, G., 2006, "Handbook of Clay Science," Elsevier, Amsterdam, London.
- [2] Bleam, W., Welhouse, G., Janowiak, M., 1993, "The Surface Coulomb Energy and Proton Coulomb Potentials of Pyrophyllite (010), (110), (100), and (130) Edges," *Clays and Clay Minerals*, 41(3) pp. 305-316.
- [3] Van Olphen, H., 1963, "An Introduction to Clay Colloid Chemistry, for Clay Technologists, Geologists, and Soil Scientists," Interscience Publishers, New York.
- [4] Nalaskowski, J., Abdul, B., Du, H., Miller, J. D., 2007, "Anisotropic Character of Talc Surfaces as Revealed by Streaming Potential Measurements, Atomic Force Microscopy, Molecular Dynamics Simulations and Contact Angle Measurements," *Canadian Metallurgical Quarterly*, 46(3) pp. 227-235.
- [5] Parks, G. A., 1965, "The Isoelectric Points of Solid Oxides, Solid Hydroxides, and Aqueous Hydroxo Complex Systems," *Chemical Reviews*, 65(2) pp. 177-198.
- [6] Gupta, V., Miller, J. D., 2010, "Surface Force Measurements at the Basal Planes of Ordered Kaolinite Particles," *Journal of Colloid and Interface Science*, 344(2) pp. 362-371.
- [7] Yin, X., Gupta, V., Du, H., Miller, J. D., 2012, "Surface Charge and Wetting Characteristics of Layered Silicate Minerals," *Advances in Colloid and Interface Science*, 179-182 pp. 43-50.

Chapter 2

Literature review

The surface properties of phyllosilicates are very important in minerals processing. For instance, the electrical surface charges of phyllosilicate can significantly influence the separation efficiency in mineral flotation. In this chapter, the background of fundamental colloidal interaction principles and their respective governing equations related to this dissertation work are introduced first, followed by a review on recent study on phyllosilicate minerals with regard to their surface charge characteristics.

2.1 Interactions between two surfaces

The stability of fine-grained mineral suspensions is determined largely by the colloidal interactions between mineral particles. The long range colloidal force is in control when two surfaces approaching each other while the adhesive force (pull off force) corresponds to the strength where the two surfaces are attached to each other.

2.1.1 DLVO theory

The overall interaction (U_{Total}) between two macroscopic bodies is usually determined in terms of interaction free energies. In classical DLVO theory, the fundamental colloidal interactions consist of two terms: the van der Waals (U_{VDW}) interactions and the electrostatic double layer (U_{EDL}) interaction as [1]:

$$U_{Total} = U_{VDW} + U_{EDL} \quad (2.1)$$

2.1.2 Van der Waals interactions

The molecular van der Waals (VDW) interactions which exist between any surfaces in any medium are the combination of three long range interaction terms: dispersion (London) between two induced dipoles created by fluctuation of electronic charges, orientation (Keesom) between two permanent dipoles and induction (Debye) between a permanent dipole and an induced dipole. These three interaction energies are all decaying with distance between two surfaces. The VDW interaction energy per unit area between two parallel surfaces at separation distance D , U_{VDW} can be calculated by [1, 2]:

$$U_{VDW} = -\frac{A_H}{12\pi D^2} \quad (2.2)$$

The characteristic constant A_H , also known as the Hamaker constant, can be calculated from the dielectric properties of interacting surfaces and the intervening medium. In the macroscopic method, A_H can be determined by non-retarded Lifshitz formula for material 1 interacting with material 2 across medium 3 as [3]:

$$A_H = \frac{3}{4} k_B T \left(\frac{\varepsilon_1 - \varepsilon_3}{\varepsilon_1 + \varepsilon_3} \right) \left(\frac{\varepsilon_2 - \varepsilon_3}{\varepsilon_2 + \varepsilon_3} \right) + \frac{3hV_e}{8\sqrt{2}} \frac{(n_1^2 - n_3^2)(n_2^2 - n_3^2)}{\sqrt{n_1^2 + n_3^2} \sqrt{n_2^2 + n_3^2} (\sqrt{n_1^2 + n_3^2} + \sqrt{n_2^2 + n_3^2})} \quad (2.3)$$

where ε_i and n_i are the static dielectric constant and the refractive index for materials i , respectively. h is Planck's constant and V_e is the main electronic absorption frequency in the UV region.

2.1.3 Electrostatic double layer interaction

When a surface is immersed in an electrolyte solution, it usually can be charged by various charging mechanisms such as ionization or dissociation of surface functional groups, isomorphic substitution, or specific adsorption. Taking muscovite as an example, as mentioned in Chapter 1, the basal plane of muscovite

is highly negatively charged due to $1/4 \text{ Si}^{4+}$ ions in the T are substituted by Al^{3+} . On the other hand, the charges of the edge surface can be attributed by the amphoteric Si-OH or Al-OH surface groups on the surface, which can take up a proton to be positively charged or release a proton to be negatively charged.

In the solution, a negatively charged surface is balanced by positively charged counterions and can influence the ion distribution close to it to form a double layer (EDL) structure as depicted in Figure 2.1. The inner layer is called the Stern or Helmholtz layer where the ions are fixed to the surface; the outer layer is the diffuse Gouy-Chapman layer (according to the Stern's model) where ions are in thermal motion [1]. The potential at the shear plane is called zeta potential (ζ potential) which is different in magnitude from the surface potential or Stern potential at the Stern plane (ψ_d).

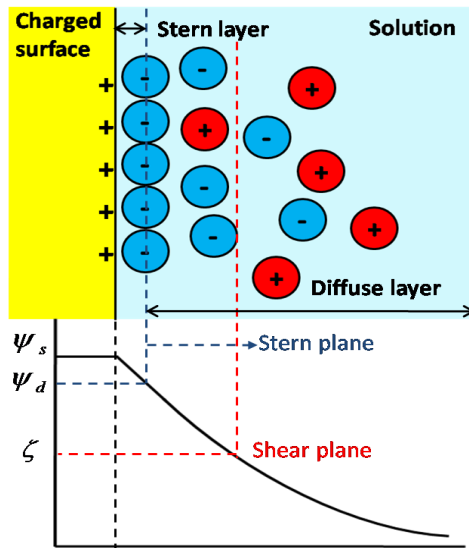


Figure 2.1 Schematics of an electrical double layer of a charged surface. ψ_s is the surface potential of the particle, ψ_d is the Stern potential at the Stern plane and ζ is the zeta potential at the shear plane.

The distribution of electrolyte ions in the diffuse layer obeys Boltzmann's distribution [1]:

$$n_i = n_{i\infty} \exp\left(\frac{-z_i e \psi}{k_B T}\right) \quad (2.4)$$

where n_i is the number density of i th ions with valence z_i , $n_{i\infty}$ is the number density of i th ions in the bulk, ψ is the potential in the EDL, e is the electron charge, k_B is the Boltzmann constant (1.38×10^{-23} J/K) and T is the absolute temperature in Kelvin.

Combining this ion distribution equation (2.4) with the expression of the surface potentials of the electric field originally derived from Maxwell's equation, we can obtain so-called Poisson-Boltzmann (PB) equation:

$$\varepsilon \varepsilon_0 \nabla^2 \psi = -e \sum_i z_i n_{i\infty} \exp\left(\frac{-z_i e \psi}{k_B T}\right) \quad (2.5)$$

where ε and ε_0 are relative permittivity of the medium and the permittivity of vacuum, respectively.

If the potential is small ($\frac{z_i e \psi}{k_B T} \ll 1$), we can assume $\sinh\left(\frac{z_i e \psi}{k_B T}\right) \approx \frac{z_i e \psi}{k_B T}$,

therefore, the non-linear PB equation can be simplified to linearized PB equation which is generally referred to as the Debye-Hückel approximation:

$$\nabla^2 \psi = \kappa^2 \psi \quad (2.6)$$

$$\text{where } \kappa^{-1} = \left(\frac{\varepsilon \varepsilon_0 k_B T}{\sum_i n_{i\infty} e^2 z_i^2} \right)^{1/2} \quad (2.7)$$

The κ^{-1} , known as the Debye length, is a characteristic parameter describing the thickness of the EDL or decay of the electric potential.

When two charged surfaces approach each other, the EDL surrounding each surface starts to overlap which induces the osmotic pressure between two surfaces.

The interaction energy $U_{EDL}(D)$ or force $F_{EDL}(D)$ between two parallel surfaces at separation distance D can be expressed by [1]:

$$U_{EDL}(D) = -\int_{\infty}^D F_{EDL}(h) dh \quad \text{per unit area} \quad (2.8)$$

$$F_{EDL}(D) = k_B T \sum_i n_{i\infty} \left(\exp\left(\frac{-z_i e \psi}{k_B T}\right) - 1 \right) - \frac{\epsilon \epsilon_0}{2} \left(\frac{d\psi}{dx} \right)^2 \quad \text{per unit area} \quad (2.9)$$

In general, surface potential profile, interaction energy and force can be obtained by numerical solution of Equations (2.8) and (2.9) with proper BC.

The selection of BC for the numerical solution depends on charging mechanism of each interacting surface. For example, if the surface charge arises from irreversible adsorption of charged species, dissociation of strong acid/base surface groups or lattice imperfections (such as the isomorphic substitution in phyllosilicates), the surface charge density is independent of the surface potential and the separation distance between two interacting surfaces. In this case, the constant surface charge density BC is more appropriate as the potential-determining ions do not have sufficient time to re-arrange during approaching of two surfaces [4]. On the other hand, if the surface charge arises from reversible ion adsorption, the potential determining ions are able to re-arrange quickly to suit every configuration of interacting surfaces. Therefore, the surface potentials would remain constant when two surfaces approach each other at a slow rate [5]. In this case, the constant surface potential BC is more

appropriate. However, in reality, the surface charge density of ionizable surface is a function of separation distance as the two interacting surfaces approach each other. The assumption of constant charge density and constant surface potential BC constitutes the upper and lower limits of the interaction, respectively. Therefore, a realistic description of the interaction would fall in between these two limits.

2.1.4 Derjaguin approximation

Theoretically, due to its simple geometry, the interaction between two semi-infinite parallel flat surfaces is evaluated in terms of interaction energy using above given equations. However, the actual measurements of interaction forces are conducted with a given geometry other than two semi-infinite parallel plates. Therefore, the influence of geometry on the interaction energy is derived by Derjaguin approximation (DA), which scales the two flat-plates interaction energy per unit area to the corresponding interaction energy between two curved surfaces. As shown in Figure 2.2, the interaction energy per unit area between two bodies of arbitrary shape $U(D)$ at a distance D (distance of closest approach between two surfaces) can be related to the interaction energy $U_A(x)$ between two planar plates which separated by a gap x by equation [6]:

$$U(D) = \int U_A(x) dA \quad (2.10)$$

where dA is the variation of the cross-section area of two real surfaces with increasing separation, and the integration runs over entire cross-sectional area.

White [7] generalized the expression of DA to:

$$U(D) = \frac{2\pi}{\sqrt{\lambda_1 \lambda_2}} \int_D^\infty U(x) dx \quad (2.11)$$

$$\lambda_1 \lambda_2 = \left(\frac{1}{R_1} + \frac{1}{R_2} \right) \left(\frac{1}{R'_1} + \frac{1}{R'_2} \right) + \left(\frac{1}{R_1} - \frac{1}{R'_1} \right) \left(\frac{1}{R_2} - \frac{1}{R'_2} \right) \sin^2 \varphi \quad (2.12)$$

where R_i and R'_i are the principal radii of curvature for the surfaces i evaluated at points of closest approach distance and φ is the angle between the planes spanned by the circles with smaller curvature radii.

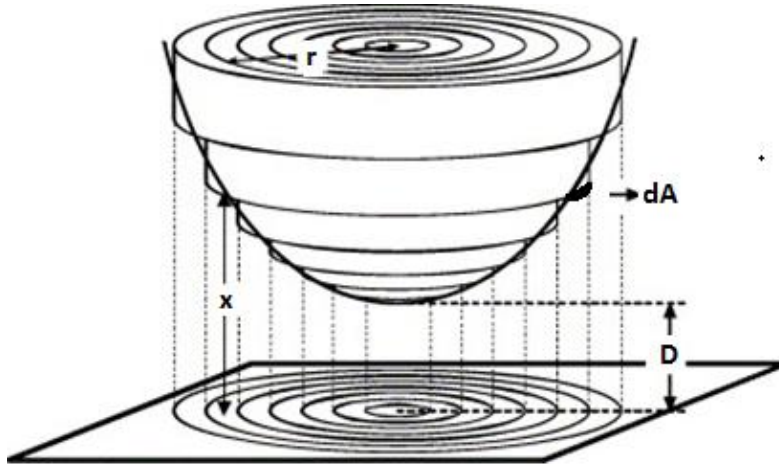


Figure 2.2 Schematics of the DA adapted from literature [6], x is the distance between the planar surfaces and D is the distance between the two considered bodies, r is the radial coordinate.

2.1.5 *The effect of surface roughness*

In DLVO theory, interacting surfaces are assumed to be perfectly smooth with well-defined geometry, which rarely occurs in real colloidal systems. Meanwhile, nearly all studies on morphological heterogeneity demonstrate that the presence of asperities on surfaces can substantially modify interaction energies between two interacting colloidal particles [6, 8-11]. Generally, the surface roughness can cause a significant reduction in the interaction energy, depending on the size of asperities and their densities. The ill-defined surface is the main cause of the discrepancies between theoretical predictions and experimental observations. In

order to avoid the erroneous interpretation from the theory, many efforts have been made to develop some calculation models to incorporate the effect of surface roughness in the calculation of the interaction energy between rough surfaces [6, 8-11].

A common approach for modeling roughness involves random placement of geometrically regular asperities on a smooth surface [8, 11]. Recently surface element integration (SEI) method was developed as an extension of DA to apply to the exact geometry of interacting surfaces [1, 9-12]. By dividing the interacting surface into numerous small elements, SEI computes the total interaction energy between two bodies by numerically integrating the interaction energy per unit area between opposing differential planar elements over the entire surfaces as [1]:

$$U(D) = \iint_A \frac{U_p(H)}{A} \frac{n \cdot k}{|n \cdot k|} dA \quad (2.13)$$

where $U_p(H)/A$ is the interaction energy per unit area between two bodies, A is the projected area of the body normal to the line of closest distance between the bodies. $n \cdot k / |n \cdot k|$ provides a measure of the angle made by the curved surface of the body with the projected normal area A , which is assumed a value of 1 or -1, depending on whether the surfaces of the bodies face each other or they face away from each other.

In this manner, the interaction energy is evaluated in conjunction with realistic geometrical models of surface roughness. Let us take the application of SEI method to AFM colloidal probe technique as an example [12], which is one of most frequently used methods to probe interactions between two surfaces. As depicted in Figure 2.3, the origin of the coordinate system (O) used for

computation of the interaction energy is on the plane of the highest point of the rough surface. All distances are measured along the positive Z -direction in this coordinate system. The minimum separation D is defined as the first sphere-plate contact, i.e., the distance between the smooth plate and the highest point on the rough surface. The actual local separation distance h for each patch of the computing surface is the sum of the separation distance D with the height difference between the local patch and the highest point. The scanned AFM image was reconstructed by dividing the image into numerous tiny meshes and each patch parallel to the mean plane of the surface for computing. Using this recreated surface area, the total energy between the half-space and the rough substrate is computed by integrating the DLVO energy per unit area between the probe and the rough surface at each mesh. This integral is then divided by the projected area to obtain the interaction energy per unit area between the probe and the rough substrate. Details of the SEI method and more applications of this method can be found elsewhere [1, 9-10, 12].

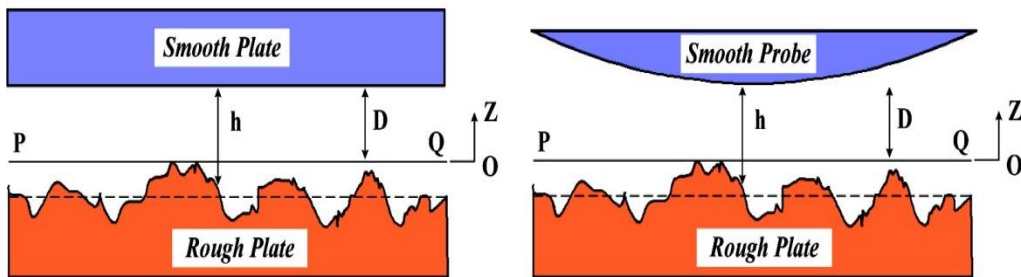


Figure 2.3 Schematics of applying the SEI method to a smooth colloidal probe and rough plate in AFM colloidal probe technique, taken from literature [12].

It should be noted that all analytic solutions, no matter whether it is DA or SEI, have some forms of approximations embedded in it. Therefore, we need to be careful in selecting an expression that is appropriate for a given situation.

2.2 Particle association and rheological property

The rheological property (eg. yield stress or viscosity) of mineral slurries is highly dependent on the properties of the mineral particles in suspension (surface charge, size, shape, concentration, etc.). The charge of mineral surfaces plays a very important role in determining slurry rheology [13-16]. Normally, the rheological properties of mineral suspensions can be predicted by correlating the yield stress τ_Y which is proportional to the mechanical strength of physical network of suspensions with the ζ potential of the particles using the following equation [17]:

$$\tau_Y = K_{struc} \left[\frac{A_H}{12D^2} - \frac{2\pi\epsilon\epsilon_0\kappa e^{-\kappa D} \zeta^2}{1 + e^{-\kappa D}} \right] \quad (2.14)$$

K_{struc} is the network structural term dependent upon the particle size, the solids volume fraction and the mean coordination number; while the two bracketed terms account for the VDW and EDL interactions, respectively.

According to equation (2.14), the maximum yield stress of a mineral suspension occurs at the zero surface potential (or charge) of particles. This is because at the pH value corresponding to this point, there would be no net electrostatic repulsive force between mineral particles and attractive van der Waals interactions will bring and hold particles together, leading to a coagulated state of particles. Based on the above discussion, the isoelectric point (IEP) or PZC of mineral particles is believed to be an important parameter to determine the mechanical properties of mineral suspensions such as shear-yield stress and therefore, is of great interest in mineral processing. For isotropic mineral particles such as quartz or corundum which has a simple and regular morphology and surface charge distribution, the IEP or PZC

across the entire surface of particle is almost identical and occur at the same value. As a result, these values predict to the maximum yield stress of mineral suspensions quite well as well documented in literature [17, 18]. However, the rheological properties of phyllosilicate minerals are hard to be correlated to their IEP or PZC as shown in Table 2.1 [14-15, 18-30].

Table 2.1 Summary of reported IEP (determined by ζ potential measurements), PZC (determined by potentiometric titration method) and maximum yield stress of phyllosilicates.

Phyllosilicate	IEP	Ref	PZC	Ref	Maximum yield stress	Ref
Talc	2.5 <3 3.6	[19] [20] [21]	7.7	[19]	5.6	[19]
Muscovite	1 1.7 5.4 2, 5-7*	[21] [22] [15] [23]	4.6	[15]	5*	[23]
Kaolinite	<2.4 <3 2.9	[24] [18] [22]	4.8 6-6.5	[25] [26]	5.5	[18]
Chlorite	<3 4.5 5.5 2.5-5**	[20] [22] [27] [28]	4.6	[20]	5**	[28]
Chrysotile	3.3	[29]	4.3 8.23	[20] [14]	5.5-9	[14]
Montmorillonite	<3	[22]	6.86	[30]	***	
Vermiculite	3.3	[15]	8.4	[15]		

Note: * IEP value 2 was determined using low solids concentration (0.002 wt. %) suspensions while IEP vary 5-7 using high solids concentration (8-57 wt. %), the maximum yield stress was determined for suspensions of 57 wt. % solids;

** : IEP value 2.5 for low solids concentration 0.05 wt.%, 5 for high solids concentration 8-57 wt.%, the maximum yield stress was determined for suspension of 57 wt.% solids;

*** : For swelling phyllosilicates (smectite or vermiculite), the hydration also plays a dominant role in rheology performance. These two groups usually have relatively low yield stresses as the particles absorb water; therefore, their yield stress data are not included and discussed here.

The apparent discrepancies between these sets of data are that phyllosilicates has unique anisotropic surface character due to their layered structure as described in Chapter 1. As shown in Figure 2.4, various modes of particle associations can occur for phyllosilicates [31]: face (basal)–face (basal) (FF), edge–face (EF) and edge–edge (EE).

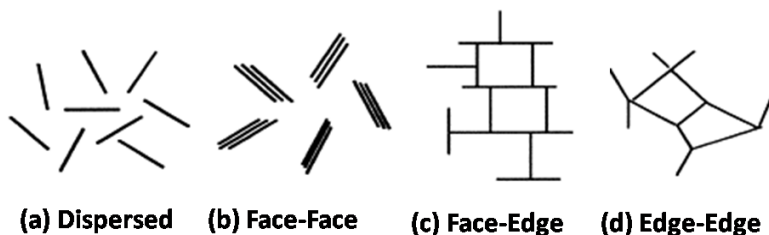


Figure 2.4 Modes of particle associations in phyllosilicate suspensions: (a) dispersed; (b) face-to-face (FF); (c) edge-to-face (EF) and (d) edge-to-edge (EE) adapted from literature [31].

FF association leads to formation of lamellar structured aggregates, which decreases the gel strength of suspensions due to the reduction of available units to build gel structures and the available surface for particle interaction. EF and EE associations can lead to three dimensional voluminous structures which exhibit more complex rheology and difficult to handle. The overall rheological behaviour of phyllosilicate particles depends on the type of particle associations in suspensions, which is affected by the conditions of the solution such as pH or salt concentrations. For example, the effect of pH on the yield stress due to particle

associations of phyllosilicate minerals is shown in Figure 2.5 [32]. EE and EF contacts between phyllosilicate particles form most probably at low pH values. At a somewhat higher pH, the potential between the EE contacts is predominant, which results in the lower yield stress of suspensions. Theoretically, in terms of this proposed interaction model, James and Williams [33] calculated the total interaction energy between kaolinite suspensions at various pH and electrolyte concentrations by representing the edge and face of a kaolinite platelet as a cylinder and a flat plate, respectively. Rheological parameters of flocculated suspensions (extrapolated shear stress and plastic viscosity) of dilute kaolinite suspensions (solid volume fraction of 0.02) are interpreted.

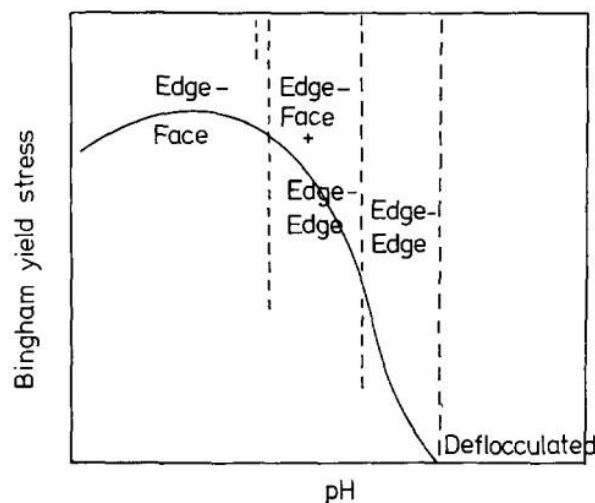


Figure 2.5 Schematics of the effect of pH on the yield stress in terms of particle associations of phyllosilicate minerals adapted from literature [32].

2.3 Surface charging characteristic of phyllosilicates

The surface charges of phyllosilicate minerals govern characteristic chemical and physical phenomena such as ion exchange, adsorption, swelling, colloidal stability, and flow behaviour. Therefore, an extensive and accurate knowledge of the surface charge properties of phyllosilicate is required in order to predict their behaviours.

For the past decades, a number of efforts were made to determine or model the surface charging behaviour of phyllosilicates.

As mentioned in Chapter 1, phyllosilicate minerals exhibit different charge characteristics on different surfaces, being attributed to different prevailing charging mechanisms: fixed and permanent isomorphous substitution on basal plane and hydrolysis reactions of broken primary bonds, mostly on the edge surfaces. The total surface charge of phyllosilicate particle is a combination of charges from both basal planes and edge surfaces. The surface charge properties of phyllosilicate minerals have been extensively investigated using various experimental methods and modeling. In view of the experimental studies, Zeta potential measurements and potentiometric titration are two conventional methods extensively used to investigate the surface charging character of phyllosilicates.

2.3.1 Zeta potential measurement

The zeta potential measurements by electrophoresis are widely used to determine the electrokinetic potentials of minerals. As already shown in Figure 2.1, the ζ potential of particles is the electrical potential at the shear plane when the particles are moving in an aqueous solution under the influence of a given electric field. In electrophoresis method, the electrophoretic mobility of dilute suspensions is measured, which is then converted to ζ potential values by mathematical models. The pH where the ζ potential is zero refers to the IEP.

In early years, Parks compiled the IEP of most metal oxides and hydroxides, which has been commonly used as the reference in the later studies of IEP for many materials [34]. Fuerstenau and Pradip reviewed the study of ζ potential

measurements in the context of the flotation of oxide and silicate minerals [21]. By reviewing studies reported in recent years, Kosmulski updated the data not only on metal oxides and hydroxides but also on lots of pH-dependent charging materials [22, 35]. He pointed out that many publications clearly indicate that $IEP \neq PZC$ for specific materials other than metal oxides. Compared with the PZC, IEP values reported for the same materials (corresponding to certain chemical formula and crystallographic structure) are more consistent, which makes it more suitable to characterize the pH-dependent surface charges of materials.

In most conventional methods of electrophoretic measurements, highly dilute dispersions are required. Recently the dynamic mobility measurement using electroacoustic method was developed. This method can measure ζ potential of concentrated dispersions and has been applied to investigating charge characteristics of the kaolinite and montmorillonite suspensions [17, 36-37] though the theoretical background is still under development [38].

In all electrokinetic methods, the mathematical models used to convert the determined electrophoretic mobility of suspensions to ζ potential values of the surface were derived for spherical or near-spherical particles with a basic assumption that the charges are uniformly distributed on the particle. Until now, there is no well developed theory that can properly describe the movement of platy particles with anisotropic charge characteristics under the influence of a given electric field. Therefore, in the case of phyllosilicate, interpretation of colloidal behaviour based on the ζ potential values determined by the existing electrophoretic measurements could be misleading.

2.3.2 Potentiometric titration

Unlike the electrophoretic method which is affected by the shape of particles, potentiometric titration method is based on the principle of ion exchange in solution, which is independent to the shape of particles. Therefore, this method has been chosen as another main approach to study the electrical surface properties of minerals, especially the phyllosilicates.

By adding a certain amount of acid or base titrant, the surface charge density σ (C/m²) can be calculated, if the surface area A (m²/litre) is known, by:

$$\sigma = \frac{F_a}{A} ([C_a - C_b] - [H^+] + [OH^-]) \quad (2.15)$$

where F_a is the Faraday's constant, C_a and C_b are the amounts of acid and base titrant added (mol/litre). However, this titration method demands that the surface area A of the sample to be precisely known, which is highly unlikely in the case of phyllosilicates [39]. In simplified Mular–Roberts (M–R) method, by adjusting the ionic strength (given by an indifferent electrolyte), the difference between the initial and final pH values ΔpH is plotted against the final pH. The PZC is then referred to the pH point of zero salt effect (ΔpH is zero). In this manner, PZC of many phyllosilicates were determined. Duc, et al. [40] reviewed many literature devoted to probing the acid-base properties of clays by this method. He pointed out that many technical and theoretical difficulties are still encountered, which results in highly scattered potentiometric data. Meanwhile, this method cannot provide a numerical estimate of the magnitude of the surface charge. Also, it should be noted that the accurate determination of true PZC of minerals by potentiometric titration method is very much limited to the systems without specific adsorbing ions in the solution. The potential-determining ions should only be H^+

and OH^- , which induce pH changes. If other ions are also proved to act as pdi in the system, such as Mg^{2+} being potential-determining ions in the case of talc, this method cannot be applied successfully [20].

Moreover, similar to the results from ζ potential measurements, this method can only give a combination of charges from both the basal planes and edge surfaces of phyllosilicates, which can vary with the basal/edge ratio of particles. Clearly, a more thorough understanding of the charging behaviour of specific surface of phyllosilicate minerals to better investigate their corresponding colloidal behaviours is needed.

In addition to above two conventional techniques which can only give the average surface charge characteristics of phyllosilicates, SFG and AFM are used to probe the surface charging behaviour of minerals at molecular level by fitting the SF spectral and interaction forces, respectively. By investigating the spectral change of the interfacial molecular species using SFG or probing interaction forces using AFM on relatively small sampling area, these two methods provide the possibility to examine the individual face of phyllosilicate minerals.

2.3.3 Sum frequency generation spectroscopy

Opposed to the titration method, Sum frequency generation (SFG) is independent of interpreting the electrical potential based on acid-base titration stoichiometry in electrolyte. In SFG method [41-42], two laser beams at frequencies of ω_1 and ω_2 mix at a surface and generate an output beam picked up by a detector with the sum frequency $\omega = \omega_1 + \omega_2$. One of the laser beams is a visible wavelength laser held at a constant frequency and the other is a tunable infrared laser. By tuning the IR beam across a vibrational resonance, the molecules at the interface will interact with the electric field by generating a new field that oscillates at the sum of the

incident frequencies. For example, when protonation/deprotonation reaction dominates at the surface, the water is dominated by different interfacial water species such as the tetrahedrally coordinated and weakly bound water molecules. Their relative intensities of frequency peaks and orientation will be changed as a function of the solution pH. Therefore, by analyzing SFG results of different water species at different pH values, the estimation of the PZC can be obtained.

Yeganeh et al. [41] first employed SFG to probe OH stretch vibrations of a typical water/oxide (alumina) interfaces. This method was chosen as an alternative method to study the charging behaviour and the PZC of metal oxide and related minerals. Hopkins [42] reviewed recently reported work on the solid/aqueous interface using this method, which included the neat non-metal aqueous interfaces, self-assembled monolayers, surfactants, adsorbates and polymers. Stack et al. [43] studied the charging behaviour of water/ sapphire interfaces at different pH values. The edge of sapphire is a sharing AlO_6 octahedral structure which is also seen in many other minerals, especially the mica group. By using this method, the PZC of the sapphire was found to be around pH 6.3, much lower than the well-reported PZC at pH 9.

However, as a nascent technique, due to certain limitations, there is still no common agreement regarding the experimental setup or interpretation of the results [41-43]. Quiet few studies on investigating surface character of phyllosilicates using this method were reported [42].

2.3.4 Atomic force microscopy

Atomic force microscopy (AFM) is a well developed technique and widely used to study the surface properties of phyllosilicates [44-51]. Various phyllosilicate surfaces such as kaolinite [45], illite [46], talc [47-50] and mica [12, 51] have

been studied by AFM using colloid probe technique. In this technique, the interaction forces between an AFM probe and phyllosilicate surfaces are directly measured and then fitted with the DLVO theory. By solving equations that correlate the surface potential with interaction force profiles, the AFM derived Stern potential can be obtained. As the principal technique used in this study, the details about the working principles of AFM will be introduced in Chapter 3.

Although AFM method has been well established to study the surface property of minerals, quiet few studies were reported on using AFM colloid probe technique to investigate the anisotropic character of specific faces of phyllosilicates. The biggest challenge of applying this technique to determine the surface charge characteristics of phyllosilicate minerals is the preparation of sufficiently smooth surfaces. For this reason, most AFM colloid probe studies of phyllosilicate minerals had been performed on cleavage basal planes or simply rough surfaces of phyllosilicate minerals.

By depositing kaolinite basal planes on differently charged substrates, Gupta and Miller [45] investigated the anisotropic character of different kaolinite basal planes (T or O) by measuring surface forces on each basal plane. The different charging behaviour, wetting characteristics and the surface hydrophobicity of two kaolinite basal planes have been observed. The PZC, or more precisely the point of zero Stern potential of silica-like T basal plane of kaolinite was determined to be at $\text{pH} > 4$, while the PZC of alumina-like O basal plane of kaolinite was found between $\text{pH} 6-8$.

Regarding to phyllosilicate edge surfaces, Nalaskowski et al. [50] used a talc particle (around $20 \mu\text{m}$) as an AFM probe to measure the forces between this talc particle and talc basal planes or edge surfaces in aqueous solutions of varying pH

values. Although their study showed different electric properties between basal planes and edge surfaces, their AFM force curves could only be analyzed semi-quantitatively at the best due to the ill-defined geometry of the talc particles glued on AFM cantilevers and high roughness of prepared edge surfaces.

Zhao et al. [12] probed the interaction forces on muscovite basal planes and edge surfaces using a silica sphere of 8 μm diameter, glued on an AFM cantilever. In order to quantitatively analyze the measured force curves, a microtome cutting technique was employed for the first time with the purpose of obtaining a suitably smooth edge surface. Although the surface smoothness of muscovite edge surface was greatly improved by microtome cutting technique, the obtained edge surface was still not sufficiently smooth, especially compared with its basal plane. The roughness over the contact area for silica colloid probe remains too high, as indicated by significantly weaker forces measured. Eventually, the surface topology was reconstructed by obtained AFM image of the surface and SEI was employed by these authors in their analysis to account for the effect of surface roughness.

By fitting the interactions between the silica probe and muscovite surfaces with DLVO theory, the AFM-derived surface potentials of muscovite basal plane were found to be pH-insensitive, while the mica edges were highly pH-dependent with the estimated PZC to be around pH 7.5 ± 0.5 . Although this innovative study demonstrated the possibility of using AFM colloidal probe technique to study anisotropic surface charge properties of phyllosilicate minerals, it was still limited to obtain accurate result by some shortcomings. One problem in their study is that the colloidal interaction forces were measured with a micron size silica probe, while an AFM cantilever with a sharp tip was used to obtain a good AFM image

with detailed morphological characteristics of the surface. This switching of the probe particle to the sharp tip means that the recreated image used in SEI calculation may not be the exact spot where the force profile was measured. To resolve this uncertainty, those authors used several representative images to carry out the SEI calculations and the average potentials of muscovite edge surfaces were determined. However, due to the prepared surface remains too rough, the determined surface potentials of muscovite edge surfaces cannot be considered to be accurate but rather semi quantitative. Therefore, establishing a suitable technique to improve the quality of the prepared edge surface to minimize the uncertainties of SEI calculations is of great importance.

2.4 References

- [1] Masliyah, J. H., Bhattacharjee, S., 2006, "Electrokinetic and Colloid Transport Phenomena," Wiley Interscience, Hoboken, New Jersey.
- [2] Hamaker, H. C., 1937, "The London-Van Der Waals Attraction between Spherical Particles," *Physica*, 4 (10) pp. 1058-1072.
- [3] Bergström, L., 1997, "Hamaker Constants of Inorganic Materials," *Advances in Colloid and Interface Science*, 70(1) pp. 125-169.
- [4] Hunter, R. J., 2001, "Foundations of Colloid Science: Second Ed., Clarendon Press, Oxford.
- [5] Warszyński, P., Adamczyk, Z., 1997, "Calculations of Double Layer Electrostatic Interactions for the Sphere/Plane Geometry," *Journal of Colloid and Interface Science*, 187(2) pp. 283-295.
- [6] Butt, H., Cappella, B., Kappl, M., 2005, "Force Measurements with the Atomic Force Microscope: Technique, Interpretation and Applications," *Surface Science Reports*, 59(1-6) pp. 1-152.
- [7] White, L. R., 1983, "On the Derjaguin Approximation for the Interaction of Macrobodies," *Journal of Colloid and Interface Science*, 95(1) pp. 286-288.
- [8] Suresh, L., Walz, J. Y., 1996, "Effect of Surface Roughness on the Interaction Energy between a Colloidal Sphere and a Flat Plate," *Journal of Colloid and Interface Science*, 183(1) pp. 199-213.
- [9] Bhattacharjee, S., Elimelech, M., 1997, "Surface Element Integration: A Novel Technique for Evaluation of DLVO Interaction between a Particle and a Flat Plate," *Journal of Colloid and Interface Science*, 193(2) pp. 273-285.
- [10] Bhattacharjee, S., Ko, C. H., Elimelech, M., 1998, "DLVO Interaction between Rough Surfaces," *Langmuir*, 14(12) pp. 3365-3375.
- [11] Huang, X., Bhattacharjee, S., Hoek, E. M. V., 2010, "Is Surface Roughness a "Scapegoat" Or a Primary Factor when Defining Particle-Substrate Interactions?" *Langmuir*, 26(4) pp. 2528-2537.
- [12] Zhao, H., Bhattacharjee, S., Chow, R., Wallace, D., Masliyah, J. H., Xu, Z., 2008, "Probing Surface Charge Potentials of Clay Basal Planes and Edges by Direct Force Measurements," *Langmuir*, 24(22) pp. 12899-12910.

- [13] Laskowski, J. S., 2010, "Rheological Properties of Aqueous Suspensions of Anisotropic Minerals," 8th UBC-McGill-UA symposium, M. Pawlik, ed. Vancouver, BC, Canada.
- [14] Ndlovu, B. N., Forbes, E., Becker, M., Deglon, D. A., Franzidis, J. P., Laskowski, J. S., 2011, "The Effects of Chrysotile Mineralogical Properties on the Rheology of Chrysotile Suspensions," *Minerals Engineering*, 24(9) pp. 1004-1009.
- [15] Ndlovu, B., Becker, M., Forbes, E., Deglon, D., Franzidis, J., 2011, "The Influence of Phyllosilicate Mineralogy on the Rheology of Mineral Slurries," *Minerals Engineering*, 24(12) pp. 1314-1322.
- [16] Leong, Y. K., Boger, D. V., Parris, D., 1991, "Surface and Rheological Properties of Zirconia Suspensions," *Chemical Engineering Research and Design*, 69(5) pp. 381-385.
- [17] Johnson, S. B., Franks, G. V., Scales, P. J., Boger, D. V., Healy, T. W., 2000, "Surface chemistry–rheology Relationships in Concentrated Mineral Suspensions," *International Journal of Mineral Processing*, 58(1-4) pp. 267-304.
- [18] Johnson, S. B., Russell, A. S., Scales, P. J., 1998, "Volume Fraction Effects in Shear Rheology and Electroacoustic Studies of Concentrated Alumina and Kaolin Suspensions," *Colloids and Surfaces A-Physicochemical and Engineering Aspects*, 141(1) pp. 119-130.
- [19] Burdukova, E., Becker, M., Bradshaw, D. J., Laskowski, J. S., 2007, "Presence of Negative Charge on the Basal Planes of New York Talc," *Journal of Colloid and Interface Science*, 315(1) pp. 337-342.
- [20] Alvarez-Silva, M., Uribe-Salas, A., Mirnezami, M., Finch, J. A., 2010, "The Point of Zero Charge of Phyllosilicate Minerals using the Mular-Roberts Titration Technique," *Minerals Engineering*, 23(5) pp. 383-389.
- [21] Fuerstenau, D. W., Pradip, 2005, "Zeta Potentials in the Flotation of Oxide and Silicate Minerals," *Advances in Colloid and Interface Science*, 114-115 pp. 9-26.
- [22] Kosmulski, M., 2012, "IEP as a Parameter Characterizing the pH-Dependent Surface Charging of Materials Other than Metal Oxides," *Advances in Colloid and Interface Science*, 171–172 pp. 77-86.

- [23] Nosrati, A., Addai-Mensah, J., and Skinner, W., 2012, "Rheological Behaviour of Muscovite Clay Slurries: Effect of Water Quality and Solution Speciation," *International Journal of Mineral Processing*, 102-103 pp. 89-98.
- [24] Alkan, M., Demirbaş, O., and Doğan, M., 2005, "Electrokinetic Properties of Kaolinite in Mono- and Multivalent Electrolyte Solutions," *Microporous and Mesoporous Materials*, 83(1-3) pp. 51-59.
- [25] Taubaso, C., Afonso, M. D., Sanchez, R. M. T., 2004, "Modelling Soil Surface Charge Density using Mineral Composition," *Geoderma*, 121(1-2) pp. 123-133.
- [26] Tombác, E., and Szekeres, M., 2006, "Surface Charge Heterogeneity of Kaolinite in Aqueous Suspension in Comparison with Montmorillonite," *Applied Clay Science*, 34(1-4) pp. 105-124.
- [27] Fornasiero, D., Ralston, J., 2005, "Cu (II) and Ni (II) Activation in the Flotation of Quartz, Lizardite and Chlorite," *International Journal of Mineral Processing*, 76(1-2) pp. 75-81.
- [28] Tan, H., Skinner, W., and Addai-Mensah, J., 2012, "pH-Mediated Interfacial Chemistry and Particle Interactions in Aqueous Chlorite Dispersions," *Chemical Engineering Research and Design*, 91(3) pp. 448-456.
- [29] Alvarez-Silva, M., Mirnezami, M., Uribe-Salas, A., Finch, J. A., 2010, "Point of Zero Charge, Isoelectric Point and Aggregation of Phyllosilicate Minerals," *Canadian Metallurgical Quarterly*, 49(4) pp. 405-410.
- [30] Tombacz, E., Csanaky, C., Illes, E., 2001, "Polydisperse Fractal Aggregate Formation in Clay Mineral and Iron Oxide Suspensions, pH and Ionic Strength Dependence," *Colloid and Polymer Science*, 279(5) pp. 484-492.
- [31] Luckham, P. F., and Rossi, S., 1999, "The Colloidal and Rheological Properties of Bentonite Suspensions," *Advances in Colloid and Interface Science*, 82(1-3) pp. 43-92.
- [32] Rand, B., Melton, I. E., 1977, "Particle Interactions in Aqueous Kaolinite Suspensions. I. Effect of pH and Electrolyte upon the Mode of Particle Interaction in Homoionic Sodium Kaolinite Suspensions," *Journal of Colloid and Interface Science*, 60(2) pp. 308-320.
- [33] James, A., Williams, D., 1982, "Flocculation and Rheology of Kaolinite Quartz Suspensions," *Rheologica Acta*, 21(2) pp. 176-183.

- [34] Parks, G. A., 1965, "The Isoelectric Points of Solid Oxides, Solid Hydroxides, and Aqueous Hydroxo Complex Systems," *Chemical Reviews*, 65(2) pp. 177-198.
- [35] Kosmulski, M., 2009, "Compilation of PZC and IEP of Sparingly Soluble Metal Oxides and Hydroxides from Literature," *Advances in Colloid and Interface Science*, 152(1-2) pp. 14-25.
- [36] Rasmusson, M., Rowlands, W., O'Brien, R. W., Hunter, R. J., 1997, "The Dynamic Mobility and Dielectric Response of Sodium Bentonite," *Journal of Colloid and Interface Science*, 189(1) pp. 92-100.
- [37] Rowlands, W. N., O'Brien, R. W., 1995, "The Dynamic Mobility and Dielectric Response of Kaolinite Particles," *Journal of Colloid and Interface Science*, 175(1) pp. 190-200.
- [38] Hunter, R. J., 1998, "Recent Developments in the Electroacoustic Characterization of Colloidal Suspensions and Emulsions," *Colloids and Surfaces A: Physicochemical and Engineering Aspects*, 141(1) pp. 37-66.
- [39] Hunter, R. J., 1982, "The Flow Behaviour of Coagulated Colloidal Dispersions," *Advances in Colloid and Interface Science*, 17(1) pp. 197-211.
- [40] Duc, M., Gaboriaud, F., Thomas, F., 2005, "Sensitivity of the Acid-Base Properties of Clays to the Methods of Preparation and Measurement: 2. Evidence from Continuous Potentiometric Titrations," *Journal of Colloid and Interface Science*, 289(1) pp. 148-156.
- [41] Yeganeh, M. S., Dougal, S. M., Pink, H. S., 1999, "Vibrational Spectroscopy of Water at liquid/solid Interfaces: Crossing the Isoelectric Point of a Solid Surface," *Physical Review Letters*, 83(6) pp. 1179-1182.
- [42] Hopkins, A. J., McFearin, C. L., and Richmond, G. L., 2005, "Investigations of the Solid-Aqueous Interface with Vibrational Sum-Frequency Spectroscopy," *Current Opinion in Solid State and Materials Science*, 9(1-2) pp. 19-27.
- [43] Stack, A., Higgins, S., Eggleston, C., 2001, "Point of Zero Charge of a Corundum-Water Interface Probed with Optical Second Harmonic Generation (SHG) and Atomic Force Microscopy (AFM): New Approaches to Oxide Surface Charge," *Geochimica Et Cosmochimica Acta*, 65(18) pp. 3055-3063.

- [44] Ducker, W., Senden, T., Pashley R., 1991, "Direct Measurement of Colloidal Forces using an Atomic Force Microscope," *Nature*, 353(6341) pp. 239-241.
- [45] Gupta, V., Miller, J. D., 2010, "Surface Force Measurements at the Basal Planes of Ordered Kaolinite Particles," *Journal of Colloid and Interface Science*, 344(2) pp. 362-371.
- [46] Long, J., Xu, Z., Mashyah, J. H., 2006, "Role of Illite-Illite Interactions in Oil Sands Processing," *Colloids and Surfaces A-Physicochemical and Engineering Aspects*, 281(1-3) pp. 202-214.
- [47] Wallqvist, V., Claesson, P. M., Swerin, A., 2006, "Interaction Forces between Talc and Hydrophobic Particles Probed by AFM," *Colloids and Surfaces A: Physicochemical and Engineering Aspects*, 277(1-3) pp. 183-190.
- [48] Wallqvist, V., Claesson, P. M., Swerin, A., Schoelkopf, J., Gane, P. A. C., 2007, "Interaction Forces between Talc and Pitch Probed by Atomic Force Microscopy," *Langmuir*, 23(8) pp. 4248-4256.
- [49] Chi, R., Xu, Z., DiFeo, T., Finch, J. A., Yordan, J. L., 2001, "Measurement of Interaction Forces between Talc and Toner Particles," *Journal of Pulp and Paper Science*, 27(5) pp. 152-157.
- [50] Nalaskowski, J., Abdul, B., Du, H., Miller, J. D., 2007, "Anisotropic Character of Talc Surfaces as Revealed by Streaming Potential Measurements, Atomic Force Microscopy, Molecular Dynamics Simulations and Contact Angle Measurements," *Canadian Metallurgical Quarterly*, 46(3) pp. 227-235.
- [51] Hartley, P. G., Larson, I., Scales, P. J., 1997, "Electrokinetic and Direct Force Measurements between Silica and Mica Surfaces in Dilute Electrolyte, Solutions," *Langmuir*, 13(8) pp. 2207-2214.

Chapter 3

Materials, characterization and methods

3.1 Materials

Talc obtained from Luzmenac America (Englewood, CO, USA) and muscovite supplied by S & J Trading (Glen Oaks, NY, USA) were used throughout this study. Silica wafers with one side polished were purchased from Nanofab (University of Alberta, Canada). KCl (Aldrich Inc.) was used as supporting electrolyte. HCl and NaOH (Fisher Inc.) were used as pH modifiers. $\text{CaCl}_2 \cdot 2\text{H}_2\text{O}$ and $\text{MgCl}_2 \cdot 6\text{H}_2\text{O}$ (Aldrich Inc.) were used as sources of Ca^{2+} and Mg^{2+} , respectively. All the reagents used were of ACS analytical grade. High purity Milli-Q water with a resistivity of $18.2 \text{ M}\Omega \text{ cm}^{-1}$, prepared with an Elix 5 followed by a Millipore-UV Plus Ultra water purification system (Millipore Inc.), was used for preparation of solutions used throughout this study.

3.2 Preparation of different phyllosilicate surfaces

Since both talc and muscovite have perfect cleavages along their basal planes, the basal planes of these two phyllosilicates are freshly cleaved using a sticky tape in a dust-free, horizontal laminar flow hood (NuAire, Inc., Plymouth, MN, USA).

3.2.1 Ultramicrotome cutting technique

In the case of edge surfaces, an ultramicrotome cutting procedure was developed to obtain suitable smooth edge surfaces for further study at molecular level using AFM. As shown in Figure 3.1, a very small and thin piece of phyllosilicate mineral was first embedded in an epoxy resin (Electron Microscopy Sciences,

Hatfield, PA, USA) and baked as following the instructions to cure the sample as a block.

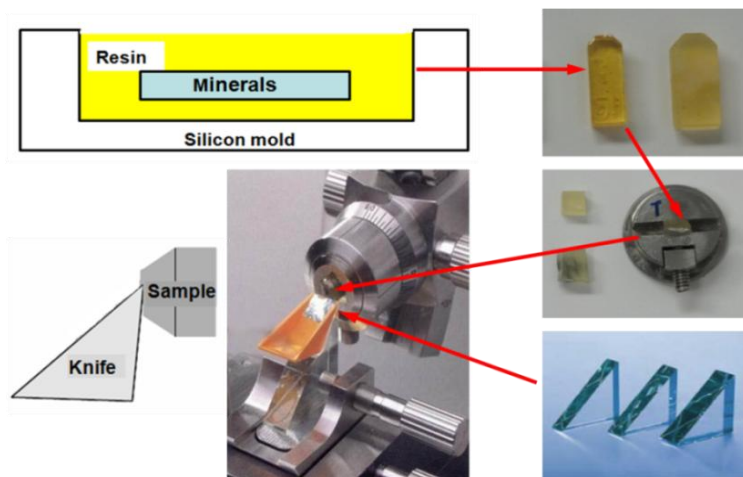


Figure 3.1 Schematics of preparing the phyllosilicate edge surfaces by the ultramicrotome cutting technique.

To optimize cutting result, the resin should have similar hardness as the mineral sample to decrease folding of the resin or sample and to avoid the sample being pulled out during the cutting. To ensure the cutting surface having less slanting angles, the epoxy block was trimmed by a razor blade under an optical microscope to make phyllosilicate sheets as perpendicular as possible to the cutting edge of the knife on the ultramicrotome. After trimming, the block was glued on the metallic disk with epoxy (Master Bond, Hackensack, NJ, USA) and mounted on the ultramicrotome (EM UC 7, Leica Microsystems Inc.) for cutting. Surfaces were cut by following the procedures for thin sectioning. Instead of collecting thin sections that were cut off, as in most applications for TEM sample preparation, the remaining blocks with the finish surface were used for further AFM imaging, colloidal force measurements and other related surface analysis. Before being used in AFM study, the prepared phyllosilicate surface was subjected to a high-pressure ultrapure nitrogen gas blow to remove any possible

flakes and dust on the surface, and rinsed with Milli-Q water and ethanol. Finally, the prepared surface was cleaned by UV-ozone immediately prior to its use to remove any organic contaminants.

3.2.2 Characterization of prepared surfaces

3.2.2.1 Field emission secondary electron microscopy imaging

The morphology of the obtained edge surface prepared by ultramicrotome cutting technique was examined by Field emission secondary electron microscopy (FE-SEM) equipped with a scanning Auger microprobe (JAMP-9500F, Oxford Instruments). To prevent a poor quality image caused by surface charging, low voltage was applied during the imaging to minimize the charge effects. Typical FE-SEM images of edge surfaces prepared by ultramicrotome cutting technique are shown in Figure 3.2. Figure 3.2 (a) shows a large scale image of the prepared edge surface at lower magnification and Figure 3.2 (b) shows a high resolution image after zooming in to a small smooth area. The resin appeared to be darker than the edge surface due to its low electron scattering yield. Some pitch lines and tiny debris were observed on the edge surfaces. These pitch lines are possibly due to pull off and carryover of tiny phyllosilicate debris which stick on the cutting knife by electrostatic adhesion and are hard to be removed during the cutting process.

3.2.2.2 X-ray photoelectron spectroscopic analysis

The surface elemental composition of both basal planes and edge surfaces of each mineral was obtained by performing X-ray photoelectron spectroscopic (XPS) analysis with an Axis 165 spectrometer (Kratos Analytical). As shown in Figure 3.3, the presence of different cations is seen in the spectra of different phyllosilicate minerals studied. The dominated cationic elements of both basal

planes and edge surfaces of talc are silicon and magnesium. For muscovite basal planes and edge surfaces, silicon, aluminum and potassium were detected as major making up cations, indicating isomorphous substitution of Si^{4+} by Al^{3+} with K^+ as compensating ions. Trace amounts of fluoride and iron were also found on the talc and muscovite basal planes, respectively.

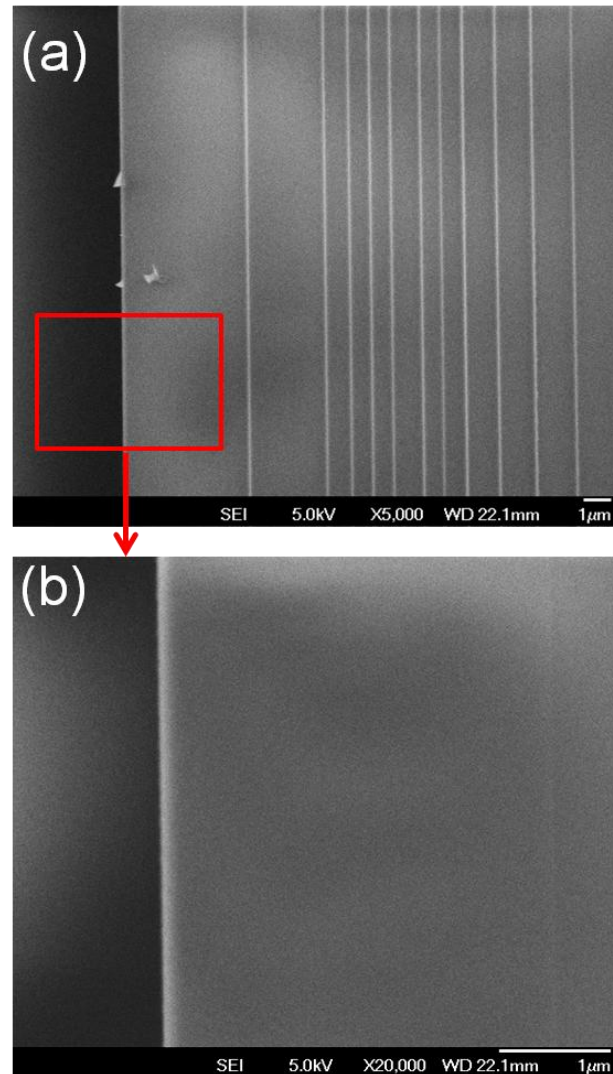


Figure 3.2 Typical FE-SEM images of the talc edge surface prepared by the ultramicrotome cutting technique: (a) taken with lower area resolution but larger scanning area; and (b) taken by zooming in on a small smooth area at a high resolution.

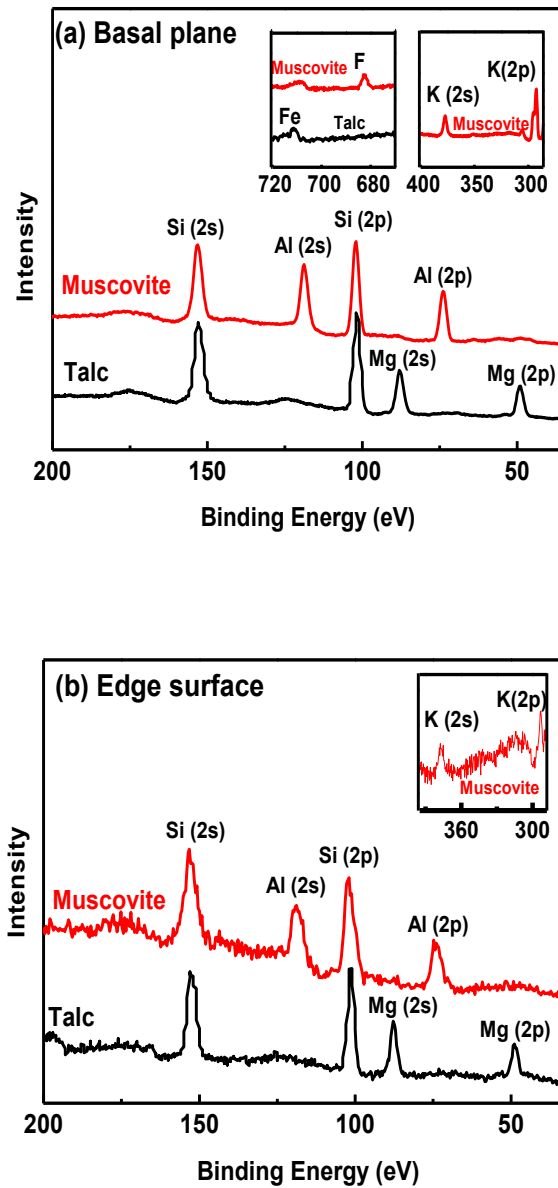


Figure 3.3 XPS spectra of talc and muscovite (a) basal plane and (b) edge surface.

3.3 AFM

3.3.1 The principle of the AFM

As introduced in Chapter 2, AFM is a powerful tool for directly probing the surface topographies and intermolecular forces at nanoscale resolution, which has

been broadly used in materials, biology, mineral processing and nanofabrication. As depicted in Figure 3.4, a basic AFM system consists of a piezoelectric transducer, a cantilever with tip, a laser beam system and a photodiode. When a sample is brought toward and away from the AFM tip on cantilever, the interaction forces between the sample and the tip cause the cantilever to deflect. This reflected laser beam is directed by a mirror to a split photodiode, which can detect the deflection of the cantilever to a fraction of a nanometer resolution.

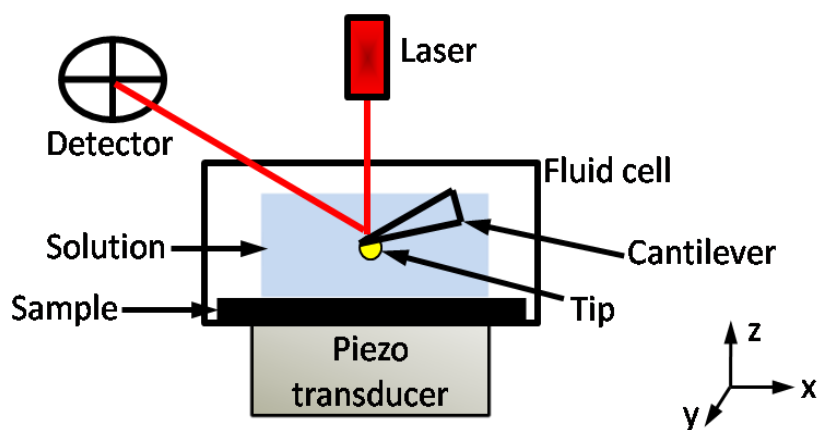


Figure 3.4 Schematics of the components in an AFM set-up.

3.3.2 *AFM imaging*

Compared to other conventional microscopic techniques in imaging such as TEM or SEM, AFM has a distinct advantage that it can be used in situ without the requirement of the vacuum environment. By using a cantilever with a sharp tip, the atomic resolution can be obtained in imaging process. Usually, the imaging process is performed in two modes: contact mode or tapping mode. In the contact mode, the cantilever is kept at constant loading force and dragged line by line over the surface to create profiles and construct an image. In the tapping mode, the cantilever is kept at its resonance frequency and gently tapped on the surface which is moving in the z direction to reach contact. When the tip is lifted away

from the contact, the surface is moved in the x-y directions, avoiding the drag of the tip on the surface.

3.3.3 *AFM force measurement*

In addition to mapping the surface topography, AFM can also probe the interaction forces between a flat surface and an AFM tip. For one AFM force measurement cycle, both the long range attractive or repulsive forces between two surfaces when they are approaching each other and the adhesion (pull off) force when one surface is retracted from the other can be recorded.

A typical “force vs piezo displacement” curve recorded by AFM is shown in Figure 3.5 (a). When the sample on the piezo transducer stage start to move toward the tip on the cantilever, at the beginning, there is no deflection of the cantilever due to zero interaction force between the two surfaces at large separation distances. Therefore, a constant output signals is obtained initially in this zero deflection region (Figure 3.5 (a): a0-a1). As the sample moves closer to the tip, the change of the output signal is observed (Figure 3.5 (a): a1-a2). An increase in the output signal indicates the cantilever being pushed away by the repulsion between the two surfaces while a decrease in the output signal indicates the cantilever moving towards the lower sample surface corresponding to an attraction between the two surfaces. Eventually, the sample will be brought by the translation stage into the contact with the tip and then a constant compliance is observed. In this constant compliance region, though the surface is in contact with the probe, the surface is still moving with the probe. The cantilever displacement (deflection) can be calibrated in terms of output signals from the known displacement of the piezo to which the surface is attached. The slope of this linear part of the curve (Figure 3.5 (a): a2-a3) is estimated as the compliance gradient

(deflection sensitivity) in V/nm, which later can be used to convert the measurement cantilever deflection from deflection voltage to nanometer. At the end of the extension of the piezo transducer, the piezo starts to retract (Figure 3.5 (a): a3-a4). The cantilever continues to follow the displacement of the piezo due to the adhesion force holding the tip to the sample.

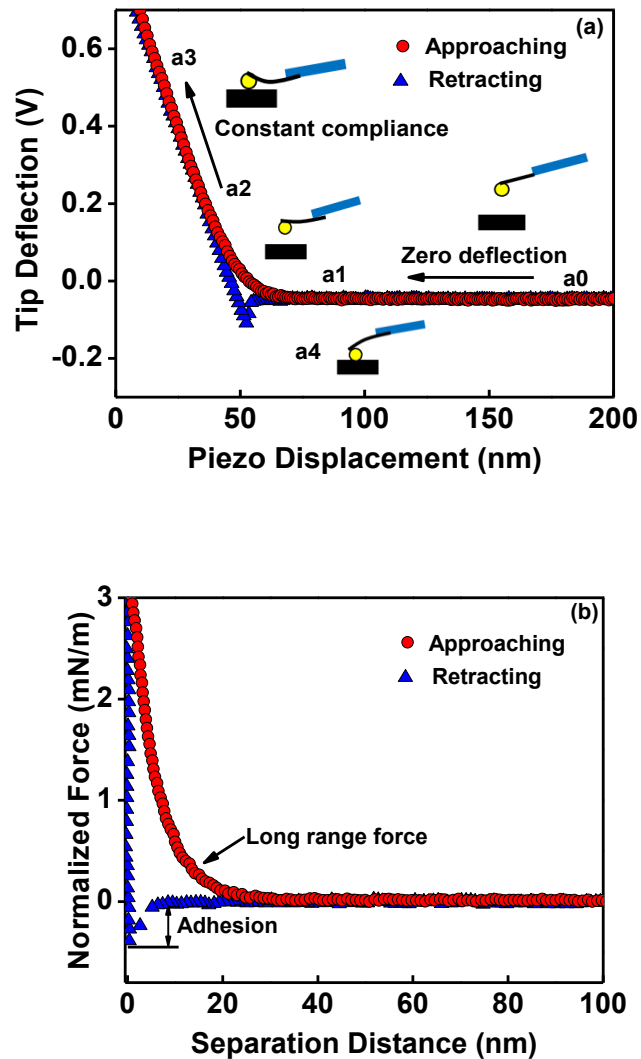


Figure 3.5 Typical AFM force curves: (a) “force vs. piezo displacement” curves recorded by AFM and (b) “force vs. separation distance” force profiles converted from (a).

The force acting between the tip and the sample is determined from the deflection of the cantilever and its spring constant using Hooke's law ($F = kx$), where x represents the deflection and k is the spring constant of the cantilever. Finally, in this manner, the "force vs. piezo displacement" is converted to the "force vs. separation distance" force profile as shown in Figure 3.5 (b). More detailed description on the principles of the AFM can be found in literature [1-2].

In this dissertation, AFM technique was employed to probe the colloidal interaction as well as to image surface topographies. A Multimode AFM with Nanoscope IIIa controller, equipped with PicoForce or E scanner and vendor-provided liquid cell, all supplied by Veeco Instruments Inc., (Santa Barbara, CA, USA) was used throughout this study.

In experiments reported in Chapters 4-6, AFM measurements were carried out in 1 mM KCl solutions as the supporting electrolyte. After filling the liquid cell with the test aqueous solutions, the system was allowed to stabilize for at least 30 minutes before each measurement. At least three pairs of tip-surface were used for each surface type and the measurements were conducted at various locations on one surface for each condition of the solution. For force measurement, at each location, continuous approaching and retracting force curves were taken and the data was only recorded when the force curve was stable. All experiments were conducted at room temperature ($20 \pm 2^\circ\text{C}$). The raw force profiles were analyzed with SPIP software (Image Metrology) which converts the deflection-distance data to force-separation curves, including baseline and hysteresis correction. The spring constant of each cantilever was measured by the thermal tune method using the built-in option in the Veeco AFM software version 8.10, with values obtained

varying from 0.12 to 0.19 N/m. The maximum loading force used in the force measurement was controlled within the same range.

3.3.4 AFM tip evaluation

In Chapters 4-6, silicon nitride tips (NP, Veeco Inc., Santa Barbara, CA, USA) were used in AFM experiments. It has been reported that compared to micron sized probe particles, the use of sharp AFM tips allows mapping of surface charge or Stern potential at a spatial resolution of 20-100 nm which is about 20-100 fold higher than the colloidal probe technique [3]. One possible disadvantage of using the sharp tip is its lower sensitivity for force measurements due to weaker interaction forces from small interacting surfaces. However, the high surface charge reported for this type of tip as a probe offsets some negative effects of weak interaction forces [4]. In order to obtain its geometry and apex curvature, the morphology of the tip was examined with a field emission scanning Auger microprobe (JAMP-9500F, Jeol, Japan). A pyramid-like shape tip is shown in Figure 3.6 (a and b). As shown by the scanning Auger electron spectrum in Figure 3.6 (b1), the tip consists of 49.4% silicon and 42.5% nitrogen with a small amount of oxygen (8.1%) on the top end of the tip which interacts with the phyllosilicate surface during the AFM force measurements.

The tip geometry was also evaluated with the Nanoscope software (Veeco Inc., Santa Barbara, CA, USA) by analyzing the image of a polycrystalline titanium “tip-check” sample (RS, Veeco Inc., Santa Barbara, CA, USA) taken by the tip. This “tip-check” sample contains extremely sharp features. The effective tip diameter and aspect ratio at a selected distance from the tip apex were calculated from the width and height of the image taken. A detailed description of the tip geometry evaluation can be found elsewhere [5]. By using this software program,

the tip geometry can be evaluated by comparing the estimated tip diameter and aspect ratio with selected threshold and limit values. These baseline data were collected by scanning several brand new tips. In order to avoid faulty interrelating data and get consistent results, the tip evaluation was performed after force measurement. If the tip was shown to be worn or bad (i.e. tip was damaged during force measurements), the result would not be used for further analysis.

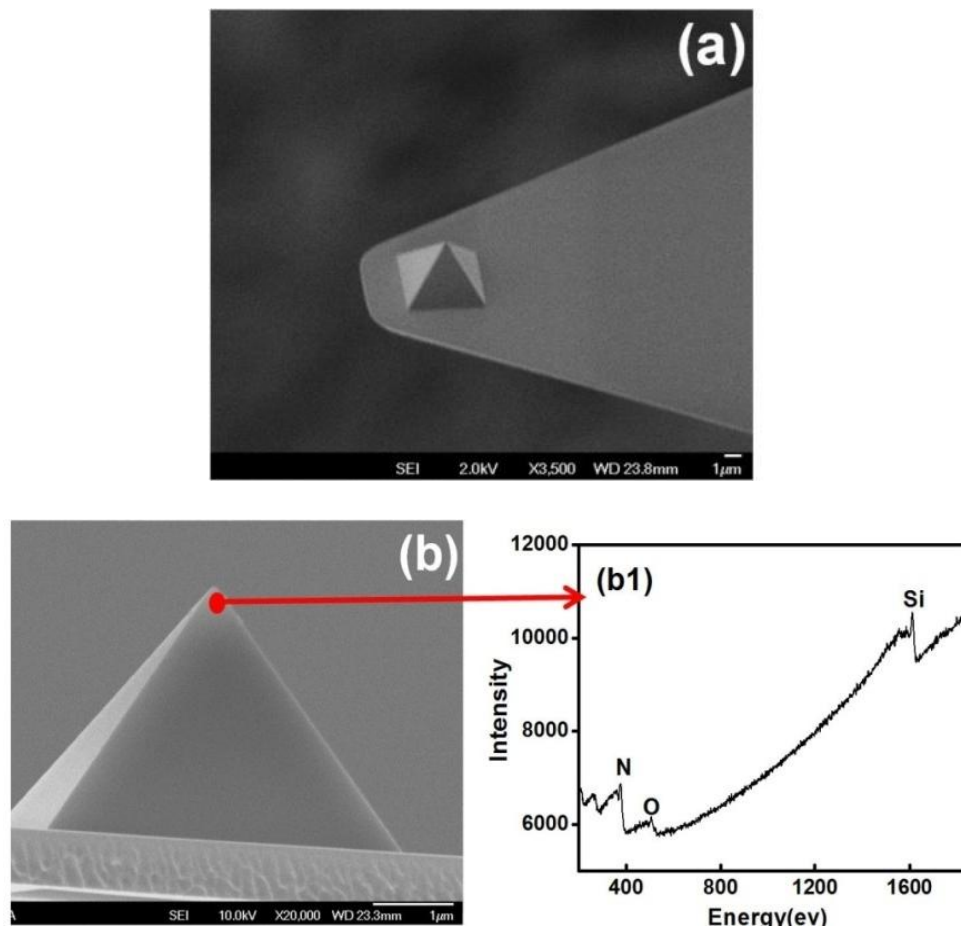


Figure 3.6 Typical FE-SEM images of an AFM silicon nitride tip used in this study: (a) plane view; (b) oblique view and (b1) scanning auger electron spectroscopy analysis on the top end of the tip.

3.4 Theoretical model for DLVO calculation

The van der Waals interaction energy per unit area between two planar surfaces and the corresponding Hamaker constant A_H were calculated using equations (2.2) and (2.3) in Chapter 2. The data of each material used for the calculation of Hamaker constant A_H in equation (2.3) are listed in Table 3.1, taken from literature [6-7] and the ν_e assumed to be the same for all materials.

Table 3.1 The values used for calculation of Hamaker constant A_H taken from literature [6-7].

Materials	Talc	Muscovite	Silica	Silicon nitride	Water
Dielectric constant (ε_i)	3	5.4	3.82	7.4	78.5
Refractive index (n_i)	1.57	1.584	1.448	1.988	1.333

The surface potential ψ and the surface charge density σ are linked to each other by Grahame equation [8]:

$$\sigma = \sqrt{8c_0 \varepsilon_0 k_B T} \sinh\left(\frac{e\psi}{2k_B T}\right) \quad (3.3)$$

The EDL energy per unit area between two planar surfaces a (with surface potential ψ_a and surface charge density σ_a) and b (with surface potential ψ_b and surface charge density σ_b) at distance D was calculated by following equations at different BC.

The EDL interaction energy at constant electrical surface charge BC per unit area

($U_{EDL}^{\sigma-\sigma}$) [9]:

$$U_{EDL}^{\sigma-\sigma} = \frac{1}{2\epsilon_0\kappa} \left\{ (\sigma_a^2 + \sigma_b^2) [\coth(\kappa D) - 1] + 2\sigma_a\sigma_b \operatorname{cosech}(\kappa D) - 1 \right\} \quad (3.4)$$

The EDL interaction energy at constant electrical surface potential BC per unit

area ($U_{EDL}^{\psi-\psi}$) [10]:

$$U_{EDL}^{\psi-\psi} = \frac{\epsilon_0\kappa}{2} \left\{ (\psi_a^2 + \psi_b^2) [1 - \coth(\kappa D)] + 2\psi_a\psi_b \operatorname{cosech}(\kappa D) - 1 \right\} \quad (3.5)$$

The EDL interaction energy at mix BC per unit area ($U_{EDL}^{\sigma-\psi}$) [11]:

$$U_{EDL}^{\sigma-\psi} = \frac{1}{2} \left\{ 2\psi_a\sigma_b \operatorname{sech}(\kappa D) + (\sigma_b^2 / \epsilon_0\kappa - \epsilon_0\kappa\psi_a^2) \times [\tanh(\kappa D) - 1] \right\} \quad (3.6)$$

As mentioned in Chapter 2, the interaction energy between two surfaces of a given geometry can be derived from the interaction energy between two planar plates by DA. Based on the pyramidal shape as shown in Figure 3.6 (a and b), the tip geometry can be reasonably approximated as conical with a spherical cap at its apex as depicted in Figure 3.7. Greek symbols α and β are the geometrical angles for the spherical cap at the tip apex and the conical tip, with $\alpha + \beta = 90^\circ$. D is the distance between the end of the tip and the substrate; L is the distance between a differential surface section of the tip and the substrate; r is the radius of the circle of the tip at a given vertical position and R is the radius of the spherical cap at the end of the tip.

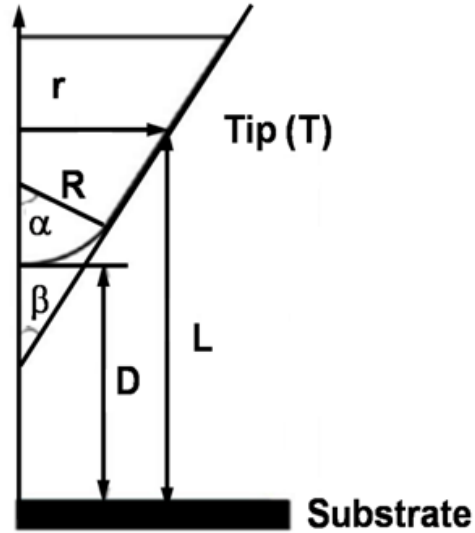


Figure 3.7 Geometry of a model conical AFM tip with spherical apex used for DLVO calculations taken from literature [12].

Therefore, the geometry of the conical tip was break down to two parts: spherical region (S) and conical region (C). The derivations of the DLVO interaction energy U and force F for these two parts were integrated by following the similar procedure in literature [12] as follow:

$$F = \int_0^{\infty} U 2\pi r dr \quad (3.7)$$

In the spherical region (S) of the tip end $0 < r < R \sin \alpha$

$$L = R - \sqrt{R^2 - r^2} + D \quad r dr = (R + D - L) dL$$

In the conical region (C) of the tip end $r > R \sin \alpha$

$$L = D + R(1 - \cos \alpha) + (r - R \sin \alpha) \tan \alpha$$

$$r dr = \left(\frac{L - D - R(1 - \cos \alpha)}{\tan \alpha} + R \sin \alpha \right) \frac{1}{\tan \alpha} dL$$

Therefore: $F = F^S + F^C = 2\pi \left(\int_D^{L_1} U(R+D-L)dL + \frac{1}{\tan^2 \alpha} \int_{L_1}^{\infty} U(L+R \sin \alpha \tan \alpha - L_1)dL \right)$ (3.8)

$$L_1 = D + R(1 - \cos \alpha)$$

For VDW interaction forces:

$$F^{vdw} = -\frac{A}{6} \left[\frac{R+D}{L_1^2} + \frac{R-D}{D^2} \right] \quad (3.9)$$

EDL force at constant electrical surface potential BC:

$$F^{\psi-\psi} = 4\pi\epsilon\epsilon_0\psi_a\psi_b(\alpha_0 e^{-\kappa D} - \alpha_1 e^{-\kappa L_1}) + 2\pi\epsilon\epsilon_0(\psi_a^2 + \psi_b^2)(\alpha_2 e^{-2\kappa D} - \alpha_3 e^{-2\kappa L_2}) + \frac{4\pi\epsilon\epsilon_0\kappa}{\tan \alpha} \left[b_1\psi_a\psi_b e^{-\kappa L_1} - b_2 \frac{(\psi_a^2 + \psi_b^2)}{2} e^{-2\kappa L_1} \right] \quad (3.10)$$

$$\alpha_0 = \kappa R - 1, \alpha_1 = \kappa R \cos(\alpha - 1), \alpha_2 = \alpha_0 + 0.5, \alpha_3 = \alpha_1 + 0.5$$

$$b_1 = R \sin \alpha + \frac{1}{\kappa \tan \alpha} \quad b_2 = R \sin \alpha + \frac{1}{2\kappa \tan \alpha}$$

EDL force at constant surface charge density BC:

$$F^{\sigma-\sigma} = \frac{4\pi}{\epsilon\epsilon_0\kappa^2} \sigma_a\sigma_b(\alpha_0 e^{-\kappa D} - \alpha_1 e^{-\kappa L_1}) + \frac{2\pi}{\epsilon\epsilon_0\kappa^2} (\sigma_a^2 + \sigma_b^2)(\alpha_2 e^{-2\kappa D} - \alpha_3 e^{-2\kappa L_2}) + \frac{4\pi}{\epsilon\epsilon_0\kappa \tan \alpha} \left[b_1\sigma_a\sigma_b e^{-\kappa L_1} + b_2 \frac{(\sigma_a^2 + \sigma_b^2)}{2} e^{-2\kappa L_1} \right] \quad (3.11)$$

EDL force at mix BC:

$$F^S = \pi(R+D) \left[2\psi_a\sigma_b \int_D^{L_1} \sec h(\kappa L)dL + \left(\frac{\sigma_b^2}{\epsilon\epsilon_0\kappa} - \epsilon\epsilon_0\kappa\psi_a^2 \right) \int_D^{L_1} (\tanh(\kappa L) - 1)dL \right] - \pi \left[2\psi_a\sigma_b \int_D^{L_1} \sec h(\kappa L)dL + \left(\frac{\sigma_b^2}{\epsilon\epsilon_0\kappa} - \epsilon\epsilon_0\kappa\psi_a^2 \right) \int_D^{L_1} (\tanh(\kappa L) - 1)LdL \right] \quad (3.12)$$

$$F^C = \frac{\pi b_3}{\tan^2 \alpha} \left(2\psi_a \sigma_b \int_{L_1}^{\infty} \sec h(\kappa L) dL + \left(\frac{\sigma_b^2}{\varepsilon \varepsilon_0 \kappa} - \varepsilon \varepsilon_0 \kappa \psi_a^2 \right) \int_{L_1}^{\infty} (\tanh(\kappa L) - 1) dL \right) + \quad (3.13)$$

$$\frac{\pi}{\tan^2 \alpha} \left[2\psi_a \sigma_b \int_{L_1}^{\infty} \sec h(\kappa L) L dL + \left(\frac{\sigma_b^2}{\varepsilon \varepsilon_0 \kappa} - \varepsilon \varepsilon_0 \kappa \psi_a^2 \right) \int_{L_1}^{\infty} (\tanh(\kappa L) - 1) L dL \right]$$

$$b_3 = R \sin \alpha \tan \alpha - L_1$$

It should be noted that by fitting the measured interaction force profiles between AFM tip and different surfaces with this evaluation model, to be more precisely, the Stern potential instead of the surface potential of specific surface can be obtained, though they are almost the same in magnitude.

3.5 References

- [1] Butt, H., Cappella, B., Kappl, M., 2005, "Force Measurements with the Atomic Force Microscope: Technique, Interpretation and Applications," *Surface Science Reports*, 59(1-6) pp. 1-152.
- [2] Cappella, B., Dietler, G., 1999, "Force-Distance Curves by Atomic Force Microscopy," *Surface Science Reports*, 34(1-3) pp. 1-104.
- [3] Gupta, V., Miller, J. D., 2010, "Surface Force Measurements at the Basal Planes of Ordered Kaolinite Particles," *Journal of Colloid and Interface Science*, 344(2) pp. 362-371.
- [4] Yin, X., Drelich, J., 2008, "Surface Charge Microscopy: Novel Technique for Mapping Charge-Mosaic Surfaces in Electrolyte Solutions," *Langmuir*, 24(15) pp. 8013-8020.
- [5] Veeco Metrology Group, 2002, "Support Note 250, Revision C," Digital Instruments, Santa Barbara, CA.
- [6] Bergström, L., 1997, "Hamaker Constants of Inorganic Materials," *Advances in Colloid and Interface Science*, 70pp. 125-169.
- [7] Wallqvist, V., Claesson, P. M., Swerin, A., Schoelkopf, J., Gane, P. A. C., 2007, "Interaction Forces between Talc and Pitch Probed by Atomic Force Microscopy," *Langmuir*, 23(8) pp. 4248-4256.
- [8] Butt, H., Graf, K., Kappl, M., 2006, "Physics and Chemistry of Interfaces," John Wiley & Sons, KGaA, Weinheim.
- [9] Usui, S., 1973, "Interaction of Electrical Double Layers at Constant Surface Charge," *Journal of Colloid and Interface Science*, 44(1) pp. 107-113.
- [10] Hogg, R., Healy, T. W., Fuerstenau, D. W., 1966, "Mutual Coagulation of Colloidal Dispersions," *Transactions of the Faraday Society*, 62pp. 1638-1651.
- [11] Kar, G., Chander, S., Mika, T. S., 1973, "The Potential Energy of Interaction between Dissimilar Electrical Double Layers," *Journal of Colloid and Interface Science*, 44(2) pp. 347-355.
- [12] Drelich, J., Long, J., Yeung, A., 2007, "Determining Surface Potential of the Bitumen-Water Interface at Nanoscale Resolution using Atomic Force Microscopy," *Canadian Journal of Chemical Engineering*, 85(5) pp. 625-634.

Chapter 4

Determination of anisotropic surface charging characteristics of different phyllosilicates by direct force measurements: Effect of pH*

The work presented in this chapter comprise a detailed study of the effect of pH on the anisotropic surface charge characteristic of two 2:1 layer (TOT) natural minerals, talc and muscovite, as representatives of magnesium and aluminum phyllosilicate minerals, respectively.

In this study, following the methodology described in Chapter 3 to prepare smooth edge surface by the ultramicrotome cutting technique, probe the interaction forces between the AFM tip and phyllosilicate basal/edge surfaces using AFM and fit the measured force profiles with the classical DLVO theory, the electrical surface potentials, or more precisely Stern potential of different talc and muscovite surfaces in aqueous solutions of various pH values were determined. The Stern potential of muscovite basal planes was found to be significantly more negative than the basal plane of talc, both being pH insensitive. In contrast, the Stern potential of edge surfaces was highly pH-dependent, exhibiting a PZC of pH 7.5 and 8.1 for edges of muscovite and talc, respectively.

4.1 Introduction

To fundamentally understand the electrokinetic behaviour of phyllosilicate minerals, it is necessary to study the anisotropic surface charge properties of phyllosilicate surfaces.

*Published work: Yan, L., Englert, A. H., Masliyah, J. H., Xu, Z., 2011, Langmuir, 27(21).

The stability of fine-grained phyllosilicate suspensions is determined largely by the colloidal interactions between phyllosilicate particles. In order to accurately predict phyllosilicates behaviour in industrial applications, an extensive knowledge on anisotropic surface properties of phyllosilicates is essential.

As introduced in Chapter 2, AFM has been widely used to study surface properties of phyllosilicate minerals. Various probe and flat phyllosilicate surface systems such as illite-illite [1], talc-talc [2], silica-mica [3-4], pitch-talc [5] and toner-talc [6] have been studied. AFM force measurements provide the possibility to determine the Stern potential of minerals by fitting the force profiles obtained in aqueous solutions with the DLVO theory. Normally the radius of the colloid probe is around several micrometers, which is too large to allow for accurate imaging of the surface where the force profiles are measured. On the other hand, only very smooth surfaces of the root-mean-square (Rq) roughness less than 1 nm can be studied using the AFM probe techniques [7]. To our knowledge, there are quiet few investigations reported on using AFM colloid probe technique to study the anisotropic character of phyllosilicates on specific basal planes and edge surfaces [2, 4]. In the present study, the effect of pH on the anisotropic surface charge properties of different phyllosilicate surfaces by direct interaction force measurements are investigated, aiming to understand how these anisotropic surface charge properties influence phyllosilicate behaviour in aqueous solutions. In this study, an AFM tip instead of micron size particles is used as probe to explore the mapping of heterogeneous surface charges on edge surfaces. Commercial AFM tips have been widely used for probing the interactions on various surfaces such as multiphase rock [8], kaolinite particles [9], silica plate [10], bitumen [11] or nano particles [12]. The theoretical model for obtaining Stern potential, from the measured force profiles is well developed and verified.

4.2 Results and discussion

4.2.1 Interactions between AFM tip and silica surfaces

To obtain the unknown charge property of a phyllosilicate surface by the method of fitting AFM force profiles, it is necessary to first know the Stern potential of the tip at each testing condition. Since the Stern potential values of silica have been well studied and are quite characteristic for a given solution pH, silica can be used to calibrate/determine the Stern potential of the tip by measuring colloidal forces between the tip and a clean silica wafer in 1 mM KCl solutions of varying pH. A representative AFM image of a silica wafer used for colloidal force measurements is shown in Figure 4.1 (a). The surface roughness (R_q) of the silica wafer cleaned by UV-ozone was 0.166 nm over a $4 \mu\text{m}^2$ area.

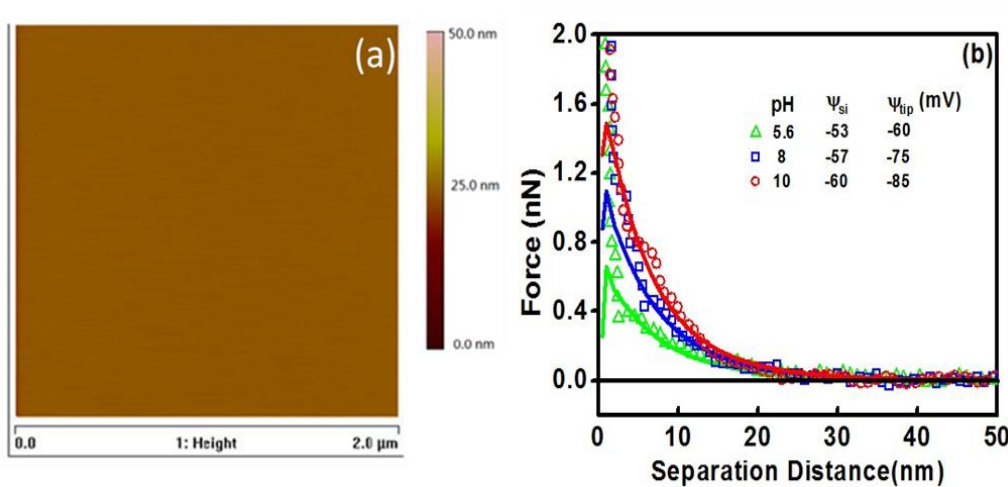


Figure 4.1 Typical (a) AFM image of the silica wafer and (b) interaction forces measured between a silicon nitride tip and the silica wafer in 1 mM KCl solutions at pH 5.6, 7.9 and 9.9. Symbols correspond to experimental data. The solid lines represent the theoretical fit. ψ_{si} and ψ_{tip} are the fitted Stern potential values of the silica surface and the tip, respectively.

Typical force curves of the tip interacting with silica are shown in Figure 4.1 (b). For all pH values tested (5.6, 7.9 and 9.9), the interaction forces are monotonically repulsive on approach. As it is well established that the PZC value of silica is around 2 [13-14], the silica wafer can be treated as being negatively charged over the pH range of 5.6-10 being investigated in this study. Since the force profiles are always repulsive, the surface charge of the tip should also be negative in this pH range. The measured force profiles were analyzed by the classical DLVO theory to quantitatively evaluate the Stern potential of the tip. A MATLAB (The Math Works Inc.) program based on its built-in curve fitting function was developed for the fitting process. As shown in Figure 4.1 (b), the experimentally measured force profiles between the tip and silica in simple electrolyte solutions are found to be fitted quite well with the theoretical force curves, particularly for separation distances larger than 4-5 nm. The discrepancy at very short separation distances is probably due to the presence of repulsive non-DLVO hydration forces between the silica surface and the tip, which were not taken into account in the theoretical model used in the fitting of force profiles in this study. The fitted values of silica Stern potential are compared with the results taken from the literature in Table 4.1 [3-4, 15]. The fitted potential values agree well with the measured values by other methods (Table 4.1), which corroborates the viability of applying this tip-substrate system to study the proposed phyllosilicate surfaces.

Figure 4.2 shows Stern potential values of the tip obtained from AFM force measurements, which are compared to ζ potential values determined on silicon nitride nano powders (Aldrich Inc.) by Zetasizer (Nano ZS, Malvern Instruments, UK). The ζ potential measurement was carried out in 1 mM KCl solutions of different pH values for at least 10 times and the average value was reported. The

Stern potential values of the silicon nitride tip derived from AFM force profiles show a similar trend as the ζ potential values with changing solution pH: becoming more negative with increasing pH over the pH range studied. However, the magnitudes of the ζ potential values are lower than the corresponding Stern potential values obtained by fitting of AFM force profiles, as anticipated by the EDL compression for a system containing simple electrolytes. More importantly, the discrepancy between the two data sets in Figure 4.2 could very likely be a result of differences in surface states of silicon nitride powder and AFM tip. The IEP of silicon nitride reported in the literature varies from 4-6, depending on the surface treatment and measurement methods [8, 16].

Table 4.1 Comparison of best-fitted Stern potential values of silica obtained in this study with corresponding literature values obtained by microelectrophoresis (MEP), streaming potential (SP) and fitting of AFM force profiles.

pH	Silica electrical potential (mV)			
	This work	From literature		
		Value	Method	Ref
5.6	-53 ± 5	~ -51	AFM	[4]
		-50	SP	
		-60	MEP	[2]
		-25 to -60	AFM	
		-50	MEP	[15]
7.9	-57 ± 5	-56	SP	[4]
		-60	SP/ AFM	[2]
		~ -60	MEP	[15]
9.9	-60 ± 5	~ -65	AFM	[4]
		-65	MEP	[15]

In this study, the IEP of silicon nitride tip is determined to be pH 3-4. It appears that the silicon nitride tip used in our study may be partially oxidized, forming silica layer which lowers the IEP of the silicon nitride surface. As presented Figure 3.6 (b1), a small amount (8.1%) of oxygen was detected, confirming the oxidation of the tip. Compared with the tip, the silicon nitride nano powder may be less oxidized, contributing to less negatively charged surfaces as revealed by the ζ potential measurements. Nevertheless, the Stern potential values obtained for silicon nitride from fitting of AFM force profiles agree well with literature values for this kind of tips [8].

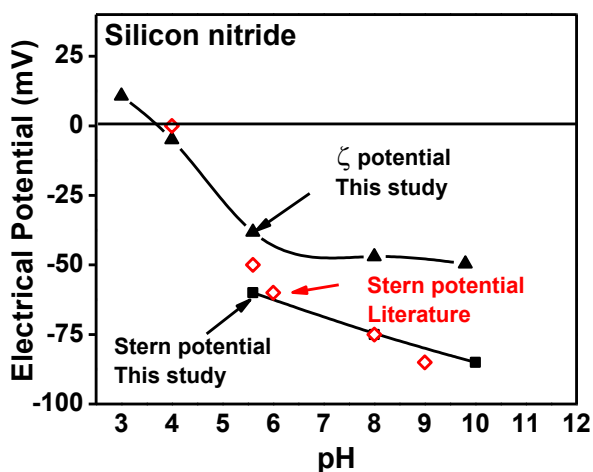


Figure 4.2 Comparison of Stern potential values of silicon nitride tip, determined by fitting of AFM force profiles, with ζ potential values of silicon nitride nano particles determined by electrophoresis method and Stern potentials of this kind of tips reported in literature in 1 mM KCl solutions of different pH values[8].

4.2.2 Interactions between AFM tip and talc surfaces

Representative AFM images of talc basal planes and edge surfaces used for force measurements are shown in Figure 4.3. The same color scheme and scanning size

for the surface images are used for better comparison. Clearly, the edge surfaces of talc prepared with ultramicrotome cutting techniques is sufficiently smooth for nanoscale studies of its surface chemistry.

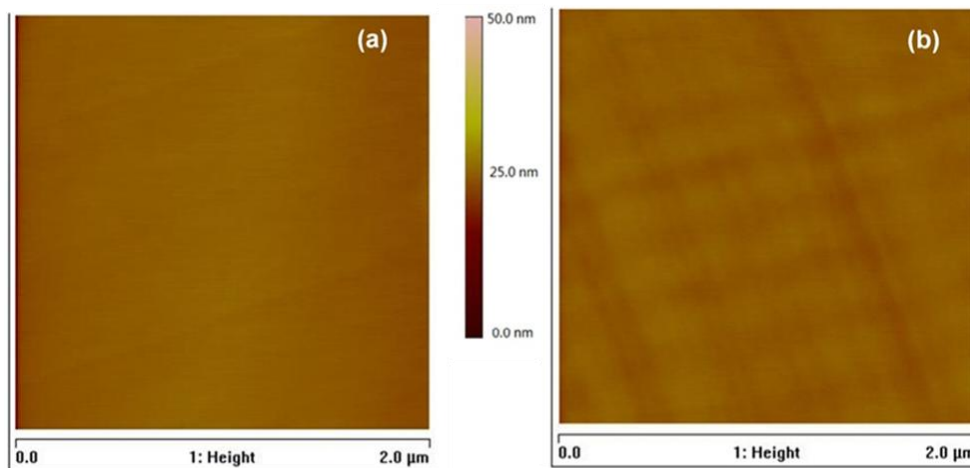


Figure 4.3 Typical AFM images of a prepared hydrophobic talc basal plane and an edge surface: (a) talc basal plane with a mean roughness of 0.36 nm (R_q) over $4 \mu\text{m}^2$; (b) talc edge surface with a mean roughness of 0.73 nm (R_q) over $4 \mu\text{m}^2$.

Approaching force profiles between the silicon nitride AFM tip and hydrophobic talc basal plane in 1 mM KCl solutions of varying pH values are shown in Figure 4.4 (a). For all three pH conditions tested, the repulsive interaction dominates between the tip and talc basal plane. The magnitude of electrostatic repulsion increases gradually with increasing pH. The measured force profiles are fitted with the classical DLVO theory as shown by solid curve.

In the fitting process, Stern potential of the tip derived from tip-silica system was used. As can be seen in the typical force curves shown in Figure 4.4 (a), the measured force profiles can be well fitted with the classical DLVO theory down to a separation distance of 5 nm. At pH 5.6, there is an energy barrier at separation distance around 5 nm, as predicted by DLVO theory.

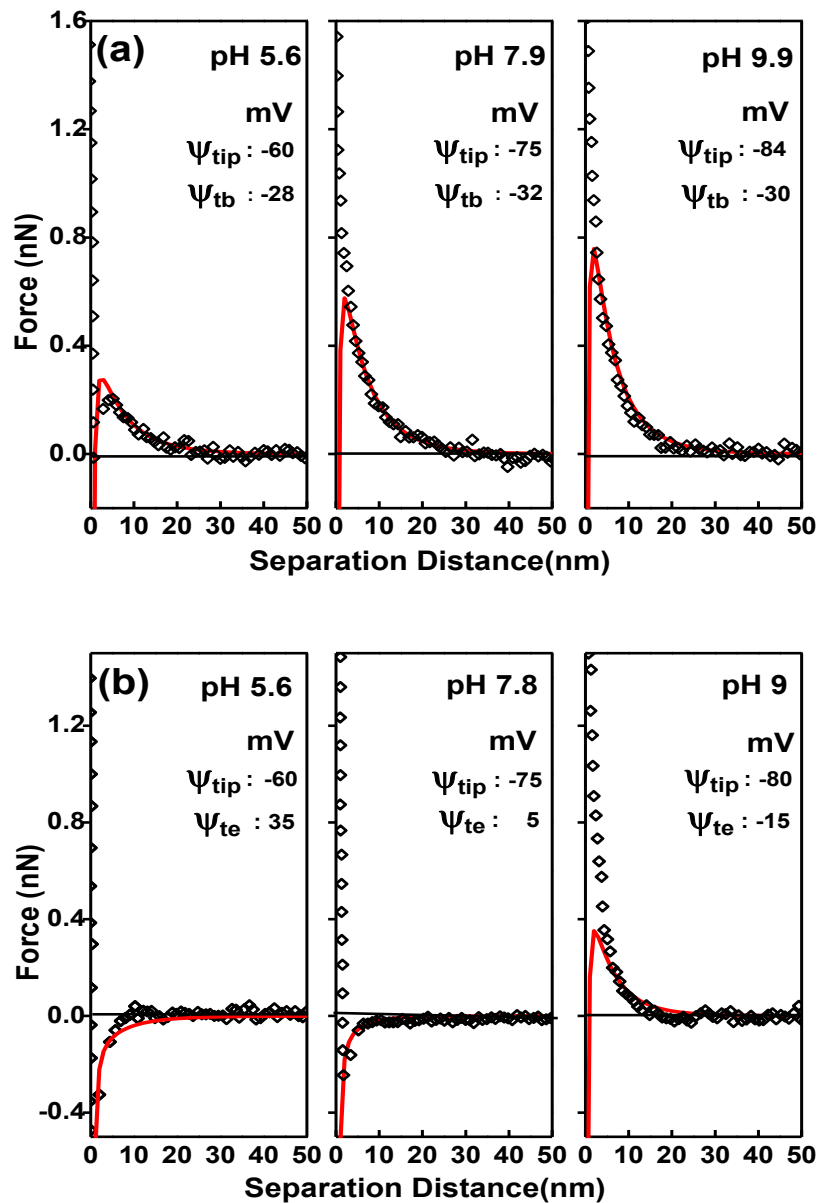


Figure 4.4 Typical interaction force curves (a) between AFM tip and hydrophobic talc basal plane, and (b) between AFM tip and hydrophilic talc edge surfaces, measured in 1 mM KCl solutions of different pH values. Symbols correspond to experimental data. The solid lines represent theoretical fit. Ψ_{tb} and Ψ_{te} are the fitted Stern potential values of the tip, talc basal plane and edge surface, respectively.

It is interesting to note that the energy barrier measured is located at a slightly larger separation distance with a slightly smaller value than that predicted by the classical DLVO theory. Such a deviation suggests the presence of an additional attractive force that is not included in the classical DLVO theory, mostly likely due to the hydrophobic nature of talc basal planes. More importantly, as anticipated, the fitted Stern of talc basal plane is nearly the same, around -30 mV over the solution pH range covered in this study.

A set of typical force profiles between AFM tip and talc edge surfaces in 1 mM KCl solutions of varying pH values is shown in Figure 4.4 (b). As can be seen, the long range interactions are repulsive at pH 9. At pH 7.8 there is no net repulsive force and the force profile becomes purely attractive at pH 5.6. Since the surface of the tip is always negatively charged in the given pH range of this study, the variable interaction force profiles observed at different pH values explicitly suggests that the surface charge of talc edge is highly pH-dependent, changing from negative at pH 9 to positive at pH below 7.8. Again the measured force profiles can be well fitted to classical DLVO theory as shown by solid curves.

The Stern potential values obtained from fitting of force profiles were compared in Figure 4.5 with streaming potential results obtained by Nalaskowski et al.[2]. To our knowledge, such study was the only attempt to reveal the anisotropic character of talc surfaces by measuring streaming potentials of flat basal planes and edge surfaces prepared by sand blasting. In their study, the authors observed an IEP of talc basal planes and edge surfaces both around pH 3. At pH below 5, the ζ potential value of talc edge surfaces and basal planes changed similarly with changing pH. However a slight decrease in ζ potential values of talc edge surfaces with increasing pH above 5 was observed, most likely due to the hydrolysis of magnesium.

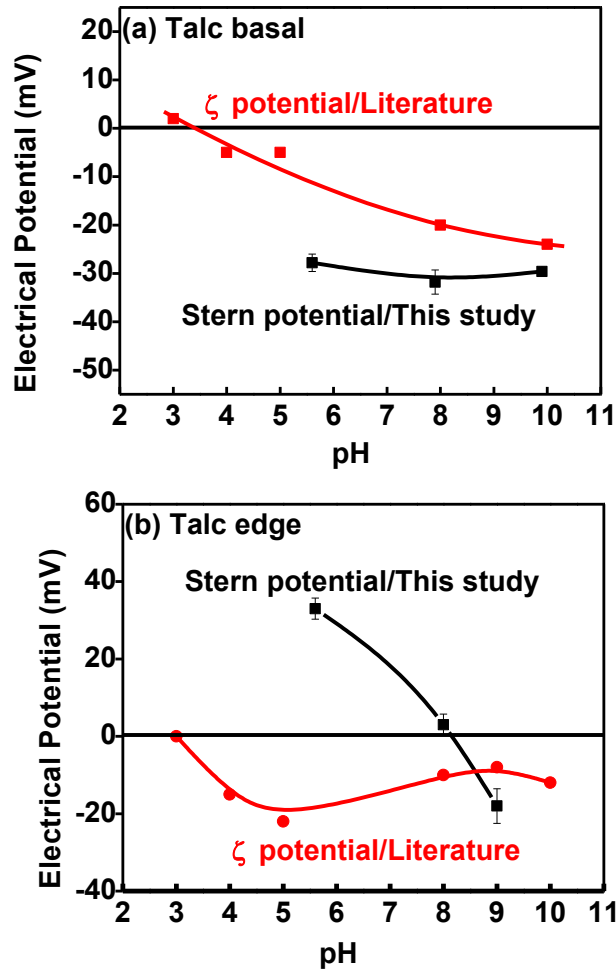


Figure 4.5 Comparison of the Stern potential values, determined by fitting of AFM force profiles in this study with ζ potential values taken from Reference [2] for talc (a) basal planes and (b) edge surfaces in 1 mM KCl of different pH values.

Their ζ potential results are very different from our Stern results obtained from colloidal force measurement. In our study, the Stern of the talc basal plane was found to be largely independent of solution pH, while the Stern potential of the edge surfaces reversed from positive to negative at pH around 8. The discrepancy between these two studies may be a result of difference in the source of materials and method of measurement. As mentioned above, the poorly-defined electrophoretic model for anisotropic particles limits the proper interpretation of

the results from ζ potential measurements on phyllosilicate minerals. In addition, the reported large roughness of surfaces in the mentioned study [2] may also cause unexpected results as the excessively rough surfaces of phyllosilicates make the differentiation of basal planes and edge surfaces extremely difficult. Surface roughness is believed to be most likely the reason for the discrepancy between their predictions and our experimental results. Compared to the small contact area in our measurements, with an R_q value for the surface less than 1 nm over the $4 \mu\text{m}^2$ area, the mean roughness value of the samples prepared by precision diamond saw cutting in the mentioned reference [2] was significantly higher, around 100 nm over a $625 \mu\text{m}^2$ area. Although the sand blasting was used for their further polishing, the folding of talc edge surfaces on each sample was clearly visible. In contrast, by correlating the ζ potential and titration results with the yield stress, Burdukova et al. [17] derived the PZC value of the talc edge surface to be around 8 which is in a remarkable agreement with the results from this study.

4.2.3 Interactions between AFM tip and muscovite surfaces

Representative AFM images of hydrophilic muscovite basal planes and edge surfaces used for force measurements are shown in Figure 4.6. The same color scheme and scanning size for the surface images are used for better comparison. Although prepared using ultramicrotome, the muscovite edge surface having a mean roughness of 0.57 nm, is rougher than a molecularly smooth muscovite basal plane of R_q mean roughness of 0.22 nm. However, the roughness of muscovite edge surface is slightly smaller than the roughness of talc edge surfaces having an R_q mean roughness of 0.72 nm. As in the case of talc, the muscovite edge surfaces prepared as such are suitable for colloidal probing force measurement using AFM tips.

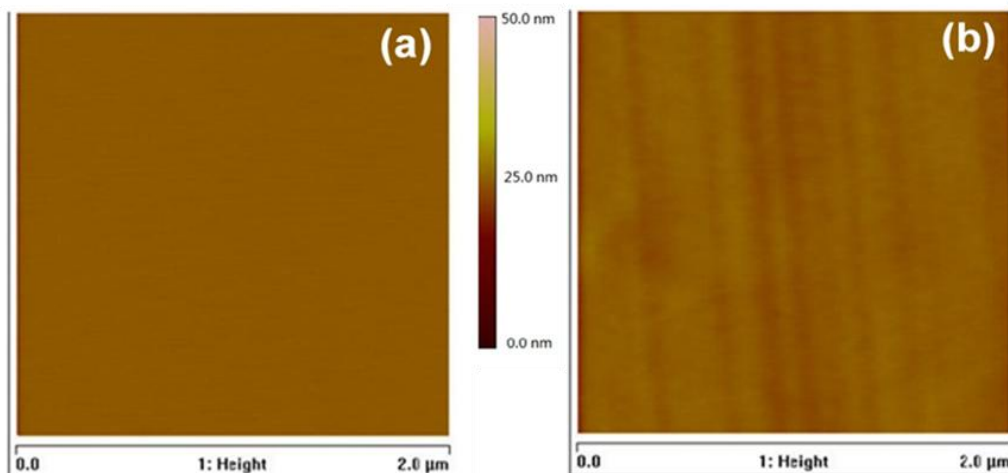


Figure 4.6 Typical AFM images of phyllosilicate planes prepared by microtome cutting technique: (a) muscovite basal plane with a mean roughness of 0.22 nm (Rq) over $4 \mu\text{m}^2$; (b) muscovite edge surface with a mean roughness of 0.57 nm (Rq) over $4 \mu\text{m}^2$.

Force profiles between AFM tip and hydrophilic muscovite basal planes in 1 mM KCl solutions of varying pH values are shown in Figure 4.7 (a). Similar to the talc basal plane, the net interaction forces are all repulsive and increase gradually with increasing pH. Stern potentials of muscovite basal planes obtained from this study are compared in Table 4.2 with the results taken from the literature [3-4, 18-19]. Despite the variety of mica sources and experimental methods, the obtained electrical surface potential values for mica basal planes are in a comparable range.

The structural defects of basal planes, due to the random substitution of lattice Si^{4+} or Al^{3+} by lower valence ions, account for negative charge on the basal plane. This isomorphous substitution is permanent and fixed [20]. The level of substitution depends on the source of phyllosilicates, which may be difficult to determine. The dominant siloxane group (-Si-O-Si-) on the basal plane of 2:1 phyllosilicate is estimated to be essentially inert and has very low affinity to protons in aqueous

media of mild acidity or alkalinity [20]. The observed pH independence of the Stern potential values derived from our experimental colloidal force profiles for both the talc and muscovite basal planes supports the absence of the significant protonation on phyllosilicate basal planes at solution pH studied. The isomorphous substitution is believed to be the main cause for the basal plane charges. In a recent report, Gupta et al. [9] showed that the Stern potential on a silica tetrahedral layer of kaolinite is pH dependent. They attributed the observed pH dependency to the possibility of broken bonds on the basal planes and/or hydrolysis of siloxane bonds in strong acidic and alkaline environment.

Although both phyllosilicate basal surfaces show similar pH-independent properties, the magnitude of the negative Stern potential on muscovite basal planes is nearly twice that on talc basal planes. This means that these two different phyllosilicates have different levels of isomorphous substitution, albeit with the same charge mechanism. For most common mica minerals such as muscovite, the ratio of the Al^{3+} substitution for Si^{4+} on the T basal plane is close to 1:3, which is responsible for highly negative Stern potential values [21]. Talc, in contrast to muscovite, has a much lower isomorphous substitution ratio. Depending on the source, the cation substitution in the tetrahedral layers may vary from 0.01% to 3.4% [22]. The majority of researchers believe that the talc basal plane is almost electrically neutral because of its extremely low isomorphous substitution [18, 21]. Burdukova et al. [17] studied the coagulation behaviour of talc particles by measuring the yield stress of talc suspensions as a function of pH. The coagulation performance strongly indicated the presence of negative charges on talc basal planes. The authors performed a microprobe analysis on the polished thin talc section by analyzing the X-ray emission of each individual element and found the cation substitution ratio in the tetrahedral layer to be as small as 0.38%.

Based on their results, they proposed that even a small degree of isomorphic substitution was sufficient to generate a negative charge on talc basal planes. In their study, only the overall surface potential of both basal planes and edge surfaces was evaluated. The Stern potential on each surface remains unknown. In our study, a trace amount of iron was also detected in talc basal plane as shown by XPS results and the cation substitution in the tetrahedral layer is around 1.9%. It was verified that talc basal planes do carry a definite negative charge by performing direct force measurements on the surface. The magnitude of charges on each surface is determined and quantified. The fitting of measured force profile with the theoretical model may not lead to the exact Stern potential values as only the BC is applied in the calculations. It does however aid in quantitative comparisons of the charge properties of each surface with the consistent use of the same evaluation procedure.

A set of typical force profiles between the tip and the muscovite edge surface in 1 mM KCl solutions of varying pH values is shown in Figure 4.7 (b). These force profiles are similar to the interactions between AFM tip and talc edge surface, as shown in Figure 4.4 (b). The transition from a net attractive to a net repulsive interaction force between the tip and muscovite edge surface is clearly observed. The attractive interaction dominates at pH 5.6. The interaction force is reversed to be repulsive in electrolyte solutions of pH 8 and becomes increasingly more repulsive with further increasing pH up to 9. The observed transition of interaction forces from attractive to repulsive with increasing solution pH strongly suggests that the surface charge of muscovite edges is also pH-dependent. The PZC of the muscovite edge surface is estimated to be between pH 7-8. This value is in an excellent agreement with the PZC value obtained by Zhao et al. [17] who

performed direct colloid probe force measurements on the microtome-prepared muscovite edge surface.

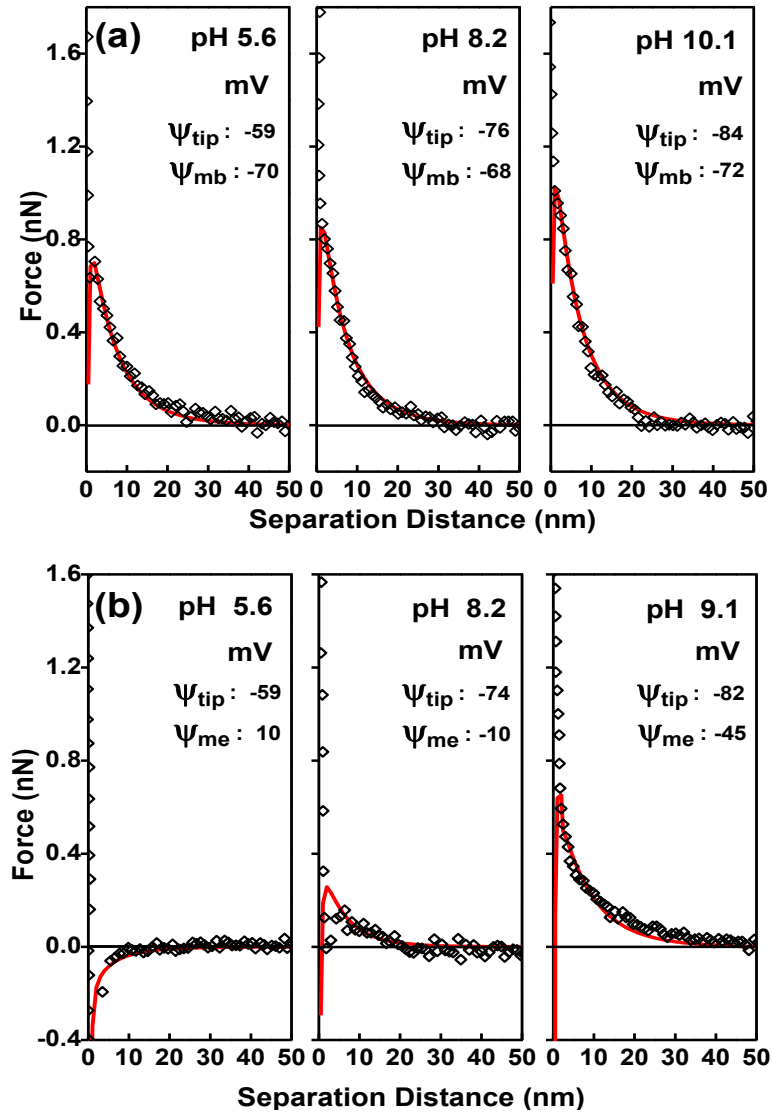


Figure 4.7 Typical AFM interaction force curves measured between (a) AFM tip and muscovite basal plane; (b) AFM tip and muscovite edge surface in 1 mM KCl solutions of various pH values. Symbols correspond to experimental data. The solid lines represent theoretical fit. Ψ_{mb} and Ψ_{me} are the fitted Stern potential values of the tip, muscovite basal plane and edge surface, respectively.

Table 4.2 Comparison of best-fitted Stern potential values of the muscovite basal plane with literature values of mica obtained by MEP, SP measurement and AFM fitting (CP: EDL force was calculated at constant potential BC; CC: EDL force was calculated at constant charge BC).

pH	Electrical potential of muscovite basal plane (mV)			
	This work	From literature		
		Value	Method	Ref
5.6	-70	~-80	AFM	[3]
		~-73	AFM	[4]
		~-68	SP	[23]
		-60 to -90	AFM	
7.9	-68	-60	AFM	[3]
		-60 to -90	AFM	[4]
9.9	-72	~-78	AFM	[3]
		-100	AFM(CP)	[4]
		-58	AFM(CC)	
		-47	SP	

4.2.4 PZC and protonation reactions of different phyllosilicate edge surfaces

The electric charge characteristics of talc and muscovite edge surfaces are similar with a noted exception. At pH 8, a weak repulsive force between AFM tip and muscovite edge surface is observed in contrast to a negligible repulsion between the AFM tip and talc edge surface. This finding suggests a lower PZC of muscovite edge surface than that of the talc edge surface. While the charges on the basal plane are mainly caused by isomorphous substitution of structural ions, the charge on the edge surface is attributed to protonation–deprotonation reactions of the broken primary bonds from the tetrahedral silica and the octahedral

gibbsite/brucite sheets. The basic charging reactions of proton adsorption can be formulated as equation (1.1) as mentioned in Chapter 1.

For many metal oxide minerals, the surface potential can be approximated by the Nernstian equation [19]. The surface potential is positive when the pH of the solution is lower than the PZC and negative when the pH is higher than PZC. As mentioned earlier, the PZC is an important parameter that determines electrochemical phenomena, such as adsorption and coagulation, and controls interactions between phyllosilicate particles. The PZC value of silica is around 2 [13, 24]. The PZC of gibbsite and brucite were reported to be around 8.4-9.1 [14] and 11 [25], respectively. The reported PZC values of phyllosilicate minerals vary widely from pH 1 to 8 depending on the type of phyllosilicates and measurement methods, with the most frequently reported PZC values being observed between pH 6-8.5 [26, 27]. The difference between the reported PZC values can be attributed to different phyllosilicate structures, different degree of isomorphic substitution in phyllosilicate structure and reactive groups on phyllosilicate edge surfaces.

On phyllosilicate edge surfaces, each reactive surface group has its own intrinsic chemical protonation constant (K_H) associated with specific surface sites, e.g., Mg-OH in brucite vs Al-OH in gibbsite. Classical site binding models assume only one type of surface group which is reactive to protons in two consecutive steps, each with its own binding constant to impart surface charges. In general, the difference in protonation constants between the two successive protonation steps of the same surface group is expected to be so large that only one protonation reaction dominates over a given pH window. Therefore, a single protonation reaction is usually sufficient for describing the pristine surface charging [13].

Hiemstra et al. [24] found that even for the same metal hydroxide, different crystal planes may exhibit quite different charging characteristics. They developed a MUltiSiteComplexation (MUSIC) model to include surface heterogeneity. This model involves more than one type of reactive surface groups. The classical site binding models are just the special case of this model [28].

Based on Pauling's bond valence principle [28] and the structure shown in Chapter 1, the possible surface groups on talc and muscovite edges and their corresponding protonation constants taken from literature are listed in Table 4.3 [20, 24-26].

Table 4.3 Possible surface groups on muscovite and talc edge surfaces and their corresponding protonation constants ($\log K_H$) [20, 24-26].

Phyllosilicates	Surface group	$\log K_H$
Muscovite	Si-O ¹⁻	11.9
	Si-OH	-1.9
	SiAl-O ^{1/2-}	-
	Al ₂ -O ¹⁻	12.3
	Al-OH ^{1/2-}	7.9-9.9
	Al ₂ -OH	0-5.2
Talc	Si-O ¹	11.9
	Si-OH	-1.9
	SiMg ₂ -O ^{1/3-}	-
	Mg-OH ^{2/3-}	10
	Mg ₂ -OH ^{1/3-}	-

Since the absolute value of charges of surface species is allowed only to be equal to or lower than one in aqueous solutions [26], Mg-O^{5/3-} and Al-O^{3/2-} are not

found at the interface in aqueous solutions. At least three types of surface groups (singly, doubly and triply coordinated) may be found on talc or muscovite edge surfaces. The groups that populate a talc edge surface are Si-OH, Si-O¹⁻, SiMg₂-O^{1/3-}, Mg₂-OH^{1/3-} and Mg-OH^{2/3-}, and on muscovite edge surfaces they are Si-OH, Si-O¹⁻, SiAl-O^{1/2-}, Al₂-O¹⁻, Al₂-OH, and Al-OH^{1/2-}. The singly coordinated group is nearly always protonated due to its large protonation constant and is considered to dominate the charging mechanism of the surface. The SiOH group from the tetrahedral sheet has a log K_H equal to -1.9, indicating a significantly protonated surface only at H⁺ concentration greater than almost 10^{1.9} (79.4) mol/L, which is unrealistic as considering the fact that mole concentration of the pure HCl is just 40.9 mol/L. Therefore, the de-protonation of Si-OH to Si-O¹⁻ contributes to negative surface charges observed in the pH range studied. The major protonation reactions on talc and muscovite edge surfaces are expected to come from Mg-OH^{2/3-} and Al-OH^{1/2-} surface groups, respectively.

According to literature [28], both Mg-OH^{2/3-} and Al-OH^{1/2-} sites become positively charged at pH values lower than 10, through the following site binding reactions:



Different protonation constants of Al-OH^{1/2-} were derived from calculations using different site binding models. The protonation constant of Al-OH^{1/2-} is often considered to be lower than that of Mg-OH^{2/3-}, which accounts for lower PZC values of gibbsite than that of brucite [24-25]. Since the positive charges on talc and muscovite edge surfaces are mainly attributed to the protonation of singly

coordinated $\text{Mg-OH}^{2/3-}$ and $\text{Al-OH}^{1/2-}$ groups, respectively, the difference in the protonation constants of these two edge surface groups explains why at a given pH talc edge surface is more positively charged than muscovite edge surface, leading to a higher PZC value for talc edge surface than for muscovite edge surface. In addition to protonation reactions of the singly coordinated groups on phyllosilicate edge surfaces, the doubly coordinated surface groups, such as $\text{SiAl-O}^{1/2-}$, $\text{Al}_2\text{-OH}$, $\text{Al}_2\text{-O}^{1-}$ and $\text{Mg}_2\text{-OH}^{1/3-}$, may also become protonated or deprotonated at a given pH. For example, a proton can be attached to an $\text{Al}_2\text{-OH}$ group at low pH to become $\text{Al}_2\text{-OH}_2^+$. The protonation of $\text{Al}_2\text{-OH}$, $\text{SiAl-O}^{1/2-}$ or $\text{Mg}_2\text{-OH}^{1/3-}$ surface groups, therefore also contributes to positive charges on edge surfaces. However, the reactivity of these doubly coordinated surface groups is believed to be suppressed by a singly coordinated group at high pH [26]. At present, there is no well-accepted theoretical estimation or experimental determination of the protonation constant for such transitional groups as $\text{SiMg}_2\text{-O}^{1/3-}$ and $\text{SiAl-O}^{1/2-}$. Proton adsorption at a triply coordinated surface group does not occur over the normal pH range encountered as its protonation constant is extremely low [24]. As a result, the influence on surface charge from this kind of groups can be neglected.

The increased dissolution of structural metal hydroxide with decreasing pH or specific adsorption of Mg^{2+} on the talc edge surface may also contribute to the observed difference in the PZC values between talc and muscovite edge surfaces [24, 29]. Although it is believed that protons at low pH and hydroxyl groups at high pH participate in the dissolution process, the detailed dissolution mechanism of metal hydroxides remains to be established [24, 26].

4.3 Summary

Thanks to the state-of-the-art ultramicrotome to prepare sufficiently smooth talc and muscovite edge surfaces, commercial AFM tips are used in commercial scanning probe microscope to quantitatively probe the surface charge properties of two typical 2:1 layer phyllosilicates: talc and muscovite. The surface roughness provided by this technique is much lower than other sample preparation methods such as sandblasting or precision diamond saw cutting.

The measured interaction force profiles between AFM tip and phyllosilicate basal planes and edge surfaces were fitted with the classical DLVO theory without incurring complex finite element analysis applied to reconstruct surfaces. On the basis of measured interaction forces between the tip and different phyllosilicate surfaces, the Stern potential of talc and muscovite surfaces are determined. The basal planes of talc are found to carry a permanent negative charge while the charges on its edge surfaces are highly pH-dependent.

The long range interaction forces between AFM tip and talc edge surfaces are repulsive at pH 9, reduces to nearly zero at pH 8.0 and be attractive at pH 5.6. It is the first time that the magnitudes of Stern potential of the talc edge surface is determined by direct force measurement. The similar trend has been observed for basal plane and edge surfaces of muscovite. However, the basal plane of muscovite has been found to be much more negative than that of talc, attributed to a much higher isomorphic substitution in muscovite than in talc. The PZC of muscovite edge surface, on the other hand, is lower than the corresponding PZC for the edge surfaces of talc, which is attributed to higher protonation constant of magnesium hydroxide in talc than aluminum hydroxide in muscovite.

4.4 References

- [1] Long, J., Xu, Z., Mashyah, J. H., 2006, "Role of Illite-Illite Interactions in Oil Sands Processing," *Colloids and Surfaces A-Physicochemical and Engineering Aspects*, 281(1-3) pp. 202-214.
- [2] Nalaskowski, J., Abdul, B., Du, H., Miller, J. D., 2007, "Anisotropic Character of Talc Surfaces as Revealed by Streaming Potential Measurements, Atomic Force Microscopy, Molecular Dynamics Simulations and Contact Angle Measurements," *Canadian Metallurgical Quarterly*, 46(3) pp. 227-235.
- [3] Hartley, P. G., Larson, I., Scales, P. J., 1997, "Electrokinetic and Direct Force Measurements between Silica and Mica Surfaces in Dilute Electrolyte Solutions," *Langmuir*, 13(8) pp. 2207-2214.
- [4] Zhao, H., Bhattacharjee, S., Chow, R., Wallace, D., Masliyah, J. H., Xu, Z., 2008, "Probing Surface Charge Potentials of Clay Basal Planes and Edges by Direct Force Measurements," *Langmuir*, 24(22) pp. 12899-12910.
- [5] Wallqvist, V., Claesson, P. M., Swerin, A., Schoelkopf, J., Gane, P. A. C., 2007, "Interaction Forces between Talc and Pitch Probed by Atomic Force Microscopy," *Langmuir*, 23(8) pp. 4248-4256.
- [6] Chi, R., Xu, Z., DiFeo, T., Finch, J. A., Yordan, J. L., 2001, "Measurement of Interaction Forces between Talc and Toner Particles," *Journal of Pulp and Paper Science*, 27(5) pp. 152-157.
- [7] Lin, X. Y., Creuzet, F., Arribart, H., 1993, "Atomic Force Microscopy for Local Characterization of Surface Acid-Base Properties," *Journal of Physical Chemistry*, 97(28) pp. 7272-7276.
- [8] Yin, X., Drelich, J., 2008, "Surface Charge Microscopy: Novel Technique for Mapping Charge-Mosaic Surfaces in Electrolyte Solutions," *Langmuir*, 24(15) pp. 8013-8020.
- [9] Gupta, V., Miller, J. D., 2010, "Surface Force Measurements at the Basal Planes of Ordered Kaolinite Particles," *Journal of Colloid and Interface Science*, 344(2) pp. 362-371.
- [10] Long, J., Xu, Z., Masliyah, J. H., 2006, "Adhesion of Single Polyelectrolyte Molecules on Silica, Mica, and Bitumen Surfaces," *Langmuir*, 22(4) pp. 1652-1659.

- [11] Drelich, J., Long, J., Yeung, A., 2007, "Determining Surface Potential of the Bitumen-Water Interface at Nanoscale Resolution using Atomic Force Microscopy," *Canadian Journal of Chemical Engineering*, 85(5) pp. 625-634.
- [12] Drelich, J., Long, J., Xu, Z., Masliyah, J. H., White, C. L., 2006, "Probing Colloidal Forces between a Si_3N_4 AFM Tip and Single Nanoparticles of Silica and Alumina," *Journal of Colloid and Interface Science*, 303(2) pp. 627-638.
- [13] King, R. P., 1982, "Principles of Flotation," South African Institute of Mining and Metallurgy, Johannesburg.
- [14] Parks, G. A., Bruyn, P. L. D., 1962, "Zero Point of Charge of Oxides," *Journal of Physical Chemistry*, 66(6) pp. 967.
- [15] Liu, J., Xu, Z., Masliyah, J. H., 2003, "Studies on Bitumen-Silica Interaction in Aqueous Solutions by Atomic Force Microscopy," *Langmuir*, 19(9) pp. 3911-3920.
- [16] Cerovic, L. S., Milonjic, S. K., Bahloul-Hourlier, D., Doucey, B., 2002, "Surface Properties of Silicon Nitride Powders," *Colloids and Surfaces A-Physicochemical and Engineering Aspects*, 197(1-3) pp. 147-156.
- [17] Burdukova, E., Becker, M., Bradshaw, D. J., Laskowski, J. S., 2007, "Presence of Negative Charge on the Basal Planes of New York Talc," *Journal of Colloid and Interface Science*, 315(1) pp. 337-342.
- [18] Van Olphen, H., 1963, "An Introduction to Clay Colloid Chemistry, for Clay Technologists, Geologists, and Soil Scientists," Interscience Publishers, New York.
- [19] Brant, J. A., Johnson, K. M., Childress, A. E., 2006, "Examining the Electrochemical Properties of a Nanofiltration Membrane with Atomic Force Microscopy," *Journal of Membrane Science*, 276(1-2) pp. 286-294.
- [20] Avena, M. J., Mariscal, M. M., De Pauli, C. P., 2003, "Proton Binding at Clay Surfaces in Water," *Applied Clay Science*, 24(1-2) pp. 3-9.
- [21] Bergaya, F., Theng, B. K. G., Lagaly, G., 2006, "Handbook of Clay Science," Elsevier, Amsterdam; London.
- [22] Deer, W. A., Howie, R. A., Zussman, J., 1962, "Rock-Forming Minerals," Longmans, London.

- [23] Toikka, G., Hayes, R. A., 1997, "Direct Measurement of Colloidal Forces between Mica and Silica in Aqueous Electrolyte," *Journal of Colloid and Interface Science*, 191(1) pp. 102-109.
- [24] Lützenkirchen, J., 2006, "Surface Complexation Modelling," Academic Press, Amsterdam; London.
- [25] Jodin, M. C., Gaboriaud, F., Humbert, B., 2005, "Limitations of Potentiometric Studies to Determine the Surface Charge of Gibbsite Gamma-Al(OH)₃ Particles," *Journal of Colloid and Interface Science*, 287(2) pp. 581-591.
- [26] Pokrovsky, O. S., Schott, J., 2004, "Experimental Study of Brucite Dissolution and Precipitation in Aqueous Solutions: Surface Speciation and Chemical Affinity Control," *Geochimica Et Cosmochimica Acta*, 68(1) pp. 31-45.
- [27] Taubaso, C., Afonso, M. D., Sanchez, R. M. T., 2004, "Modelling Soil Surface Charge Density using Mineral Composition," *Geoderma*, 121(1-2) pp. 123-133.
- [28] Hiemstra, T., Vanriemsdijk, W. H., Bolt, G. H., 1989, "Multisite Proton Adsorption Modeling at the Solid-Solution Interface of (Hydr)Oxides-a New Approach.1. Model Description and Evaluation of Intrinsic Reaction Constants," *Journal of Colloid and Interface Science*, 133(1) pp. 91-104.
- [29] Alvarez-Silva, M., Uribe-Salas, A., Mirnezami, M., Finch, J. A., 2010, "The Point of Zero Charge of Phyllosilicate Minerals using the Mular-Roberts Titration Technique," *Minerals Engineering*, 23(5) pp. 383-389.

Chapter 5

Interaction of divalent cations with basal planes and edge surfaces of phyllosilicate minerals*

Following the systematically study of the effect of pH on the anisotropic surface charge characteristic of talc and muscovite in Chapter 4, the work presented in this chapter comprises a detailed study on the effect of two divalent cations (Ca^{2+} and Mg^{2+}) on the surface charge characteristic of different surfaces of phyllosilicate minerals by the direct interaction force measurements using AFM.

The AFM measurements were conducted in 1 mM KCl background solutions at pH 8.5 as a function of divalent cation concentration. The fitted Stern potentials of the muscovite basal plane become less negative with increasing Ca^{2+} or Mg^{2+} concentration but do not reverse its sign even at Ca^{2+} or Mg^{2+} concentrations up to 5 mM. In contrast, the Stern potentials of the muscovite edge surface reverse at Ca^{2+} or Mg^{2+} concentrations as low as 0.1 mM. The Stern potentials of talc basal planes become less negative with 0.1 mM Ca^{2+} addition and nearly zero with 1 mM Ca^{2+} addition. The Stern potentials of talc edge surfaces become reverse with 0.1 mM Ca^{2+} or 1 mM Mg^{2+} addition, showing not only a different binding mechanism of talc basal planes and edge surfaces with Ca^{2+} and Mg^{2+} , but also different binding mechanism between Ca^{2+} and Mg^{2+} ions with basal planes and edge surfaces.

5.1 Introduction

The multivalent cations were reported to promote homocoagulation of mineral particles and hence to increase the efficiency of mineral recovery [1-6]. The presence of multivalent cations in solution is known to compress more

* Yan, L., Masliyah, J. H., Xu, Z., 2013, Journal of Colloid and Interface Science (Accepted).

significantly the EDL of the charged particles than monovalent electrolytes, therefore reducing the EDL repulsive forces between the mineral particles. This effect is often referred to as double layer compression. The adsorption of metal ions and/or their hydroxyl species on the mineral surface can often lead to a more significant effect on the colloidal behaviour of mineral particles than the EDL compression. Taking the oil sands processing as an example, the detrimental effect of divalent cations on the overall bitumen recovery from oil sands by hot water based extraction process has been reported extensively [1-6]. A dramatic reduction in bitumen recovery was observed when processing certain types of ores in the presence of over 1 mM Ca^{2+} or Mg^{2+} in the solution. The depression of bitumen recovery was attributed to the slime coating of negatively charged bitumen by clays with divalent cations acting as the bridge, making the bitumen surface more clay like and hence difficult to attach to air bubbles [1, 2]. More interestingly, Kasongo et al. [3] observed that only the co-presence of montmorillonite and Ca^{2+} presented over 1 mM concentration in the solution had a detrimental effect on bitumen recovery, while other clay minerals such as kaolinite and illite were less detrimental. Similar to their finding, Liu et al. [4] observed that kaolinite was weakly attached to the bitumen surface when 1 mM Ca^{2+} was added in the solution, in contrast to strong adhesion of montmorillonite to the bitumen surface in the presence of the same amount of Ca^{2+} . Similar effect of clays and divalent cations on coal flotation was also reported [7]. Divalent Ca^{2+} and Mg^{2+} cations are both hydrolysable metal ions and can undergo hydrolysis at specific concentrations and pH values. It was reported that the enhancement in fine particle coagulation of some minerals was significant only when these metal cations were in the form of more hydroxyl species such as $\text{Ca}(\text{OH})^+$ and $\text{Mg}(\text{OH})^+$ [5-6]. This finding suggests that instead of metal ions themselves, the

specific adsorption of metal mono hydroxyl species on the clay surfaces was responsible for the reduction in bitumen recovery [5]. Gan et al. [6] reported that only the metal mono hydroxyl species may have a significant effect on the heterocoagulation between the bitumen and silica.

Though the detrimental effect of divalent metal cations such as Ca^{2+} and Mg^{2+} on bitumen recovery is already well recognized, there is no consensus reached regarding how this kind of hydrolysable divalent cations affects the surface property of specific mineral surfaces. Until now, there is no direct measurement on how different divalent metal ions interact with basal plane and edge surfaces of phyllosilicate minerals. The major hurdle to systematically study the interaction of metal cations with phyllosilicates is that this type of minerals has distinct anisotropic surface properties as well described in chapter 1. This distinct anisotropic character of phyllosilicate surface chemistry and hence surface charge makes the study of metal ion interactions with phyllosilicate minerals extremely difficult if not impossible, despite its critical importance, mainly due to the lack of tools to study the basal plane and edge surfaces independently.

As well described in Chapter 3, sufficiently smooth edge surfaces of different phyllosilicate minerals were successfully prepared using an ultramicrotome cutting method, which makes the study on anisotropic charge properties of phyllosilicate minerals at nano-scale resolution possible. As presented in Chapter 4, the surface charge characteristics of the basal plane and edge surfaces of two different phyllosilicate minerals in simply electrolyte solutions as a function of solution pH were investigated, which demonstrates the capable of AFM tip to independently probe surface charge properties on these specific surfaces.

In this chapter, the interactions of two divalent cations with basal planes and edge

surfaces of two different phyllosilicates by direct colloidal force measurements using AFM have been investigated, aiming to provide fundamental insights on the charging mechanisms and interaction characteristics of each phyllosilicate surfaces with divalent cations, and to better understand how these anisotropic surface charge properties influence the colloidal behaviour of aqueous phyllosilicate mineral suspensions. Ca^{2+} and Mg^{2+} are chosen here, as among all cations high levels of Ca^{2+} and Mg^{2+} are frequently encountered in many practical systems [8].

5.2 Results and discussion

5.2.1 Interactions between AFM tip and silica surfaces

Since the Stern potential or ζ potential values of silica have been extensively studied, silica was used to calibrate/determine the Stern potential of AFM tip in divalent cation solutions by measuring colloidal forces between the tip and a clean silica wafer in corresponding solutions. As the isotropic particle, the ζ potential values of silica (Aldrich Inc.) determined using Zetasizer (Nano ZS, Malvern Instruments, U.K.) have been used as the approximation of the Stern potential of silica to calibrate the Stern potential of the AFM tip by fitting the measured interaction force profiles. For each concentration, the ζ potential measurement was carried out for at least 10 times at the same conditions and the average value was reported. As shown in Figure 5.1, in 1 mM KCl solutions without Ca^{2+} or Mg^{2+} addition at pH of 8.5, the ζ potential of silica nano particles is -56 mV. When 0.1 mM Ca^{2+} is added to the solution at the same pH, the ζ potential of silica particles become less negative at around -33 mV, increases further to about -24 mV and -17 mV when 1 mM and 5 mM Ca^{2+} are added, respectively. Very similar trend in ζ potential changes of silica particles has been found in response to Mg^{2+} addition.

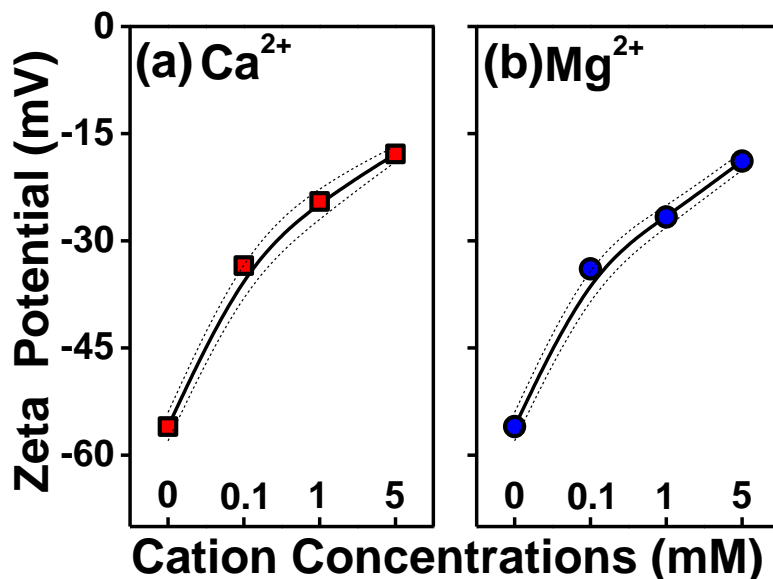


Figure 5.1 ζ potential values of silica particles in 1 mM KCl solutions at pH 8.5 containing various concentrations of (a) Ca^{2+} and (b) Mg^{2+} , determined by electrophoresis method.

As shown in Figure 5.2 (a), for all Ca^{2+} concentrations (0, 0.1 mM, 1 mM and 5 mM) tested, the interaction forces are monotonically repulsive on approach. The long range repulsive forces between the tip and the silica surface are depressed significantly and progressively by adding 0.1 mM more Ca^{2+} ions. When the concentration of Ca^{2+} reached 5 mM, the long range interaction forces, albeit very weak, were still repulsive. Figure 5.2 (b) shows interaction force profiles between the AFM tip and the silica surface at different concentrations of Mg^{2+} in 1 mM KCl solutions at pH 8.5. Similar to the case of Ca^{2+} addition, the long range repulsive forces are dramatically reduced by the addition of a small amount of Mg^{2+} . Compared to Ca^{2+} , the repulsive interaction force between the tip and the silica surface is less depressed by adding the same mole concentration of Mg^{2+} .

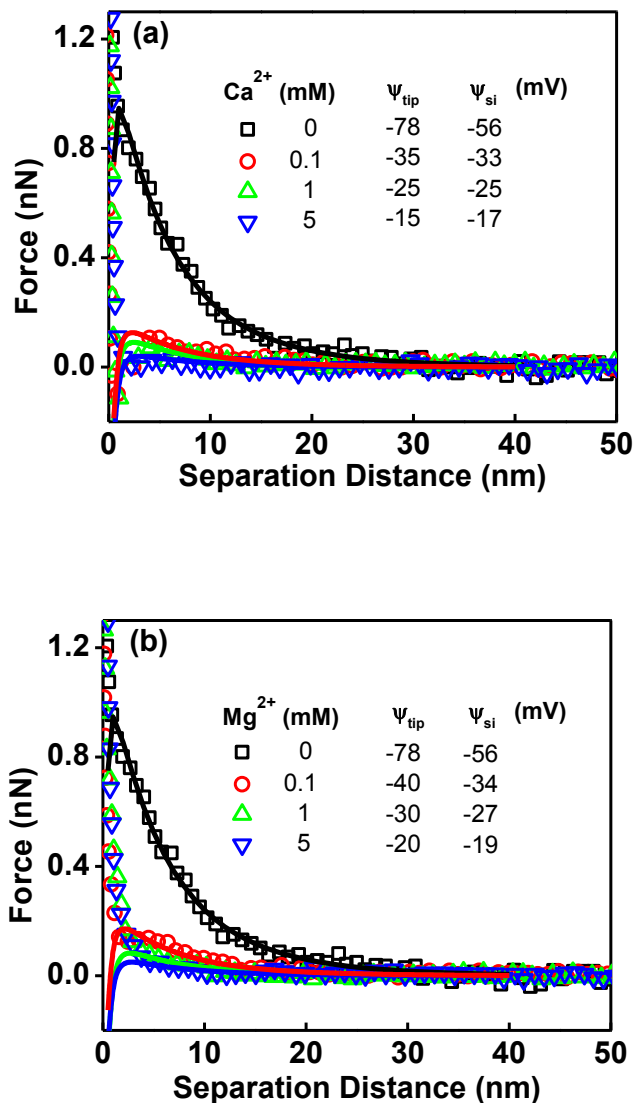


Figure 5.2 Typical AFM interaction force profiles measured between AFM silicon nitride tip and silica wafer surface in 1 mM KCl solutions containing various concentrations of (a) Ca²⁺ and (b) Mg²⁺ at pH 8.5. Symbols correspond to experimental data. The solid lines represent theoretical fit with the fitted Stern potential values of the tip being given in the legends. ψ_{tip} and ψ_{si} are the Stern potential values of AFM tip and silica, respectively.

Ebeling et al. [9] reported similar trends for the interaction force profiles between the AFM silicon tip and the silicon wafer in both MgCl_2 and CaCl_2 solutions as determined by dynamic force spectroscopy. In their study, the change of the repulsive force to attractive force between the tip and the silica wafer did not occur until the concentrations of both divalent cations were above 10 mM, which is beyond the concentration range of practical importance and hence not explored in the current study.

The measured force profiles shown in Figure 5.2 were fitted to the classical DLVO theory in which the Stern potentials of silica in the corresponding solutions were approximated by the ζ potential values measured by electrophoresis method. A MATLAB (The Math Works Inc.) program was developed for calculation of interaction forces and used for the fitting process. As shown in Figure 5.2, the experimentally measured force profiles between the tip and the silica surface in various electrolyte solutions (symbols) are found to be fitted quite well with the classical DLVO theory (solid curves), particularly for separation distances larger than 4-5 nm. The discrepancy at very short separation distances is probably due to the presence of repulsive non-DLVO forces, more likely the hydration force between the hydrophilic silica surface and silicon nitride tip, which is not considered in the classical DLVO model used in the fitting of the force profiles.

The Stern potentials of tip calibrated by the silica wafer were further used to evaluate the AFM interaction force profiles between the tip and the specific phyllosilicate surface in 1 mM KCl background solutions as a function of divalent cation concentration. To better verify this evaluation procedure, the fitted Stern potential values of the silicon nitride AFM tip is compared with the ζ potential

values of silicon nitride nano particles (Aldrich Inc.) determined using Zetasizer (Nano ZS, Malvern Instruments, U.K.). As shown in Figure 5.3 (a), the ζ potentials of silicon nitride nano particle also become less negative changing from -50 mV in 1 mM KCl solutions to around -31 mV with 0.1 mM Ca^{2+} addition, further increase to around -20 mV and -14 mV with 1 mM and 5 mM Ca^{2+} addition, respectively. Similar trend was found for the Mg^{2+} ions. As shown clearly in Figure 5.3, the ζ potential of silicon nitride in response to the addition of divalent cations shows a similar trend as the Stern potential derived from the AFM force profiles: both becoming increasingly less negative with increasing the concentration of divalent cations. Such agreement confirms the suitability of applying our current tip-substrate system to study interactions of divalent cations with specific phyllosilicate surfaces.

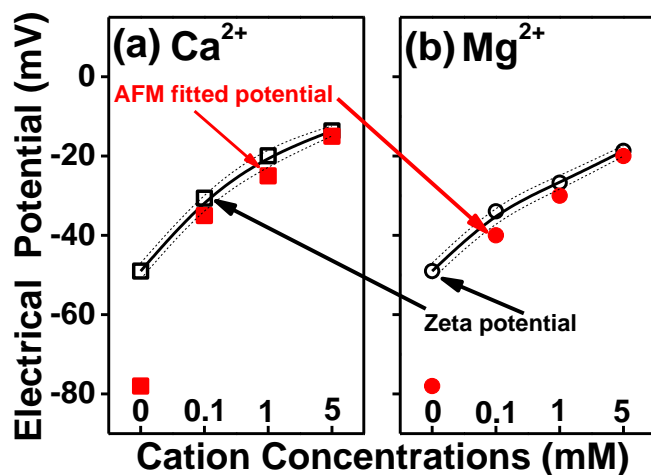


Figure 5.3 Comparison of the Stern potentials (solid symbol) of AFM silicon nitride tip determined by fitting of AFM force profiles with ζ potential values (open symbol) determined for silicon nitride nano particles by electrophoresis method in 1 mM KCl solutions containing various concentrations of (a) Ca^{2+} and (b) Mg^{2+} at pH 8.5.

Theoretically, the addition of 0.1 mM, 1 mM and 5 mM divalent cations to 1 mM simple electrolyte (KCl) solution would reduce the thickness of the EDL around charged particles from 9.6 nm to 6.5, 4.8 and 2.8 nm, respectively. These values are also used for data fitting. The compression of the EDL due to the addition of divalent cations in the solution, especially at higher divalent cation concentration leads to lower electrostatic repulsion, as shown in Figure 5.3. It should be noted that the magnitude of the ζ potential values is slightly lower than the corresponding Stern potential values derived by fitting of AFM force profiles to the classical DLVO theory, more so at lower divalent cation ion concentrations. This discrepancy between the two data sets is anticipated from the definition of ζ potential and Stern potential which is measured at a much closer location to the surface than ζ potential. When compressed more of the EDL by adding more divalent cations, a reduced difference between the Stern potential and ζ potential is anticipated as shown in Figure 5.3.

5.2.2 Interactions between AFM tip and different muscovite surfaces

Typical interaction force profiles between AFM tip and the hydrophilic muscovite basal plane in 1 mM KCl solutions of varying Ca^{2+} concentrations at pH 8.5 are shown in Figure 5.4 (a). The long range repulsion is drastically depressed upon the addition of a small amount of Ca^{2+} ions (0.1 mM) and continued to decrease with increasing Ca^{2+} concentrations to 1 mM and 5 mM. However, the interaction forces remain monotonically repulsive. A qualitatively similar effect of Mg^{2+} concentrations on the interaction force profiles between AFM tip and muscovite basal plane in 1 mM KCl solutions at the given pH of 8.5 is observed.

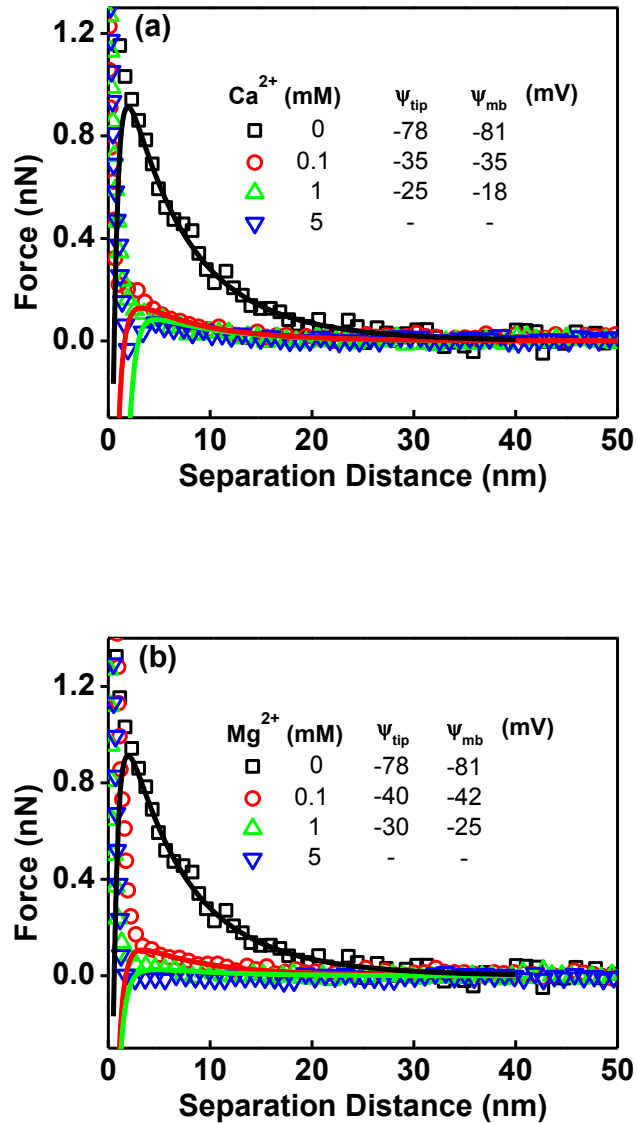


Figure 5.4 Typical AFM interaction force profiles measured between AFM tip and muscovite basal planes in 1 mM KCl solutions of various (a) Ca²⁺ and (b) Mg²⁺ concentrations at pH 8.5. Symbols correspond to experimental data. The solid lines represent theoretical fits of classical DLVO theory. ψ_{tip} and ψ_{mb} are the Stern potential values of AFM tip and the muscovite basal plane, respectively.

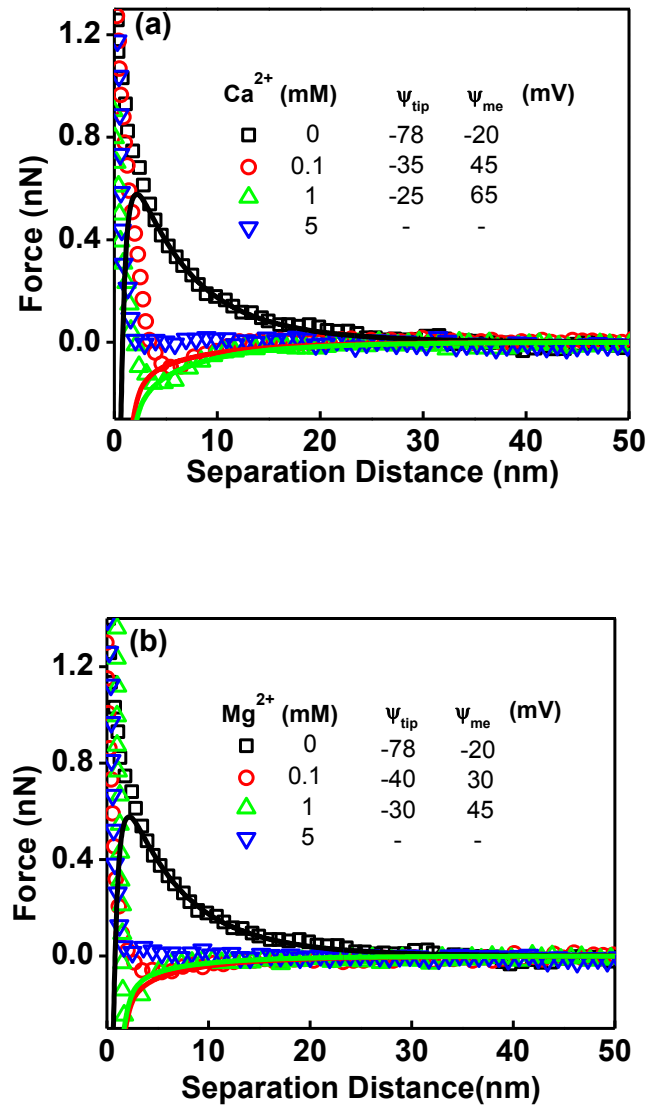


Figure 5.5 Typical AFM interaction force profiles measured between AFM tip and muscovite edge surfaces in 1 mM KCl solutions containing (a) Ca^{2+} and (b) Mg^{2+} at pH 8.5. Symbols correspond to experimental data. The solid lines represent theoretical fit to the classical DLVO theory. ψ_{tip} and ψ_{me} are the Stern potential values of AFM tip and the muscovite edge surface, respectively.

As shown in Figure 5.4 (b), the long range repulsion between the AFM tip and muscovite basal plane is drastically depressed by the addition of 0.1 mM Mg^{2+} ions and continues to decrease slightly when Mg^{2+} concentrations is increased to 1 mM. When Mg^{2+} is further increased to 5 mM, the long range repulsive force becomes almost negligible. Butt [10] reported a similar effect of divalent cations on the interaction forces between the AFM silicon nitride tip and the cleaved mica surface that the interaction force remains repulsive in 3 mM MgCl_2 solution and becomes negligible at higher MgCl_2 concentrations.

Typical interaction force profiles between the AFM tip and the muscovite edge surface in 1 mM KCl solutions of varying Ca^{2+} concentrations are shown in Figure 5.5 (a). In contrast to the basal plane, the long range interaction forces between the tip and muscovite edge surface reverse from strong repulsive to net attractive upon the addition of 0.1 mM Ca^{2+} in solution. This attraction increases further with increasing Ca^{2+} concentration up to 1 mM. A further increase in Ca^{2+} concentrations up to 5 mM decreases the attractive force to a negligible value.

Typical interaction force profiles between the AFM tip and the muscovite edge surface in 1 mM KCl solutions containing varying concentrations of Mg^{2+} are shown in Figure 5.5 (b). While monotonically repulsive in 1 mM KCl solutions, an attraction is observed between the AFM tip and the muscovite edge surface with 0.1 mM Mg^{2+} ion addition. This attraction increases further with increasing Mg^{2+} concentration up to 1 mM before becoming almost negligible at the Mg^{2+} concentration reaching 5 mM.

5.2.3 Interactions between AFM tip and different talc surfaces

Typical interaction force profiles between AFM tip and the hydrophobic talc basal plane in 1 mM KCl solutions of varying Ca^{2+} concentrations at pH 8.5 are shown in

Figure 5.6 (a). The long range repulsion is depressed significantly with Ca^{2+} addition even at very low concentration of 0.1 mM and reduces to be almost negligible by increasing the Ca^{2+} concentration to 1 mM. Figure 5.6 (b) shows the effect of the Mg^{2+} concentration on the interaction force profiles between AFM tip and the talc basal plane in the 1 mM KCl solutions of pH 8.5. The long range repulsion between the tip and the talc basal plane is also depressed with 0.1 mM Mg^{2+} addition. Unlike the case with Ca^{2+} addition at the same mole concentration, the measured long range interaction forces remains repulsive although to a less extend with the 1 mM Mg^{2+} addition. The repulsive force becomes negligible when the Mg^{2+} concentrations are increased to 5 mM and above.

Typical interaction force profiles between AFM tip and talc edge surfaces in 1 mM KCl solutions of varying Ca^{2+} concentrations are shown in Figure 5.7 (a). Similar to the case of the muscovite edge surfaces shown in Figure 5.5 (a), the long range interaction force between AFM tip and talc edge surfaces reverses from strong repulsion to net attraction in the presence of 0.1 mM Ca^{2+} in solution. The attractive force further increases with increasing Ca^{2+} concentration to 1 mM before it become nearly negligible at Ca^{2+} concentration of 5 mM.

Figure 5.7 (b) shows the effect of the Mg^{2+} concentration on the interaction force profiles between AFM tip and the talc edge surface in 1 mM KCl solutions of pH 8.5. The long range interaction forces between AFM tip and the talc edge surface are reduced significantly upon the addition of 0.1 mM Mg^{2+} , reversed from repulsive to attractive at Mg^{2+} concentration of 1 mM before becoming almost zero with further increasing Mg^{2+} concentrations to 5 mM.

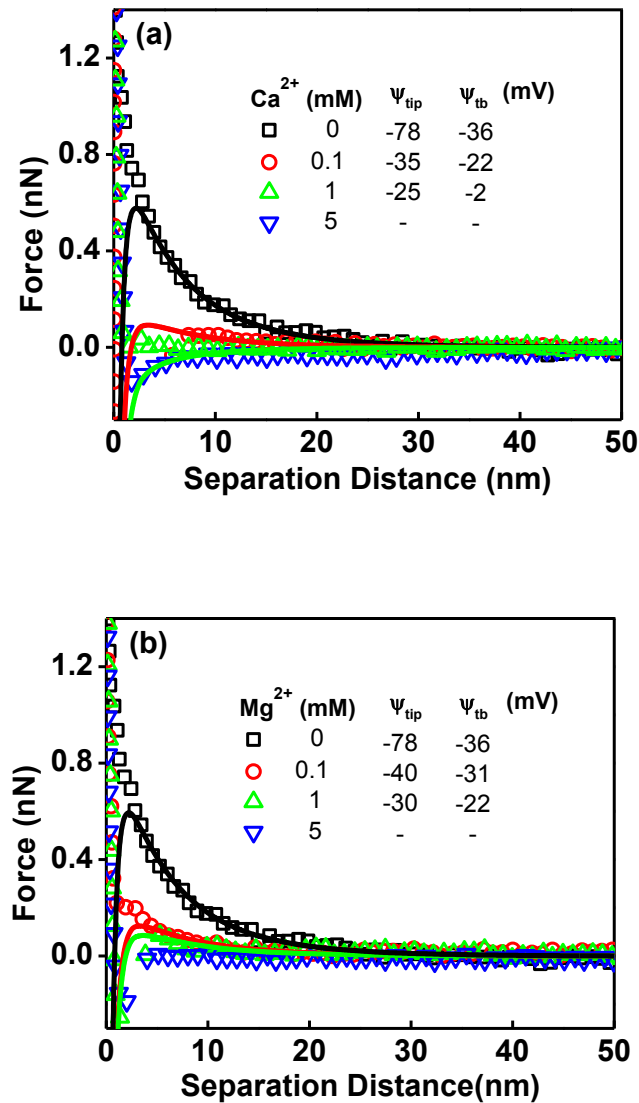


Figure 5.6 Typical AFM interaction force profiles measured between AFM tip and talc basal planes in 1 mM KCl solutions of various (a) Ca^{2+} and (b) Mg^{2+} concentrations at pH 8.5. Symbols correspond to experimental data. The solid lines represent theoretical fit of classical DLVO theory. ψ_{tip} and ψ_{tb} are the Stern potential values of AFM tip and talc basal plane, respectively.

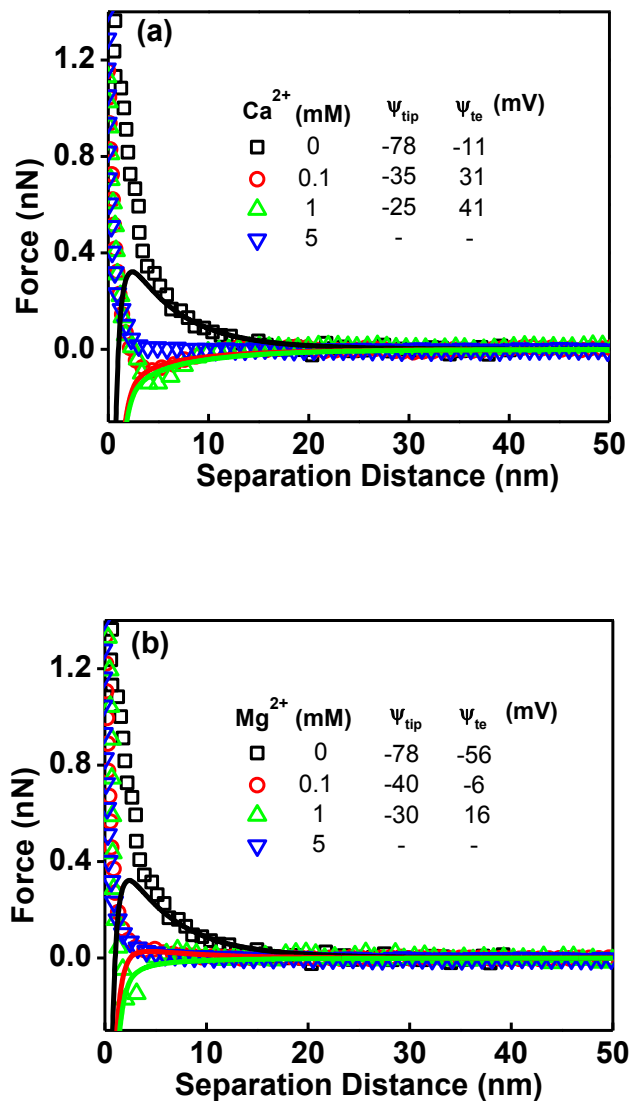


Figure 5.7 Typical AFM interaction force profiles measured between AFM tip and talc edge surfaces in 1 mM KCl solutions of various (a) Ca^{2+} and (b) Mg^{2+} concentrations at pH 8.5. Symbols correspond to experimental data. The solid lines represent theoretical fit of classical DLVO theory. ψ_{tip} and ψ_{te} are the Stern potential values of AFM tip and talc edge surface, respectively.

5.2.4 Stern potentials of different muscovite and talc surfaces

The Stern potential of both basal planes and edge surfaces of muscovite at each Ca^{2+} and Mg^{2+} concentration were determined by fitting the measured force profiles to the classical DLVO theory with appropriate BC (constant surface charge density for the basal plane and constant Stern potential for both the edge surface and tip). As shown in Figure 5.8 (a), without Ca^{2+} addition, both the muscovite basal plane and edge surface are negatively charged at the given pH of 8.5. With the addition of 0.1 mM and 1 mM Ca^{2+} , the Stern potential of the muscovite basal plane increases from around -81 mV to about -35 mV and -18 mV, respectively. The addition of Mg^{2+} shows the similar trend to the effect of Ca^{2+} addition on the Stern potential of the muscovite basal plane. The Stern potential of the muscovite basal plane increases from -81 mV to about -42 mV and -25 mV with the addition of 0.1 mM and 1 mM Mg^{2+} concentration, respectively.

In contrast, the Stern potential of the muscovite edge surface reverses its sign from around -20 mV to a positive value around of 45 mV and 30 mV, with 0.1 mM Ca^{2+} and Mg^{2+} addition, respectively. It continues to increase to around 65 mV and 45 mV with 1 mM Ca^{2+} and Mg^{2+} addition, respectively. De Lint et al. [11] reported a similar reverse of the ζ potential value of alumina from negative to positive values while increasing the concentration of CaCl_2 from 0.15 mM to 1 mM. A further increase in Ca^{2+} concentration from 1 to 10 mM showed only a marginal increase in the ζ potential of alumina.

The Stern potential of different talc surfaces derived by fitting the measured AFM force profiles at each cation concentration to the classical DLVO theory are plotted in Figure 5.8 (b). The magnitude of the Stern potential of the talc basal plane decreases from around -36 mV to -22 mV with 0.1 mM Ca^{2+} addition and

reaches almost zero with 1 mM Ca^{2+} addition. The effect of Mg^{2+} addition on the Stern potential of the talc basal plane shows a similar trend but at different magnitudes as compared to the case of Ca^{2+} additions. The Stern potential of the talc basal increases slightly to around -31 mV and -21 mV at 0.1 mM Mg^{2+} and 1 mM Mg^{2+} addition, respectively.

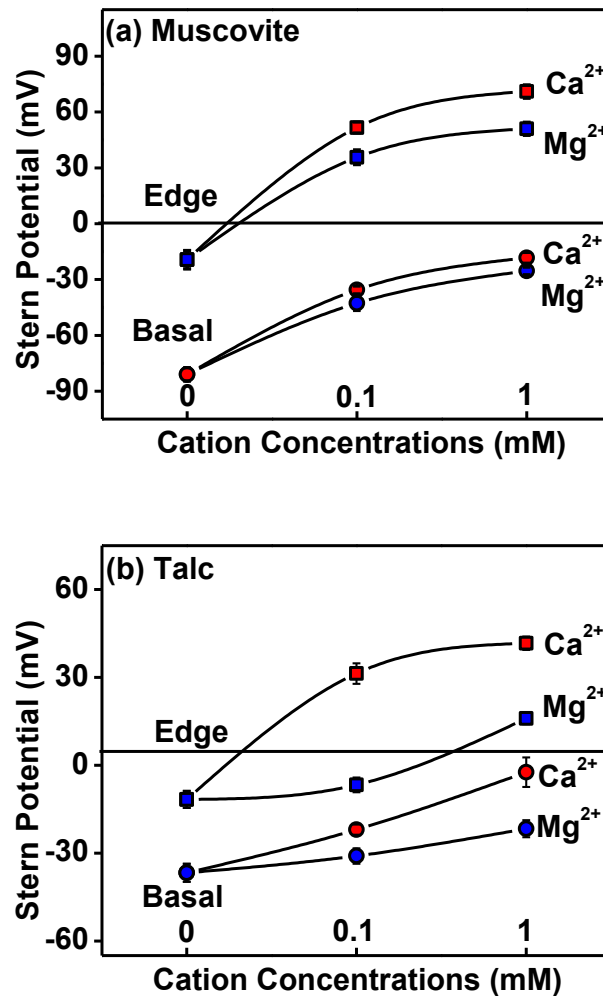


Figure 5.8 Stern potentials of (a) muscovite and (b) talc basal planes and edge surfaces in 1 mM KCl solution of different Ca^{2+} and Mg^{2+} concentrations at pH 8.5, obtained by fitting measured AFM force profiles to the classical DLVO theory.

5.2.5 *Anisotropic surface character of phyllosilicates*

The adsorption of metal ions on the mineral surface in the aqueous solutions usually can be attributed to two different mechanisms: one is the pure electrostatic interaction between positively charged metal ions and the negatively charged or neutral mineral surface; and the other results from surface complexation or specific adsorption of divalent cations at the mineral-water interface.

As mentioned before, the phyllosilicate minerals exhibit different surface charge characteristics on the basal plane and edge surfaces, attributed to different prevailing charge mechanisms. Due to the structural defects, the muscovite basal plane carries fixed negative charges caused by isomorphic substitution of lattice Si^{4+} by Al^{3+} in the T sheets. This permanent negative surface charge characteristic enables the basal plane to attract positively charged metal cations or their hydrolysis products through electrostatic interaction.

On the other hand, charges on the edge surface are attributed to protonation–deprotonation reactions of the hydrolyzed broken primary bonds from the tetrahedral silica-like and the octahedral gibbsite-like sheets. Unlike the inert siloxane group on the basal plane, the amphoteric SOH surface groups (where S represents surface Al or Si atoms) on the muscovite edge surface can easily undergo protonation or deprotonation reactions which impose charge on the edge surface as be expressed in equation (1.1) in Chapter 1. At the given pH of 8.5 in this study, the Si-OH group from the T sheet can be deprotonated to Si-O^- , while the Al-OH surface groups undergo protonation reactions to $\text{Al-OH}_2^{1/2+}$. In addition to these reactions, some of the amphoteric SOH groups on the edge surface are also assumed to be able to form strong bi-or monodentate surface complexes with some metal ions in electrolyte solutions. Generally speaking one of these metal

complexation species is dominant that can be expressed in the following equilibrium reaction [12]:



In the case of the muscovite edge surface, possible surface complexation groups of AlOM^+ can form. These specific bindings of surface groups to the divalent cation in the solution have a more significant effect on the change in the Stern potential of the edge surface as compared to the electrostatic interaction between the muscovite basal plane and divalent cations in the solution. Therefore, the change in the Stern potential of muscovite basal planes and edge surfaces responds differently to the different cations in the solution as shown in Figure 5.8 (a).

Compared to the change in the Stern potential of the muscovite basal plane as shown in Figure 5.8 (a), the difference in surface hydrophobicity and permanent charge density on the talc basal plane may be the reason for the observed difference in the Stern potential variations in responding to the addition of differential divalent cations as shown in Figure 5.8 (b). As a measure of the strength of hydrogen bonding between the surface and water molecules, the hydrophobicity is believed to be affected by the crystal structure of the mineral [13]. The structural charge, cation occupancies and distributions all affect the hydrophobicity of the surface. Similar to the muscovite basal plane, the dominant surface groups on the talc basal plane is the siloxane group which has very low affinity to protons. The charges of the basal plane are mainly caused by the structural defects in the crystalline building sheet. Despite the same charging mechanism, these two phyllosilicate minerals have very different levels of isomorphic substitution. For a perfect muscovite, the ratio of the Al^{3+} substitution for Si^{4+} on the tetrahedral basal plane is close to 1/3 [14], which is responsible for the highly negative Stern potential of its

basal plane. In contrast, the talc basal plane has a much lower isomorphic substitution ratio which results in a lower Stern potential as observed in chapter 4. As a result, these two basal planes show totally different hydrophobicity. The existence of an exclusion zone between siloxane group on talc basal plane and water molecules in solution was well documented. It is due to the absence of polarity of talc basal plane [13, 15]. In contrast, water molecules are tightly bonded with muscovite basal plane of high permanent charge density.

As also shown in Figure 5.8 (b), despite the different chemistry of muscovite and talc edge surface (Al vs Mg), the effect of Ca^{2+} addition on their electrical charge characteristics is quite similar. The Stern potential of both muscovite and talc edge surfaces reverses upon the addition of 0.1 mM Ca^{2+} and increases slightly at 1 mM Ca^{2+} addition. For Mg^{2+} , the muscovite and talc edge surface respond slightly differently. The Stern potential of talc edge surface remains negative with the addition of 0.1 mM Mg^{2+} ions and reverses to positive value only when Mg^{2+} addition is up to 1 mM, while the Stern potential of the muscovite edge surface reverses with the addition of 0.1 mM Ca^{2+} . Instead of Al-OH surface group on muscovite edge surface, the Mg-OH group populates on the talc edge surface. These two surface species exhibit different protonation constants. At a given pH of 8.5, the talc edge surface is more positively charged than the muscovite edge surface as anticipated from a higher PZC value of $\text{Mg}(\text{OH})_2$ than $\text{Al}(\text{OH})_2$ [16]. On the other hand, similar to the case of the muscovite edge surface, in addition to protonation reactions, Mg-OH groups on the talc edge surface are also able to form strong surface complexes with metal ions in solution to form MgOCa^+ and MgOMg^+ . These differences between each surface groups reacting with different metal ions cause different surface charge responses to the presence of different metal ions in solutions.

5.2.6 Effect of different divalent cations

Both Ca^{2+} and Mg^{2+} are hydrolysable metal ions to form corresponding metal hydroxyl species in solutions or at the solid/water interface. At pH 8.5, Ca^{2+} and Mg^{2+} are the predominant species in solution. Different effect of Mg^{2+} and Ca^{2+} on the Stern potential or ζ potential of several minerals is well-documented. For example, Sondi et al. [17] found that at a given pH of 6.5, the ζ potential of montmorillonite and illite was slightly more negative in 0.01 mM to 1 mM Mg^{2+} ion solutions than in Ca^{2+} ion solutions of the same concentration. A similar trend was observed for MnO_2 [18]. To account for the observed effect of Ca^{2+} and Mg^{2+} on ζ potential or Stern potential of metal oxide surfaces, a number of theoretical models based on ion exchange, formation of surface complexes, solvation and specific adsorption, have been proposed. Among these models, the surface complexation model proposed by James and Healy [19] has been widely accepted and used to predict the adsorption properties of ions on different metal oxide surfaces. In their model, the overall free energy change of adsorption (ΔG_{ad_s}) can be considered from three main contributions of the attractive Coulombic force (ΔG_{coul}), the repulsive secondary solvation force (ΔG_{solv}), and the specific "chemical" interaction (ΔG_{chem_i}), given by:

$$\Delta G_{ad_s} = \Delta G_{coul_i} + \Delta G_{solv_i} + \Delta G_{chem_i} \quad (5.2)$$

The Coulombic contribution is given by:

$$\Delta G_{coul_i} = z_i F \Delta \psi_x \quad (5.3)$$

$$\text{where } \Delta \psi_x = \frac{2RT}{zF} \ln \left(\frac{\left(e^{zF\psi_0/2RT} + 1 \right) + \left(e^{zF\psi_0/2RT} - 1 \right) e^{-\kappa x}}{\left(e^{zF\psi_0/2RT} + 1 \right) - \left(e^{zF\psi_0/2RT} - 1 \right) e^{-\kappa x}} \right)$$

$$\psi_0 = 2.3RT / zF(pH_{PZC} - pH) \quad \text{and} \quad x = (r_{ion} + 2r_w)$$

The solvation contribution is given by:

$$\Delta G_{solv} = \left(\frac{z_i^2 e^2 N}{16\pi\epsilon_0} \right) \left(\frac{1}{r_{ion} + 2r_w} - \frac{r_{ion}}{2(r_{ion} + 2r_w)^2} \right) \left(\frac{1}{\epsilon_{int}} - \frac{1}{\epsilon_{bulk}} \right) + \left(\frac{z_i^2 e^2 N}{32\pi\epsilon_0} \right) \left(\frac{1}{r_{ion} + 2r_w} \right) \left(\frac{1}{\epsilon_{solid}} - \frac{1}{\epsilon_{int}} \right) \quad (5.4)$$

$$\text{where } \epsilon_{int} = \left(\frac{\epsilon_{bulk} - 6}{1 + (1.2 \times 10^{-17}) (d\psi/dx)_x^2} \right) + 6 \quad \text{and} \quad \frac{d\psi}{dx} = -2\kappa \frac{RT}{zF} \sinh\left(\frac{zF\Delta\psi_x}{2RT}\right)$$

As we can note from the expression of ΔG_{coul} in equation (5.3), this attractive term is a function of the Debye length κ^{-1} of the solution and the PZC of the mineral surface. On the other hand, the repulsive secondary solvation energy ΔG_{solv} is the energy required to remove the hydration sheath, which is principally determined by the ionic radius and charge of adsorbing ions. The higher the secondary solvation energy, the more difficult the metal cations can absorb on the negatively charged mineral surface. The hydration enthalpies of Mg^{2+} ($-1921 \text{ kJ mol}^{-1}$) is much more negative than that $-1577 \text{ kJ mol}^{-1}$ of Ca^{2+} due to its smaller size and greater polarizing field [20]. Compared with the Ca^{2+} , the more negative hydration enthalpies of Mg^{2+} enables it to interact with water more strongly, holding the water molecules to its hydration shell more tightly. As a result, Ca^{2+} is shown to be more effective than Mg^{2+} to reduce the magnitude of the ζ or Stern potential values of silica, silicon nitride, basal planes of muscovite and talc, and hence to reduce electrostatic interactions as shown in Figures 5.1, 5.3 and 5.8.

In the case of the edge surface, different surface complexes such as $SOCa^+$ and $SOMg^+$ groups (where S represents Si, Al and Mg) can form when Ca^{2+} and Mg^{2+} ions are present in solutions. Since the specific binding of Ca^{2+} and Mg^{2+} ions is responsible for the observed impact of Ca^{2+} and Mg^{2+} addition on their Stern

potentials, the proximity of ions to the surface is more critical. Compared with Mg^{2+} , the less hydrated Ca^{2+} seems easier to get close to the surface and therefore exhibits a stronger effect than Mg^{2+} ions on Stern potential of muscovite and talc edge surfaces.

5.3 Summary

The effect of two divalent cations: Mg^{2+} and Ca^{2+} on the Stern potential of different surfaces of phyllosilicate minerals was investigated by the direct measurement of interaction forces between the AFM tip and various phyllosilicate surfaces using AFM. The measurement was conducted in 1 mM KCl background solutions at pH 8.5 as a function of divalent cation concentration. The Stern potential of each surface was determined by fitting the measured interaction force profiles to the classical DLVO theory using proper BC. Direct colloidal probe force measurement using AFM is proved to be a powerful tool to study the adsorption of cations on well-defined phyllosilicate surfaces (basal planes and edge surfaces). The methodology developed in this study opens the door to probe interactions of various mineral surfaces with process aids under various physicochemical conditions of the system. From this study the following conclusions are drawn.

- 1) The basal plane of talc carries a much lower permanent negative surface charge than the basal plane of mica due to its much lower isomorphous substitution of lattice Si^{4+} by Al^{3+} in the tetrahedron silica sheet, accounting for its hydrophobic nature of the plane.
- 2) The fitted Stern potential of both muscovite and talc basal planes became less negative with the addition of Ca^{2+} or Mg^{2+} ions but did not reverse to a positive value even at Ca^{2+} or Mg^{2+} concentrations up to 5 mM. The reduction in the stern potential is slightly more significant with the Ca^{2+} addition than with Mg^{2+}

addition.

- 3) The Stern potential of the muscovite edge surface reversed at Ca^{2+} or Mg^{2+} concentrations as low as 0.1 mM, and further increased with further increasing their concentrations. The Stern potential of talc edge surface reversed upon the addition of 0.1 mM Ca^{2+} and 1 mM Mg^{2+} , respectively.
- 4) The different responses of the Stern potential of the basal plane and edge surfaces to the divalent cation addition in solution are attributed to the different surface charging mechanisms and binding mechanisms of each type of surfaces with divalent cations: the EDL compression predominate the effect on basal planes and the specific adsorption prevail on the edge surfaces.
- 5) A slightly stronger impact of Ca^{2+} ions than Mg^{2+} ions on Stern potential of both basal planes and edge surfaces is attributed to less hydrated nature of Ca^{2+} ions than Mg^{2+} ions.

5.4 References

- [1] Fong, N., Ng, S., Chung, K. H., Tu, Y., Li, Z., Sparks, B. D., Kotlyar, L. S., 2004, "A Two Level Fractional Factorial Design to Test the Effect of Oil Sands Composition and Process Water Chemistry on Bitumen Recovery from Model Systems," *Canadian Journal of Chemical Engineering*, 82(4) pp. 782-793.
- [2] Ding, X., Repka, C., Xu, Z., Masliyah, J. H., 2006, "Effect of Illite Clay and Divalent Cations on Bitumen Recovery," *Canadian Journal of Chemical Engineering*, 84(6) pp. 643-650.
- [3] Kasongo, T., Zhou, Z., Xu, Z., Masliyah, J. H., 2000, "Effect of Clays and Calcium Ions on Bitumen Extraction from Athabasca Oil Sands using Flotation," *Canadian Journal of Chemical Engineering*, 78(4) pp. 674-681.
- [4] Liu, J., Xu, Z., Masliyah, J. H., 2004, "Role of Fine Clays in Bitumen Extraction from Oil Sands," *AIChE Journal*, 50(8) pp. 1917-1927.
- [5] Zhou, Z., Xu, Z., Masliyah, J. H., 1999, "Coagulation of Bitumen with Fine Silica in Model Systems," *Colloids and Surfaces A-Physicochemical and Engineering Aspects*, 148(3) pp. 199-211.
- [6] Gan, W., Liu, Q., 2008, "Coagulation of Bitumen with Kaolinite in Aqueous Solutions Containing Ca^{2+} , Mg^{2+} and Fe^{3+} : Effect of Citric Acid," *Journal of Colloid and Interface Science*, 324(1-2) pp. 85-91.
- [7] Xu, Z., Liu, J., Choung, J., Zhou, Z., 2003, "Electrokinetic Study of Clay Interactions with Coal in Flotation" *International Journal of Mineral Processing*, 68(1-4) pp. 183-196.
- [8] Zhao, H., Long, J., Masliyah, J. H., Xu, Z., 2006, "Effect of Divalent Cations and Surfactants on Silica-Bitumen Interactions," *Industrial & Engineering Chemistry Research*, 45(22) pp. 7482-7490.
- [9] Ebeling, D., van den Ende, D., Mugele, F., 2011, "Electrostatic Interaction Forces in Aqueous Salt Solutions of Variable Concentration and Valency," *Nanotechnology*, 22(30) pp. 305706.
- [10] Butt, H., 1991, "Measuring Electrostatic, Van der Waals and Hydration Forces in Electrolyte-Solutions with an Atomic Force Microscope," *Biophysical Journal*, 60(6) pp. 1438-1444.

- [11] de Lint, W., Benes, N., Lyklema, J., 2003, "Ion Adsorption Parameters Determined from Zeta Potential and Titration Data for a Gamma-Alumina Nanofiltration Membrane," *Langmuir*, 19(14) pp. 5861-5868.
- [12] Lützenkirchen, J., 2006, "Surface Complexation Modeling," Academic Press, Amsterdam; London.
- [13] Wang, J., Kalinichev, A. G., Kirkpatrick, R. J., 2006, "Effects of Substrate Structure and Composition on the Structure, Dynamics, and Energetics of Water at Mineral Surfaces: A Molecular Dynamics Modeling Study," *Geochimica Et Cosmochimica Acta*, 70(3) pp. 562-582.
- [14] Bergaya, F., Theng, B. K. G., Lagaly, G., 2006, "Handbook of Clay Science," Elsevier, Amsterdam, London.
- [15] Du, H., Miller, J. D., 2007, "A Molecular Dynamics Simulation Study of Water Structure and Adsorption States at Talc Surfaces," *International Journal of Mineral Processing*, 84(1-4) pp. 172-184.
- [16] Parks, G. A., 1965, "The Isoelectric Points of Solid Oxides, Solid Hydroxides, and Aqueous Hydroxo Complex Systems," *Chemical Reviews*, 65(2) pp. 177-198.
- [17] Sondi, I., Bišćan, J., Pravdić, V., 1996, "Electrokinetics of Pure Clay Minerals Revisited," *Journal of Colloid and Interface Science*, 178(2) pp. 514-522.
- [18] Malati, M. A., 1987, "The Role of the Hydration of Cations in their Adsorption on Oxides," *Surface and Coatings Technology*, 30(3) pp. 317-325.
- [19] James, R. O., Healy, T. W., 1972, "Adsorption of Hydrolyzable Metal-Ions at Oxide-Water Interface 3. Thermodynamic Model of Adsorption," *Journal of Colloid and Interface Science*, 40(1) pp. 65-66.
- [20] Smith, D., 1977, "Ionic Hydration Enthalpies," *Journal of Chemical Education*, 54(9) pp. 540-542.

Chapter 6

Understanding suspension rheology of phyllosilicates from direct force measurement using AFM*

As presented in previous chapters, the anisotropic surface charge properties of talc at different pH values were determined by fitting the measured force profiles between the AFM tip and both basal plane and edge surfaces to the DLVO theory. The talc basal planes were found to carry a permanent negative charge, while the charge on its edge surfaces was highly pH-dependent. In this chapter, the interaction energies of various associations between different anisotropic talc surfaces are calculated by using these AFM-derived Stern potential values of talc basal planes and edge surfaces, aiming to better understand how these anisotropic surface charge properties influence the rheology behaviour of aqueous phyllosilicate mineral suspensions.

6.1 Introduction

As well described in Chapter 2, the mismatch of the maximum coagulation of phyllosilicate particle suspensions and their PZC or IEP has been frequently reported. Take talc for an instance, as shown in Figure 6.1 (a), the IEP of talc particles determined using typical instruments for ζ potential measurement was found to be less than pH 3 [1-2]. Therefore, one would expect a gradual decrease in energy barrier with decreasing pH until its IEP as shown in Figure 6.1 (b). As a result, the maximum particle aggregation and hence the highest yield stress would occur at its IEP of pH around 2.3.

*Published work: Yan, L., Masliyah, J. H., Xu, Z., 2013, Current Opinion in Colloid & Interface Science, 18.

However, the maximum yield stress of the talc suspension from rheology studies was reported [3] to be around pH 5.5 as shown in Figure 6.1 (c). Considering the anisotropic surface characteristics of talc, such a mismatch between the IEP and the pH of maximum yield stress is not unexpected. As discussed in Chapter 2, in the case of platy phyllosilicate minerals such as talc or kaolinite, interpretation of colloidal behaviour based on the average ζ potential values determined using the existing electrophoretic measurements or the PZC determined by the potentiometric titration method could be misleading. The apparent discrepancy between the rheology phenomenon and surface charge characteristics in terms of either IEP or PZC is linked to the inability to determine the anisotropic surface properties of phyllosilicate minerals. The basal and edge surfaces of talc, for example, feature different charge characteristics due to their distinct prevailing charge mechanisms. These anisotropic surface charge characteristics of phyllosilicate minerals make their suspensions behave very differently from suspensions of isotropic particles such as silica or alumina. The overall electric surface charges of phyllosilicate mineral particles measured by ζ potential technique or titration method are a combination of electric potential or charges from both basal planes and edge surfaces, which cannot accurately predict the interactions in their suspension systems. As a result, various types of particle interactions are needed to be considered, including edge-to-basal, edge-to-edge and basal-to-basal interactions. These types of interactions dominate association of platy phyllosilicate particles, leading to the formation of a card-house structure. In order to accurately predict rheology behaviour of phyllosilicate mineral suspensions in industrial applications, accurate determination of their anisotropic surface charge properties is essential.

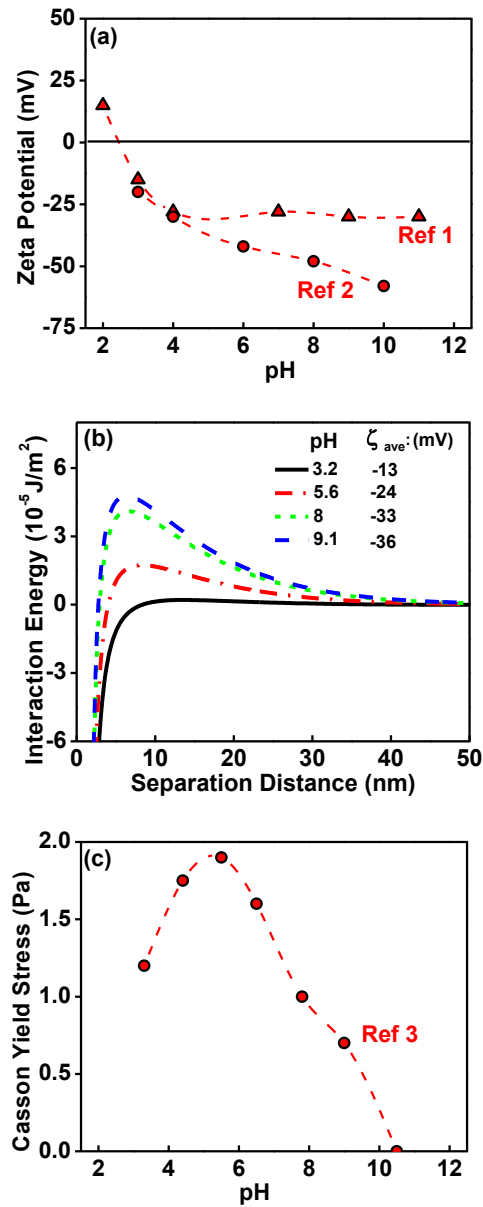


Figure 6.1 (a) Average ζ potential values of talc particles in KCl solutions measured by electrophoresis methods taken from literature [1-2]; (b) the total interaction energy per unit area of talc particles at different pH in 1 mM KCl solutions calculated using DLVO theory and measured average ζ potential values; (c) the yield stress data of talc particles at different pH in KCl solutions taken from literature [3].

6.2 Results and discussion

6.2.1 *Tip calibration*

Colloidal forces between AFM tip and a clean silica wafer were measured in 1 mM KCl solutions of varying pH prior to its use in AFM colloid probe force measurements for characterizing phyllosilicate surfaces. Smooth silica wafers with the R_q less than 0.5 nm over a $4 \mu\text{m}^2$ area were used. Typical force curves of the tip-silica system are shown in Figure 6.2. Since the PZC of silica is well established to be around 2, the silica wafer can be treated as being negatively charged over the pH range (3.2-9) covered in this study. The measured force profiles were analyzed by the classical DLVO theory to quantitatively evaluate the Stern potential of AFM tip. A MATLAB (The Math Works Inc.) program based on its built-in curve fitting function was developed for the fitting process. As shown in Figure 6.2, the experimental tip-silica force profiles are found to be fitted quite well with the theoretical force curves, particularly for separation distances larger than 4-5 nm. The discrepancy at very short separation distances is probably due to the presence of non-DLVO hydration forces between the silica wafer and silicon nitride tip surfaces, which were not taken into account in the classical DLVO theory used in the fitting. As shown in Table 6.1, the fitted stern potential values of silica compare well with values taken from literature [4-6], which validating the applicability of the proposed tip-substrate modeling to study different talc surfaces.

The interaction between a silicon nitride tip and silica wafer on approach is determined to be attractive at pH 3.2 and reversed to repulsive at pH 5.6 and above. Since the silica surface is negatively charged at pH 3.2 and above, the silicon nitride tip must be positively charged at pH 3.2 and negatively charged at pH 5.6 and above. An excellent agreement is shown between the Stern potential

values of silicon nitride tip, obtained in this study by fitting the measured force profiles to the classical DLVO theory, and those taken from literature [7]. It should be noted that the data from literature were also obtained by fitting the measured force profiles to the classical DLVO theory, but the measurement was performed between a silicon nitride tip and silicon nitride substrate. The excellent agreement between the results extracted from the AFM colloid force measurements of two different systems further confirms the robustness of the AFM tip-substrate colloid probe technique to study colloidal forces and surface charge characteristics of solid-aqueous solution interfaces. More importantly, the measured Stern potential of silicon nitride tip allows us to probe Stern potential of various phyllosilicate mineral surfaces using the same technique.

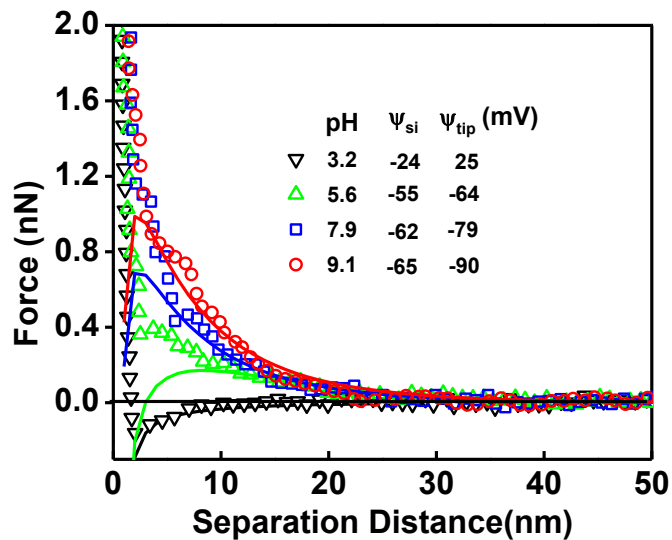


Figure 6.2 Typical interaction force profiles measured between AFM silicon nitride tip and the silica wafer in 1 mM KCl solutions of different pH values. Symbols correspond to the experimental data, while the solid lines represent the fit to the classical DLVO theory. ψ_{si} and ψ_{tip} are the Stern potential values of the silica wafer surface and AFM tip, respectively.

Table 6.1 Comparison of Stern potential, obtained by best-fit of interaction force profiles between a silicon nitride tip and silica wafer measured using AFM colloid probe force technique with the classical DLVO theory, with corresponding literature values obtained by MEP, SP measurement and AFM force curve fitting.

pH	Silica electrical potential (mV)			
	This work	From literature		
		Value	Method	Ref
3.2	-24 ± 5	-25	AFM	[5]
		-22	MEP	[6]
5.6	-55 ± 5	~ -51	AFM	[4]
		-50	MEP	[5]
		-50	SP	
		-60	MEP	[6]
		-25 to -60	AFM	
7.9	-62 ± 5	-56	SP	[4]
		~ -60	MEP	[5]
		-60	MEP/AFM	[6]
9	-65 ± 5	~ -55	AFM	
		-62	MEP	[6]

6.2.2 Interactions between AFM tip and different talc surfaces

Typical force profiles on approaching between AFM silicon nitride tip and talc basal planes (a) and edge surfaces (b) in 1 mM KCl solutions of varying pH values are shown in Figure 6.3. At pH 3.2, attractive interaction was determined between AFM tip and the talc basal plane while the repulsive interaction dominated between AFM tip and the talc edge surface. Since the tip was found to be positively charged at this pH, it can be concluded that the basal plane of the talc is negatively charged while its edge surface is positively charged at pH 3.2.

When the pH of solution increased above 5.6, the interaction between the tip and the talc basal plane is reversed from attractive to repulsive. The repulsion increases steadily with increasing pH of solutions. Similar to the basal plane, the interaction between the tip and the talc edge surface also reverses but in opposite direction from repulsive to attractive, both attributed to the reverse of the surface charge of tip from positive to negative when pH of the solution changed from 3.2 to 5.6, accounting for interactions with negatively charged basal plane and positively charged edge surface of talc. Since the tip remains negatively charged at pH above 5.6, the long range interactions between AFM tip and the talc edge surface again reverses from attractive at pH 5.6, to being almost negligible at pH 7.9 and then repulsive at pH 9, indicating the reverse of surface charge of talc edge surfaces over this pH range. This force profile change is in great contrast to dominant repulsive forces between the tip and talc basal planes over the same pH range.

For quantitative analysis, one can extract the Stern potential values of different talc surfaces at each pH by fitting the measured force profiles to the classical DLVO theory as mentioned earlier. In the fitting process, the Stern potential of AFM tip derived from the tip-silica wafer system was used. As shown in Figure 6.3, the measured force profiles can be well fitted to the classical DLVO theory as indicated by solid curves.

From the fitting of the force profiles to the classical DLVO theory, the Stern potential of both talc basal plane and edge surface as a function of pH is obtained and shown in Figure 6.4. For all pH values tested (3.2, 5.6, 7.9 and 9.0), the fitted Stern potential indicates that the talc basal plane is negatively charged and the pH of solution has a marginal impact on its Stern potential between -23 to -38 mV.

This finding further confirms the charge deficiency on the talc basal plane by isomorphic substitution and suggests a negligible hydrolysis of the siloxane group (-Si-O-Si-) on the talc basal plane over the given pH range tested as anticipated.

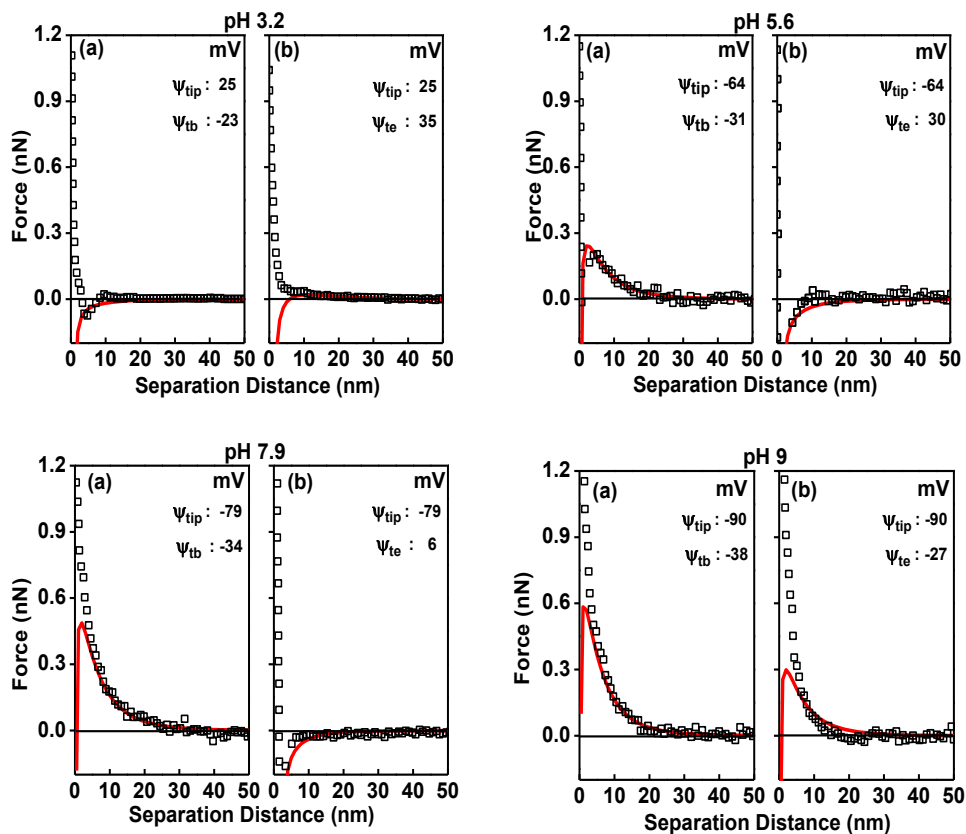


Figure 6.3 Typical force profiles measured between AFM tip and (a) talc basal planes and (b) edge surfaces in 1 mM KCl solutions as a function of aqueous solution pH. Symbols correspond to experimental data, while the solid lines represent theoretical fit of DLVO theory. Ψ_{tb} and Ψ_{te} are the fitted Stern potential values of the talc basal plane and edge surface, respectively.

At pH below 7.9, the talc edge surface is positively charged. The Stern potential at pH 3.2, 5.6 and 7.9 is determined to be 35 mV, 30 mV and 6 mV, respectively. When increasing the pH from 7.9 to 9, the Stern potential reverses to -27 mV. These

results suggested that the surface charge of talc edge surface is strongly pH-dependent. The PZC of the talc edge surface is estimated to be around pH 8. Unlike the charges on the basal plane caused by isomorphous substitution of structural ions, the charge on the edge surface is attributed to the hydrolysis of broken primary SiO- bonds from tetrahedral silica-like sheets and MgO- bonds from octahedral brucite-like sheets. Unlike the siloxane group on the basal plane, the amphoteric SiOH (PZC=1.9) [8] and MgOH (PZC=12) [9] surface groups on the talc edge surface can more easily undergo protonation or deprotonation reactions which leads to the pH-dependent surface charge on talc edge surfaces.

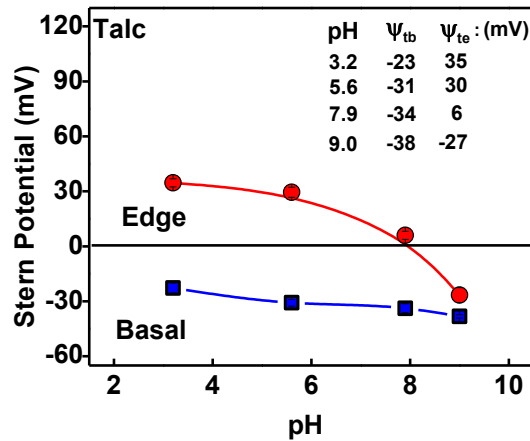


Figure 6.4 Stern potentials of different talc surfaces in 1 mM KCl solutions of different pH values extracted by fitting the measured force profiles to the classical DLVO theory shown in Figure 6.3.

6.2.3 Interaction energy between different talc surfaces

After determining the Stern potential of various types of talc particle surfaces, interactions between these surfaces were calculated using DLVO theory. The VDW interaction energies between two planar surfaces were calculated using equation (2.2-2.3). The EDL interaction energy between two planar surfaces was calculated by equations (3.3-3.5) at different BC in previous chapters.

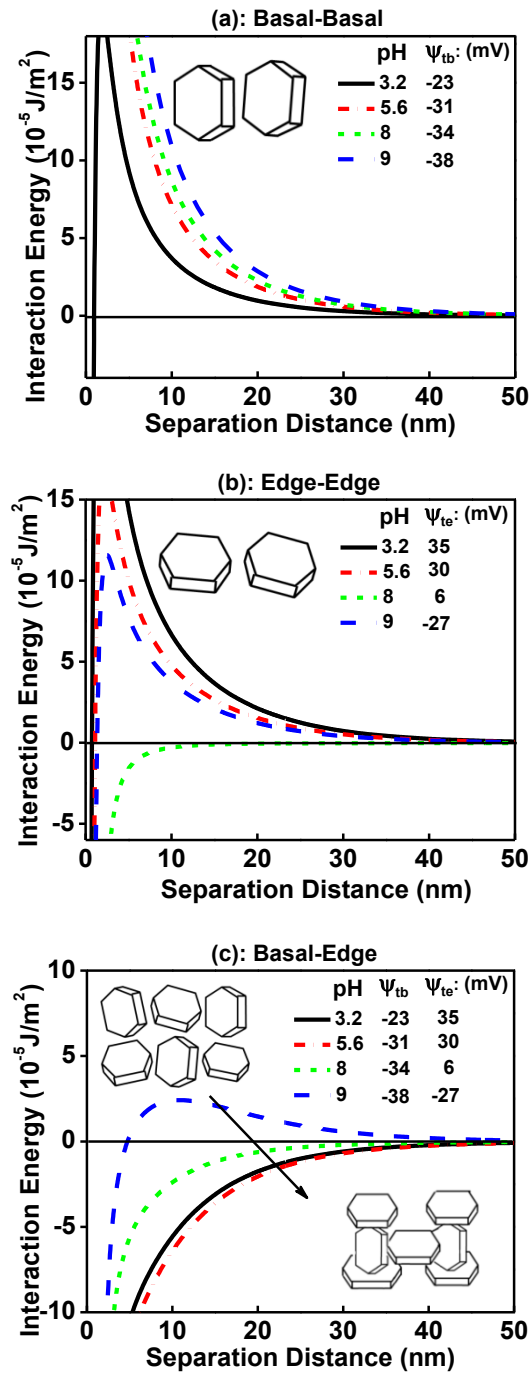


Figure 6.5 The calculated total interaction energy per unit area of various associations of talc surfaces in 1 mM KCl solutions at different pH using the Stern potential values derived from AFM colloid probe force measurement and DLVO fit.

In talc suspensions system, three types of particle associations may occur: basal–basal, edge–edge and basal–edge. Using the Stern potential values in Figure 6.4 of talc basal planes and edge surfaces, derived from the fitting of the measured force profiles to the classical DLVO theory, the interaction energy of each kind of association calculated at different pH values is shown in Figure 6.5.

As it is revealed in Figure 6.4 that the talc basal plane carried permanent negative surface charge and insensitive to the change of solution pH, the electrostatic interaction energy between basal planes was calculated by using equation (3.3) for constant surface charge density case. As shown in Figure 6.5 (a), the basal-basal interactions are all repulsive over the pH range studied. Compare to the van der Waals attraction, the electrostatic repulsion was much stronger and dominant in the total interaction energy between the two basal planes. The energy barrier is observed to be significantly high. By lowering the solution pH to 3.2, only a slight decrease in the energy barrier is observed due to its pH-insensitive nature of the Stern potential.

In contrast to the fixed negative surface charge of talc basal planes caused by isomorphic substitution, the charge of talc edge surface was highly pH-dependent, which is negative at pH 9 and reverses to positive value at pH less than 8. Such charge characteristics led to interesting interaction energy profiles of Figure 6.5 (b) using the electrostatic interaction energy between edges was calculated using the equation (3.4) for the constant electric surface potential case. At lower pH 3.2 and 5.6, the edge surfaces are highly repulsive although the energy barrier is lower at pH 5.6 than at pH 3.2. At pH 8, the force profile shows a negligible energy barrier due to a negligible surface charge of talc edge surface at this pH. In this case the VDW attraction dominates the total interaction between the two edge surfaces.

With the pH of the solution being increased to 9, the EDL repulsion becomes more dominant than VDW forces, leading again to a noticeable energy barrier due to charge reverse to a Stern potential of -27 mV.

In the case of association between talc edge surfaces and basal planes in Figure 6.5 (c), the EDL interaction energy between the basal plane and the edge surface was calculated using the equation (3.5) for the mixed case and a strong repulsion was obtained at pH 9. At this pH both the talc basal plane and edge surface are negatively charged. These similarly charged surfaces repelled each other, leading to a strong repulsive energy barrier as shown in Figure 6.5 (c). At pH 8, talc basal plane remains negatively charged while its edge surface becomes already slightly positively charged. Due to the opposite sign of surface charges of the basal plane and edge surface, the electrostatic interaction is reversed from repulsive to attractive. As a result, the talc basal planes and edge surfaces are monotonically attractive, leading to the formation of three dimensional card-house structure as shown schematically in the inset of Figure 6.5 (c). This attraction becomes even stronger as the positive charges of the edge surface increases with decreasing pH, and reaches the maximum at pH 5.6 where the difference in Stern potentials between the two surfaces is at its maximum (61 mV). With a further decrease in pH to 3.2, the EDL attraction becomes slightly weaker due to a slightly smaller Stern potential difference as compared with the value at pH 5.6.

6.2.4 Predicting rheology of talc suspensions

Instead of using interaction energies calculated from average ζ potential values shown in Figure 6.1, the rheology or yield stress of talc suspensions can be better explained using the interaction energy profiles calculated from Stern potential values of each kind of surfaces for their association (basal-basal, edge-edge,

basal-edge) at different pH values as shown in Figure 6.5. At pH higher than 9, the double-layer repulsion governs the interactions of all three associations between talc basal planes, edge surfaces or basal plane and edge surfaces, leading to a well dispersed talc suspension and hence low yield stress of suspensions, as shown in Figure 6.1 (c). When the charge of talc edge surface reversed from negative to positive with decreasing the pH of the solution to 8, the interaction between talc basal plane and edge surfaces becomes attractive while there is little repulsion between edge-edge surfaces. Such an interaction system would lead to formation of three dimensional card house structures from basal-edge association with limited edge-edge alignment and without stack of basal planes due to strong repulsion between the basal planes. As a result, an increase in yield stress is anticipated as shown in Figure 6.1 (c). A further decrease in pH to 5.6 led to the strongest attraction between the edge surfaces and basal planes, while the forces between edge-edge and basal plane-basal plane are strongly repulsive. Such a system would lead to the highest probability of card-house formation due to the strongest attraction between the basal and edge planes and hence the highest yield stress as observed. A further decrease in suspension pH to 3.2 led to a slight decrease in attraction between talc edge surface and basal planes while the association between talc edges shows a strong repulsive energy barrier. At the same time, the energy barrier between talc basal planes is also decreased. In this case, a slightly weaker association between talc basal planes and edges are anticipated while there some weak basal plane stacking, leading to weaker card-house structure and hence slightly lower yield stress than at pH 5.6, as shown in Figure 6.1 (c). It appears that the attractive interaction between talc basal planes and edge surfaces dominates rheological properties of talc suspensions. To reduce the yield stress and hence improve the flow of talc suspensions, it is of paramount

importance to adjust systems in such a way that minimizes attraction between basal planes and edge surface by increasing pH or more preferably adding dispersants which interact specifically with edge surfaces.

Similar rheological characteristics of the montmorillonite and bentonite suspension were reported [10-11]. Although various hypotheses has been proposed to account for the observed discrepancy between the measured rheology and that predicted based on the average ζ potential or surface charge density of phyllosilicate minerals, extension of our study to these systems would lead to definitive mechanism that controlling the rheology of suspensions consisting of anisotropically-charged solids.

6.3 Summary

Following successful preparation of sufficiently smooth talc edge surfaces by the ultramicrotome method for AFM colloid probe force measurement, anisotropic surface charge properties of talc at different pH values were determined by fitting the measured force profiles between the AFM tip and both talc basal plane and edge surfaces to the classical DLVO theory. The talc basal planes were found to carry a permanent negative charge, while the charge on its edge surfaces was highly pH-dependent, negative at pH 9 and positive at pH less than 8.

The Stern potential values of talc basal planes and edge surfaces obtained from fitting of the measured force profiles allowed us to calculate the interaction energy for association between anisotropically-charged phyllosilicate surfaces, such as basal plane-basal plane, edge-edge and basal plane-edge. The results confirmed the attractive interaction between talc basal planes and edge surfaces dominates the rheological behaviour.

The highest probability of card-house formation between talc edge surfaces and basal planes was determined at pH 5.6, which corresponds well with the measured highest yield stress of talc suspensions.

Our study clearly demonstrates the necessity of determining anisotropic surface charge characteristics if one would want to improve their understanding of rheological properties and hence better control their process performance.

6.4 References

- [1] Morris, G., Fornasiero, D., Ralston, J., 2002, "Polymer Depressants at the Talc-Water Interface: Adsorption Isotherm, Microflotation and Electrokinetic Studies," *International Journal of Mineral Processing*, 67(1-4) pp. 211-227.
- [2] Burdukova, E., Becker, M., Bradshaw, D. J., 2007, "Presence of Negative Charge on the Basal Planes of New York Talc," *Journal of Colloid and Interface Science*, 315(1) pp. 337-342.
- [3] Wang, J., Somasundaran, P., 2005, "Adsorption and Conformation of Carboxymethyl Cellulose at Solid-Liquid Interfaces using Spectroscopic, AFM and Allied Techniques," *Journal of Colloid and Interface Science*, 291(1) pp. 75-83.
- [4] Zhao, H., Bhattacharjee, S., Chow, R., Wallace, D., Masliyah, J. H., Xu, Z. 2008, "Probing Surface Charge Potentials of Clay Basal Planes and Edges by Direct Force Measurements," *Langmuir*, 24(22) pp. 12899-12910.
- [5] Liu, J., Xu, Z., Masliyah, J. H., 2003, "Studies on Bitumen–Silica Interaction in Aqueous Solutions by Atomic Force Microscopy," *Langmuir*, 19(9) pp. 3911-3920.
- [6] Hartley, P. G., Larson, I., Scales, P. J., 1997, "Electrokinetic and Direct Force Measurements between Silica and Mica Surfaces in Dilute Electrolyte Solutions," *Langmuir*, 13(8) pp. 2207-2214.
- [7] Yin, X., Drelich, J., 2008, "Surface Charge Microscopy: Novel Technique for Mapping Charge-Mosaic Surfaces in Electrolyte Solutions," *Langmuir*, 24(15) pp. 8013-8020.
- [8] Avena, M. J., Mariscal, M. M., De Pauli, C. P., 2003, "Proton Binding at Clay Surfaces in Water," *Applied Clay Science*, 24(1-2) pp. 3-9.
- [9] Pokrovsky, O. S., Schott, J., 2004, "Experimental Study of Brucite Dissolution and Precipitation in Aqueous Solutions: Surface Speciation and Chemical Affinity Control," *Geochimica Et Cosmochimica Acta*, 68(1) pp. 31-45.
- [10] Brandenburg, U., Lagaly, G., 1988, "Rheological Properties of Sodium Montmorillonite Dispersions." *Applied Clay Science*, 3(3) pp. 263-279.
- [11] Benna, M., Kbir-Ariguib, N., Magnin, A., 1999, "Effect of pH on Rheological Properties of Purified Sodium Bentonite Suspensions," *Journal of Colloid and Interface Science*, 218(2) pp. 442-455.

Chapter 7

Adsorption and conformation of polysaccharide on anisotropic phyllosilicates:

Effect of ionic strength

Following the investigation of surface charging characteristic of different phyllosilicate in various solutions, some preliminary results of polymer adsorption on different talc surfaces are presented in this chapter. The adsorption of carboxymethyl cellulose (CMC) on distinct talc basal plane and edge surfaces in solutions of various ionic strengths is investigated by in situ AFM imaging technique, aiming to provide some fundamental insights on the mechanisms of polysaccharide adsorption on anisotropic phyllosilicate surfaces.

7.1 Introduction

Utilization of polymers as process aids in mineral processing is well documented. By interacting with mineral particles and altering the interactions between mineral particles and air bubbles, polymers can play various roles, such as acting as flocculent, dispersant or depressant in industrial processes such as selective flotation, desliming, or dewatering.

Commercial synthetic polymers such as polyacrylamide (PAM) have been routinely selected as process aids in mineral processing. However, most PAM based polymers are extremely toxic and environmentally unacceptable. Therefore, as a promising substitute, natural organic polysaccharides such as cellulose or starch are often considered due to their non-toxic and biodegradable nature. In fact, they are widely used as depressants for iron sulphide and talc which are

inherently hydrophobic minerals or other rock forming gangue minerals [1-3]. The adsorption of polysaccharides at mineral surfaces is dependent on both the solution condition (such as the ionic strength and/or pH of the solution) and the surface property of the mineral (such as the hydrophobicity or chemical nature). Among these variables, the ionic strength of the solution was reported to be a crucial factor on adsorption of some polysaccharides on various mineral surfaces such as illite, dolomite and talc [4-6], leading to totally different stability behaviour of mineral suspensions.

Polymer adsorption on minerals has been extensively investigated using both the molecular modeling and experimental measurements. In the view of the experimental studies, infrared spectroscopy (IR) studies are widely used to investigate the interactions between the functional groups of polymers and mineral surfaces [7-9]. The shortcoming of IR method is that the IR results reported so far are based on dried samples, which are drastically different from most real scenarios of polymer adsorption on the mineral surface occurring and corresponding functions in the aqueous solutions. The state of polymers could be substantially alternated during the dehydration process. Electrophoresis measurement is another conventional experimental method being used to study polymer adsorption on mineral surfaces [4, 10-12]. The electrophoretic mobility of suspensions in solution was measured, which is then converted to ζ potential values of the particles. However, the equations used for the conversion are derived for spherical or near-spherical particles with the assumption that the charges of particles are uniformly distributed on the mineral surfaces. No single model is well developed to properly describe the movement of anisotropic particles under a given electric field. The total electric surface charge of

phyllosilicate particles determined by the ζ potential measurement method is just a combined effect of charges from both the basal planes and edge surfaces which can vary with the basal/edge area ratio of particles. Therefore, in the case of anisotropic phyllosilicate suspensions, the interpretation of colloidal behaviour based on ζ potential values determined by the existing electrophoretic methods could be misleading.

AFM has been widely used to study the adsorption of polysaccharides on both hydrophobic (such as talc, molybdenite and graphite) and hydrophilic mineral (such as chalcopyrite, clinocllore or sphalerite) surfaces [13-14]. By analyzing the images of the adsorbed polymer layers on mineral surfaces, AFM provides the possibility to directly investigate the conformation or morphological change of adsorbed polymer on mineral surfaces in different environments. Especially, by employing the in situ AFM imaging, the response of the adsorbed polymer to the change of the solution condition (alteration of polymer or electrolyte concentration) can be monitored. Based on AFM images, for example, Kaggwa et al. [15] found that the roughness of the surface, the substituted functional group and molecular weight of the polymer all play a role in affecting the morphology of adsorbed polymer on treated silica surfaces. Beattie's group studied systematically the adsorption of different polysaccharides with various functional groups, degree of substitution and molecular weight on both hydrophobic and hydrophilic minerals [6, 13-14, 16-19]. They found that not only the functional group on the polymer chain or the molecular weight of the polymer can affect the conformation and morphology of the adsorbed polymer layer on the mineral surfaces; different morphologies of the adsorbed polymer layer were also evolved on surfaces of similar hydrophobicity and surface roughness.

More importantly, the morphological features such as the surface coverage or thickness of polymer layer on the mineral surface shown in AFM images were proven to be closely related to the depressant efficiency of the polymer in mineral processing. Based on this relation, the information obtained from the AFM image at different conditions is considered as a key parameter to predict the polymer performance on certain minerals in industrial mineral processing.

In spite of a large number of studies, the adsorption mechanism of the polysaccharides on anisotropic mineral surfaces remains a subject for debate. Taking the typical magnesium phyllosilicate talc as an example, many adsorption mechanisms have been proposed based on both experimental or simulation results, to govern the adsorption process of the polysaccharide on the talc surface. Based on the variable adsorption of CMC on the talc samples of different hydrophobicities, Steenberg [20] proposed hydrophobic interaction between the CMC and talc particle being the main mechanism of CMC adsorption on talc surface. In contrast, Wang et al. [7] observed by employing the fluorescence spectroscopy that the hydrophilic instead of hydrophobic domains were formed on the interface between the labeled CMC and the talc surface in aqueous solutions. Adding the hydrogen bond breaker (urea) to the solution led to a significant reduction in the adsorption of CMC on talc surface. The strong hydrogen bonding of CMC on talc was confirmed by their FTIR study. Furthermore, they found the adsorption of CMC on talc surface being affected by the changes of the pH and ionic strength of the solution. Based on these experimental results, combined with their molecular modeling, they suggested that the main driving force for CMC adsorption on the talc surface is a combination of hydrogen bonding and electrostatic interaction rather than hydrophobic interaction.

To mediate this contradiction, Liu et al. [3] proposed an acid-base interaction model to include both hydrogen bond interaction and hydrophobic interaction for the natural polysaccharides adsorption on mineral surfaces in solutions. In their model, the hydrogen bond was treated as the typical acid-base bond. The primary interaction caused by the polysaccharide acting as Brønsted acids and the metal-hydroxyl species on the mineral surface as Brønsted bases. The hydrophobic interaction was also treated as a form of acid-base interactions since it was caused by the Lewis acid-base free energy of cohesion between water molecules in aqueous solutions. However, this interaction alone may not be the primary factor and only contribute to a synergistic effect for polysaccharide adsorption on the mineral surface.

More recently, Laskowski et al. [2] considered the anisotropic nature of the talc surface which exhibits different surface characteristics on their basal planes and edge surfaces. They observed that reducing the face-to-edge ratio of talc particles by reducing particle size decreased the polysaccharides adsorption on talc particles and concluded that the adsorption of polysaccharide takes place mostly on face surfaces of talc particles instead of edge surfaces. However, Morris et al. [12] proposed that CMC can adsorb on both the face and edge surfaces of talc particles through different mechanisms: hydrophobic interaction with basal planes hindered by weak repulsive electrostatic interaction with talc edge surfaces. Cuba-Chinem et al. [9] also suggested two different adsorption mechanisms of CMC on anisotropic talc surfaces. In situ ATR-FITR spectroscopy and the adsorption kinetic data of talc particles, revealed a stronger interaction of CMC with the talc edge through chemical complexation and a weaker hydrophobic interaction with the basal plane. By employing the molecular dynamics simulation, Du and Miller [21] proposed that polysaccharide molecules can be attracted and

stabilized at the talc basal plane with strong affinity while do not adsorb on the talc edge surface due to strong interaction between talc edge surfaces and surrounding water molecules.

Despite great efforts to elucidate how polymers adsorb on phyllosilicates, how the specific surface of talc interacts with polymers remains unresolved, due to the lack of direct experimental technique to probe the adsorption of polymers on their basal planes or edge surfaces. Up to date, most experiments were still limited to basal planes or simply rough surfaces due to the difficulties in preparing sufficiently smooth phyllosilicate edge surfaces. Simulation results on the edge surface are hard to be confirmed by experimental results.

In this chapter, the influence of ionic strength of KCl solutions on polysaccharide adsorption on anisotropic phyllosilicate surfaces is investigated by in situ AFM imaging, aiming to provide some fundamental insights on adsorption mechanisms for specific surfaces.

7.2 Experimental

7.2.1 Polysaccharide solution

CMC sodium salt (MW 70 kD, DS 0.7) supplied by Aldrich Inc. was used in this study. A stock solution of 2500 mg L⁻¹ was prepared by dissolving the polymer powders in background electrolyte (KCl) solutions overnight to ensure complete hydration of the polymer. The ζ potential value of CMC was determined by Nano-ZS Zetasizer (Malvern Instruments Ltd., Worcestershire, UK) and the radius of gyration of CMC was determined by dynamic light scattering (DLS) using an ALV 5022 laser light-scattering instrument equipped with a cylindrical He-Ne laser at a scattering angle of 90°. The DLS experiments were completed in

10 minutes and repeated at least twice. The CONTIN program supplied with the correlator was used to calculate the radius of gyration.

7.2.2 *AFM imaging*

The Peak Force Tapping imaging technique provided in quantitative nanomechanical mapping mode of AFM (Veeco Instruments Inc., Santa Barbara, CA, USA) is used for taking images. In this new model, the tip-sample interaction forces instead of cantilever amplitude in common tapping was monitored and controlled, which makes the operation inherently more stable in both air and liquid. Therefore, the quality of obtained images is greatly improved compared to the normal tapping mode.

Freshly prepared surface was first placed in a liquid cell. After injecting the CMC solution into the cell, the surface was incubated for 30 minutes, after which the polymer solution was exchanged by injecting the KCl solution of same ionic strength using a syringe. The image was taken after injecting the KCl solution for at least 30 minutes to make sure the whole system has reached the equilibrium. To avoid potential artifact on the image due to adsorbed polymer on the tip, the image was also taken in the same background KCl solution on another surface. This surface was incubated with a small droplet of CMC solution for 30 minutes and gently rinsed by KCl solution before being placed in the liquid cell for imaging. Very similar surface features were observed for the two surfaces treated by different protocols. No degradation in the quality of the image was shown by soaking the tip in the liquid cell filled with the CMC solution for 30 minutes, indicating CMC does not adsorption on AFM tip at pH 9. It was noticed that when changing CMC solutions of higher KCl ionic strength, some of the adsorbed CMC remained on the mineral surface even after flushing by a large amount of

corresponding supporting KCl solutions at pH 9, indicating that the adsorption of CMC process is not reversible in solutions of high electrolyte concentrations at least to some extent. In order to exclude the effect of adsorption history and have better comparison, at each ionic strength of the KCl solution, a new surface was prepared and used for imaging. At least three fresh surfaces were used for each ionic strength of the KCl solution and multiple images were obtained at various locations on each surface to ensure the reproducibility of imaging. All experiments were conducted at room temperature ($20 \pm 2^\circ\text{C}$).

The R_q surface roughness and the peak-to-valley (PTV) distance for the imaged surface were analyzed by Nanoscope Analysis software (Bruker, Santa Barbara, CA, USA) after the second-ordered flattening of the raw image profiles. In this study, the PTV distance was defined as the apparent layer thickness of adsorbed CMC layer on each surface. The polymer coverage on each surface was calculated by using Image J software [22]. An example of image processing is shown in Figure 7.1.

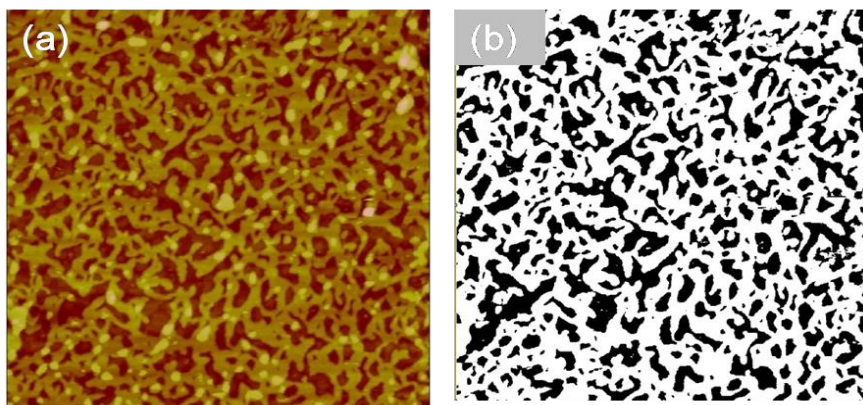


Figure 7.1 Image processing for determination of CMC coverage on the surface by using Image J: (a) the original AFM image of CMC (50 ppm) adsorbed onto the talc basal plane in 100 mM KCl solutions at pH 9, and (b) the corresponding B/W (black and white) image for calculation.

After visually adjusting the threshold to differentiate the CMC features and background mineral, the original AFM image was converted to a black and white (B/W) image. The surface coverage was calculated based on this B/W image by determining the number of black pixels over the total number of pixels shown.

7.3 Results and discussion

7.3.1 Characteristics of CMC

Among natural polysaccharides, cellulose is one of the most abundant and important kind with simple monosaccharide (sugar) units. To better understand how the change in polymer conformation affects the morphology of the polymers on the mineral surface in KCl solutions of different ionic strengths, the representative two dimensional liner cellulose CMC was chosen in this study. The monomeric structure of CMC is shown in Figure 7.2.

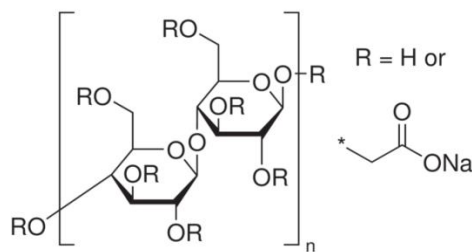


Figure 7.2 The structure of CMC

Due to the ionization of substituted carboxyl groups ($-\text{COO}^-$) on the polymer chain, CMC carries negative charge when the pH of the solution is above its intrinsic dissociation constant (pK), which was reported to be less than pH 4 [23]. The electrostatic repulsion between the charged carboxyl groups can stretch the polymer chain in solutions by keeping the polymer chains away from each other. The electrostatic repulsion between the charged carboxyl groups can be reduced by increasing the ionic strength, as a result of the screening of charges on the

polymer. Theoretically, the thickness of the EDL of the simple electrolyte (KCl) solutions can be reduced from 9.61 nm in 1 mM concentration to 3.04 nm in 10 mM and 0.96 nm in 100 mM solutions. Such significant screening results in a lower ζ potential of CMC with increasing the ionic strength of the solution. To verify this reduction, ζ potentials of CMC in KCl solutions of three ionic strengths (1 mM, 10 mM and 100 mM) at pH 9 was determined and the results are shown in Figure 7.3 (a). The zeta potential value of CMC changes from about -35 mV in 1 mM KCl solution to -25 mV in 10 mM KCl and further to -12 mV in 100 mM KCl solution. Consequently, this reduction in ζ potential due to compression of the EDL would significantly affect the conformation of CMC in the solution. This is reflected by the change in the radius of gyration of CMC as shown in Figure 7.3 (b). At low ionic strength of 1 mM KCl solution, the radius of gyration of CMC is around 60 nm, indicating a much extended CMC macromolecule due to strong electrostatic repulsion between the charged carboxylic groups on polymer chains. As the EDL of electrolyte is compressed by increasing the ionic strength of the solution, this repulsion is minimized. Therefore, the CMC macromolecules can overcome the intramolecular repulsion to form a more densely packed polymer coil. This coiling effect is clearly observed by a significant reduction in the radius of gyration of CMC from 60 nm in 1 mM KCl to 35 nm in 10 mM KCl solution, and further to 10 nm in 100 mM KCl solution as shown in Figure 7.3 (b).

This charge characteristics of CMC macromolecules at the alkaline condition and corresponding coiling in higher electrolyte concentration solutions helps to explain why higher polymer adsorption density on mineral surfaces was observed in more concentrated brines, as reported in literature [4, 24].

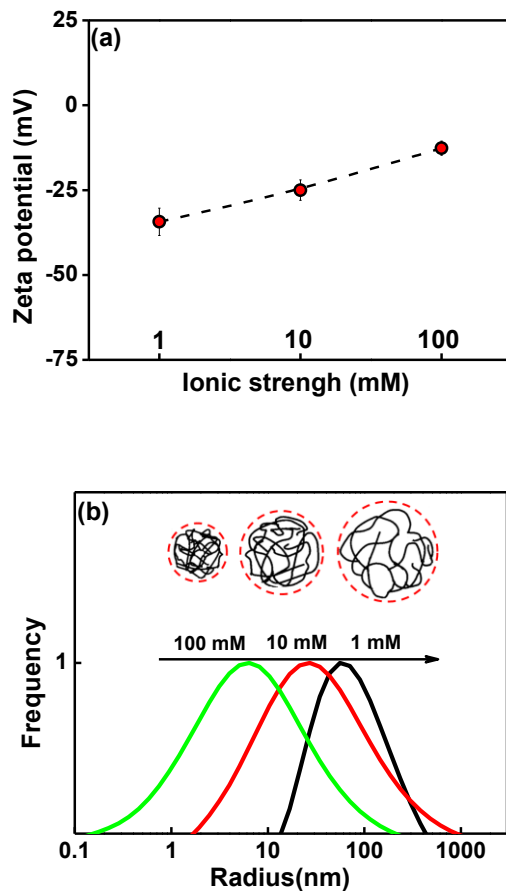


Figure 7.3 (a) ζ potentials and (b) the corresponding radius of gyration of CMC in KCl solutions of different ionic strengths at pH 9.

7.3.2 CMC adsorption on talc basal planes

In situ AFM images of CMC on the talc basal plane in KCl solutions of different ionic strengths are shown in Figure 7.4. The corresponding R_q roughness, the apparent layer thickness and surface coverage of the adsorbed CMC are given in Table 7.1. CMC forms the chain-like network on the talc basal plane in KCl solutions of all three ionic strengths studied. The R_q roughness of the bare talc basal plane was found in previous Chapter 4 to be around 0.24 nm over 4 μm^2 area. As shown in Figure 7.4 (a), due to the adsorption of CMC with an average thickness around 4 nm, the R_q roughness of the talc basal plane increased to 1.73 nm over 4 μm^2 area. The morphology of the evolved CMC layer and its surface

coverage at the talc basal plane in the higher KCl solution (10 mM) as shown in Figure 7.4 (b) are similar to the case in the 1 mM KCl solution. The surface roughness of the talc basal plane was increased to 3.31 nm over $4 \mu\text{m}^2$ area due to the formation of CMC agglomerate lumps of an average thickness around 5 nm. Similar thickness value of the adsorbed CMC layer was found in the 100 mM KCl polymer solution. As shown in Figure 7.4 (c), although the average thickness of the adsorbed CMC layer remains almost the same, the surface roughness was decreased to 2.19 nm over $4 \mu\text{m}^2$ area. Overall, increasing the ionic strength of the supporting electrolyte increased the polymer coverage on the basal plane significantly from 54.1% to 72.5%, while making the CMC network domains on the basal plane more compact.

Talc is an inherently hydrophobic mineral with a perfect cleavage along its basal planes. The basal plane of talc is of very low surface energy due to their non-polar siloxane group ($-\text{Si}-\text{O}-\text{Si}-$) on the surface. When the CMC macromolecule in the solution starts to make contact with this hydrophobic surface, the CMC macromolecule with its surrounding hydration water may behave like a nano liquid droplet, and tries to minimize its contact with this low energy surface to decrease the entropy of the system. Meanwhile, the talc basal plane would prevent this droplet spreading over the surface due to its inherent hydrophobicity. On the other hand, CMC may have some degree of hydrophobic attraction to the talc basal plane via their hydrocarbon backbone and methyl groups on the polymer chains, which can force the CMC macromolecule to attach to the talc basal plane. Similar branch-like feature was found on the carboxymethyl substituted dextrin [19] or hydroxypropylated starch [25] adsorbed on the talc basal plane. The dextrin without any substitution functional group showed only small spherical domains on the same surface. Strong affinity between polysaccharides and the talc

basal plane was shown by the molecular dynamics simulation [21]. In the simulation, the model dextrin molecule was found to attract to and stabilize on the hydrophobic talc basal plane. Due to the absence of surface metallic sites and hydrogen bonding sites on the talc basal plane, the most possible explanation for this strong attraction is via hydrophobic attraction between the hydrophobic moieties of the polymer and the talc basal plane.

As mentioned above, the conformation of CMC in KCl solutions becomes more coiled in higher KCl concentration solutions due to the reduction in both intramolecular and intermolecular repulsion between the polymer chains. The morphological change of the adsorbed CMC layer on the talc basal plane in response to the increase in the ionic strength of the KCl solution can also be attributed to the reduced repulsion between CMC molecules and talc basal planes.

As observed in our previous chapters, the talc basal plane carries negative charge in KCl solutions at pH 9 due to the isomorphic substitution. Therefore, similar to reduced repulsion between CMC polymer chains, the compressed EDL in the solution also reduces electrostatic repulsion between the talc basal plane and CMC. This in turn causes the conformational rearrangement of CMC macromolecules on the talc basal plane.

The alteration of the hydrophobicity of the talc basal plane by adsorption of CMC at different KCl ionic strengths was investigated by the contact angle measurements using sessile drop method and an advanced imaging system (Model 250 Std G/T, Rame-hart instrument co., US). The comparison of the contact angle of bare talc basal planes and treated by CMC solution (50 ppm) in different KCl concentrations at pH 9 is given in Table 7.2.

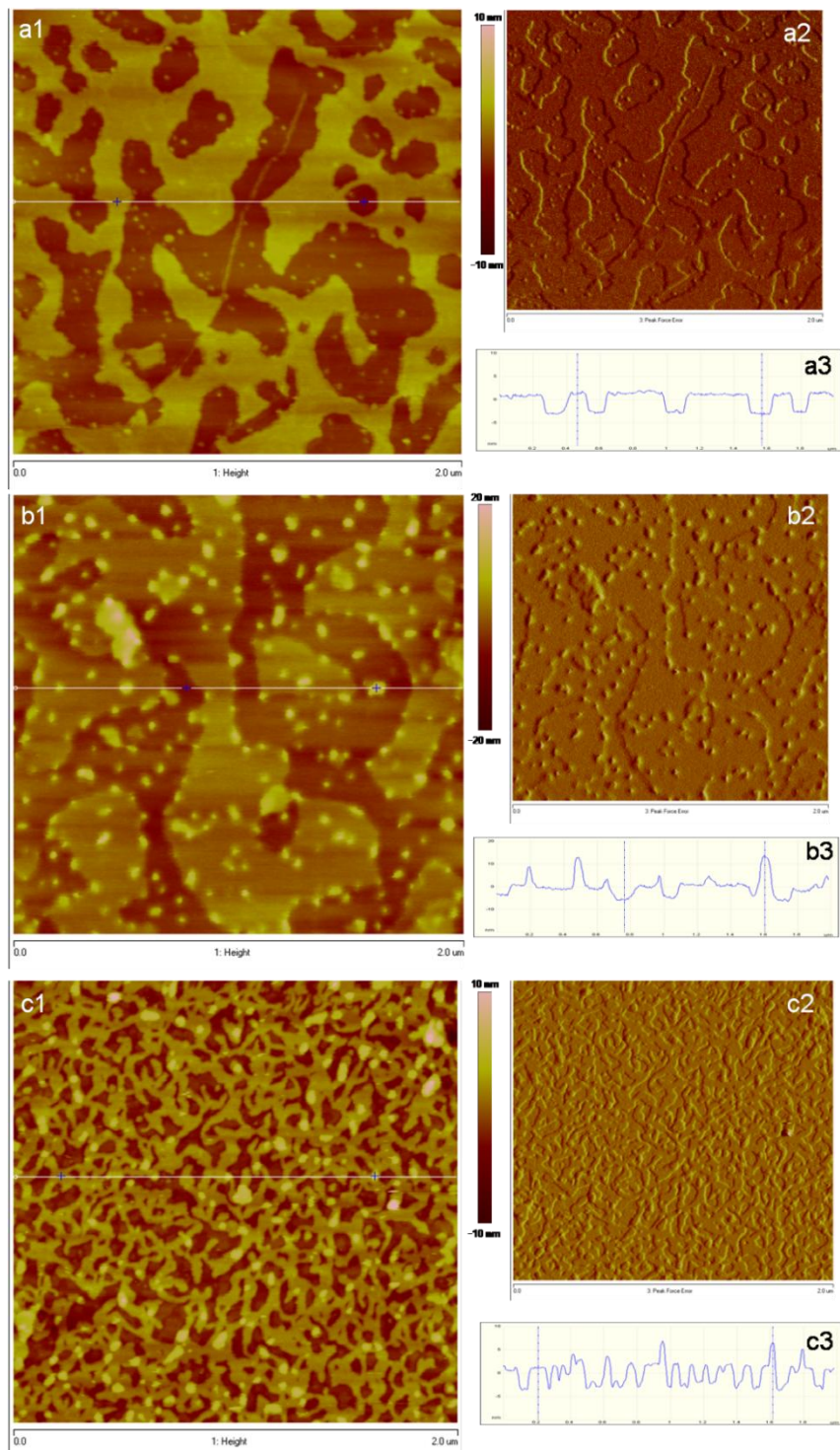


Figure 7.4 In situ AFM images of CMC (50 ppm) adsorbed onto talc basal planes in KCl solutions at pH 9 of different ionic strengths: (a) 1 mM; (b) 10 mM and (c) 100 mM.

Table 7.1 Rq surface roughness, apparent layer thickness (PTV distance) and surface coverage of adsorbed CMC (50 ppm) on talc basal planes in KCl solutions of different concentrations at pH 9.

KCl concentration (mM)	Rq (nm)	Layer thickness (nm)	CMC coverage (%)
1	1.73	4	54.1
10	3.31	4.8	53.7
100	2.19	5	72.5

Table 7.2 Contact angles of bare talc basal planes and in the presence of adsorbed CMC (50 ppm) in KCl solutions of different ionic strengths at pH 9.

KCl concentration (mM)	Contact angle (°)	
	Bare talc basal plane	Treated with CMC (50 ppm)
1		62
10	74.6±2	58
100		38

The talc basal plane is naturally hydrophobic with an initial water contact angle of 75°. After the talc basal plane was conditioned in 50 ppm CMC solution of 1 mM KCl at pH 9 for 30 minutes, the contact angle of the talc basal plane decreased to 62°. Very similar contact angle value of 58° was found after the surface treated in 10 mM KCl solution of 50 ppm CMC. When treated by 50 ppm CMC dissolved in 100 mM KCl solution, the talc basal plane became much more hydrophilic with the contact angle being reduced to 38°. This dramatic decrease in the contact angle indicates stronger interactions of CMC with the talc basal plane in CMC solutions of the high KCl concentration.

The results from the contact angle measurements correlated well with the results from in situ AFM imaging at different KCl concentrations: the higher KCl concentration, the larger the thickness and the higher the surface coverage of the adsorbed polymer layer, which make talc basal planes less hydrophobic, as shown by a significant reduction in contact angle values. This correlation suggests that the observed morphology of CMC on the mineral surface from AFM imaging under different conditions of the solution could be a good indicator to evaluate the ability of CMC to alter the wettability of mineral surfaces, which strongly affects mineral flotation.

7.3.3 CMC adsorption on talc edge surfaces

The morphologies of adsorbed CMC layer on the prepared talc edge surfaces in KCl solutions of different ionic strengths at pH 9 are shown in Figure 7.5. The R_q roughness, apparent layer thickness and surface coverage of adsorbed CMC on talc edge surfaces are given in Table 7.3. As observed in Figure 7.5, the adsorbed CMC formed spherical domains on the talc edge surface, which is totally different from the morphology of adsorbed CMC layer on talc basal planes as shown in Figure 7.4.

This anticipated difference in CMC morphology adsorbed on the talc basal plane and edge surface is most likely attributed to the different binding interactions involved between CMC and these two distinct talc surfaces. Unlike the non-polar hydrophobic talc basal plane, the talc edge surface contains abundant hydrogen bonding sites (Mg-OH and Si-OH) due to the broken bonds of Si-O-Si or Mg-O-Mg on edges, which makes the talc edge surface hydrophilic.

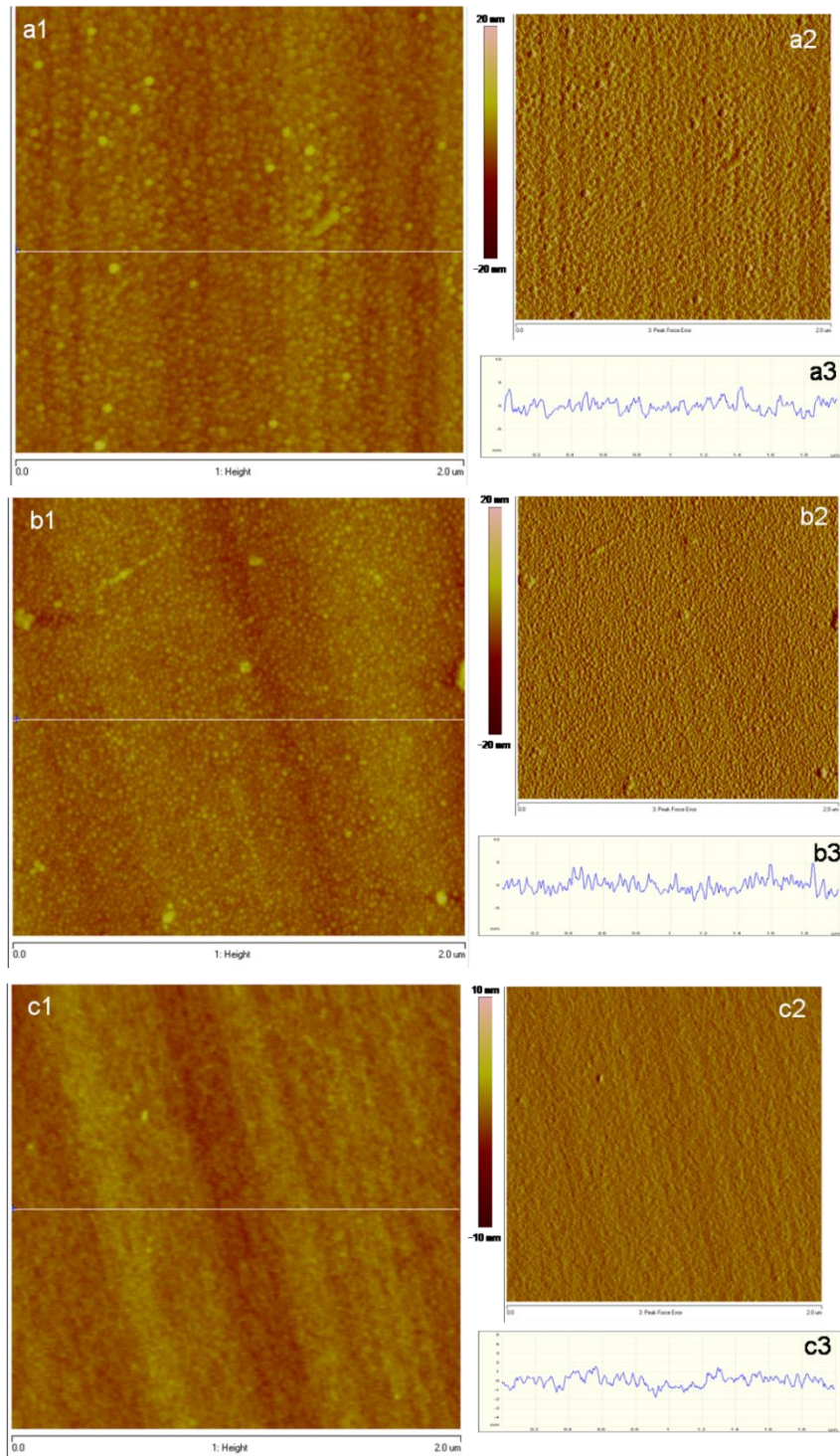


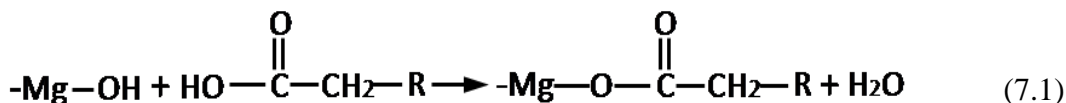
Figure 7.5 In situ AFM images of CMC (50 ppm) adsorbed onto talc edge surfaces in KCl solutions at pH 9 of different ionic strengths: (a) 1 mM; (b) 10 mM and (c) 100 mM.

Table 7.3 Rq surface roughness, apparent layer thickness (PTV distance) and surface coverage of adsorbed CMC (50 ppm) on talc edge surfaces in KCl solutions of different ionic strengths at pH 9.

KCl concentration (mM)	Rq (nm)	Layer thickness (nm)	CMC coverage (%)
1	1.36	3.27	>95
10	1.53	2.58	>95
100	0.69	less than 1.5 nm	>95

On the other hand, most polysaccharides also contain a large number of hydroxyl groups on their polymer chains, which enable themselves to interact with talc edge surfaces via hydrogen bonding interaction. This hydrogen bonding interaction is considered as an important deciding factor to choose polysaccharides as flotation depressants for a wide range of minerals [5]. As can be seen in Figure 7.2, based on the given DS of 0.7, only 7/30 hydroxyl groups on the CMC polymer chain are substituted by carboxymethyl groups (per 10 monomers). There is still quite a number of hydroxyl groups available for hydrogen bonding interactions. This strong hydrogen bonding of CMC on talc was confirmed by a number of FTIR studies [7, 9].

In addition to the hydrogen bonding interactions, the carboxyl group of CMC is also able to chemically interact with cations on many gangue mineral surfaces through the chemical complexation. The natural polysaccharides were reported to adsorb on various base metal oxides/hydroxides [26]. Similar to the reported esterification reaction between hydroxyl groups on the alumina surface and carboxylic acids [27], the carboxylic groups of CMC may interact with the magnesium ions on the talc edge surface through the following esterification reaction:



On the other hand, similar to the case of the talc basal plane, the increase in CMC adsorption on talc edge surface with increasing the ionic strength of the KCl solution is also evident. In the KCl solution of low ionic strength (1 mM), the average size of these CMC spherical domains on the talc edge surface was around 35 nm. The apparent layer thickness of adsorbed CMC on talc edge surfaces was around 3.27 nm. The presence of these small pancake domains increased the Rq surface roughness of the talc edge surface from 0.72 nm to 1.36 nm over 4 μm^2 area. As the ionic strength of the KCl solution was increased to 10 mM, the pancake domain became more compacted with the average aggregate size decreased from 35 nm to about 24.6 nm and the apparent layer thickness decreased from 3.27 nm to about 2.58 nm. The Rq surface roughness of the talc edge surface increased to 1.53 nm over 4 μm^2 area. When the concentration of the KCl solution was further increased to 100 mM, the average thickness of the adsorbed CMC layer was found to be reduced to less than 1.5 nm. The Rq surface roughness decreased to 0.88 nm over 4 μm^2 area, which is comparable to the surface roughness of bare talc edge surface. The adsorbed CMC from the KCl solution of high ionic strength appears to form a uniform layer on the talc edge surface.

7.3.4 CMC adsorption on silica surfaces

To better understand the binding mechanism of CMC on different talc surfaces, the morphology of CMC adsorbed on a hydrophilic silica surface at different KCl concentrations is also investigated by in situ AFM imaging as shown in Figure 7.6. The Rq surface roughness, apparent layer thickness and surface coverage of adsorbed CMC on the silica wafer surface are listed in Table 7.4.

The silica surface has identical chemical composition and surface roughness as talc basal planes, with only difference being hydrophilic for the silica wafer in contrast to being hydrophobic for talc basal planes. Compared to the morphology of CMC adsorbed on the talc basal plane, totally different morphology of CMC adsorbed on the silica surface was observed. These observed differences in adsorption and conformation of CMC on the two surfaces can be attributed to the totally different wettability characteristics of these two surfaces, and hence different binding mechanisms and their impact on the morphology of adsorbed CMC. Though both surfaces have similar chemical composition and surface roughness, it is believed that there exists an exclusion zone between siloxane groups (-Si-O-Si-) on the talc basal plane and water molecules of the solution due to the absence of polarity of talc basal planes [21]. In contrast, water molecules can be tightly bonded with polar groups (Si-OH) on the silica surface. The CMC molecules tend to spread over the talc basal plane in two dimensional network by strong hydrophobic interaction via their hydrocarbon backbone and methyl group, while this hydrophobic interaction does not exist on the silica surface. The strong hydrophobic interaction in the binding of CMC on talc basal planes was shown clearly.

On the other hand, although both silica and talc edge surfaces are hydrophilic due to similar metal polar hydroxyl groups (M-OH), the morphology of CMC adsorbed on the silica surface is also different from that on the talc edge surface under the same solution conditions.

As shown in Figure 7.6, at the lowest ionic strength of the KCl solution (1 mM) at pH 9, individual CMC pancakes of around 58.5 nm in diameter were formed on the silica wafer surface with the apparent CMC layer thickness of 2.27 nm. The

Rq roughness of the silica surface was increased from 0.17 nm to 0.51 nm over 4 μm^2 area. As the KCl concentration was increased to 10 mM at the same CMC concentration and pH, the pancakes became smaller with reduced average domain size about 36.7 nm and the apparent layer thickness of around 2.43 nm. The Rq surface roughness of the silica surface was increased to 1.27 nm over 4 μm^2 area. When the KCl concentration increased to 100 mM, more dense packing of CMC domains were observed with a decrease in average size to about 28.7 nm and the apparent layer thickness of around 2.79 nm.

Different hydroxyl groups have different basicity, which depends on the valence state, ionic radii and coordination numbers of the metal ions on the surface group. Normally, the higher the basicity of the mineral $-\text{OH}$ surface group, the stronger will be their interactions with polysaccharides, which can result in higher surface coverage of polysaccharides on mineral surfaces. As reported [27], a high reactivity of the Al-OH surface group toward carboxylic acids was found as compared to a hydrated silica surface. Compared with aluminum oxides/hydroxides, the magnesium oxides/hydroxides have an even higher IEP [28]. Therefore, due to its higher basicity, the Mg-OH surface group on the talc edge surface is expected to bond with the carboxylic group stronger than Al-OH surface group does, which may result in a stronger adsorption of CMC on the talc edge surface as compared to the silica surface. Strong adsorption of polysaccharides was also reported on the natural galena, as lead oxides/hydroxides also have high IEP [3].

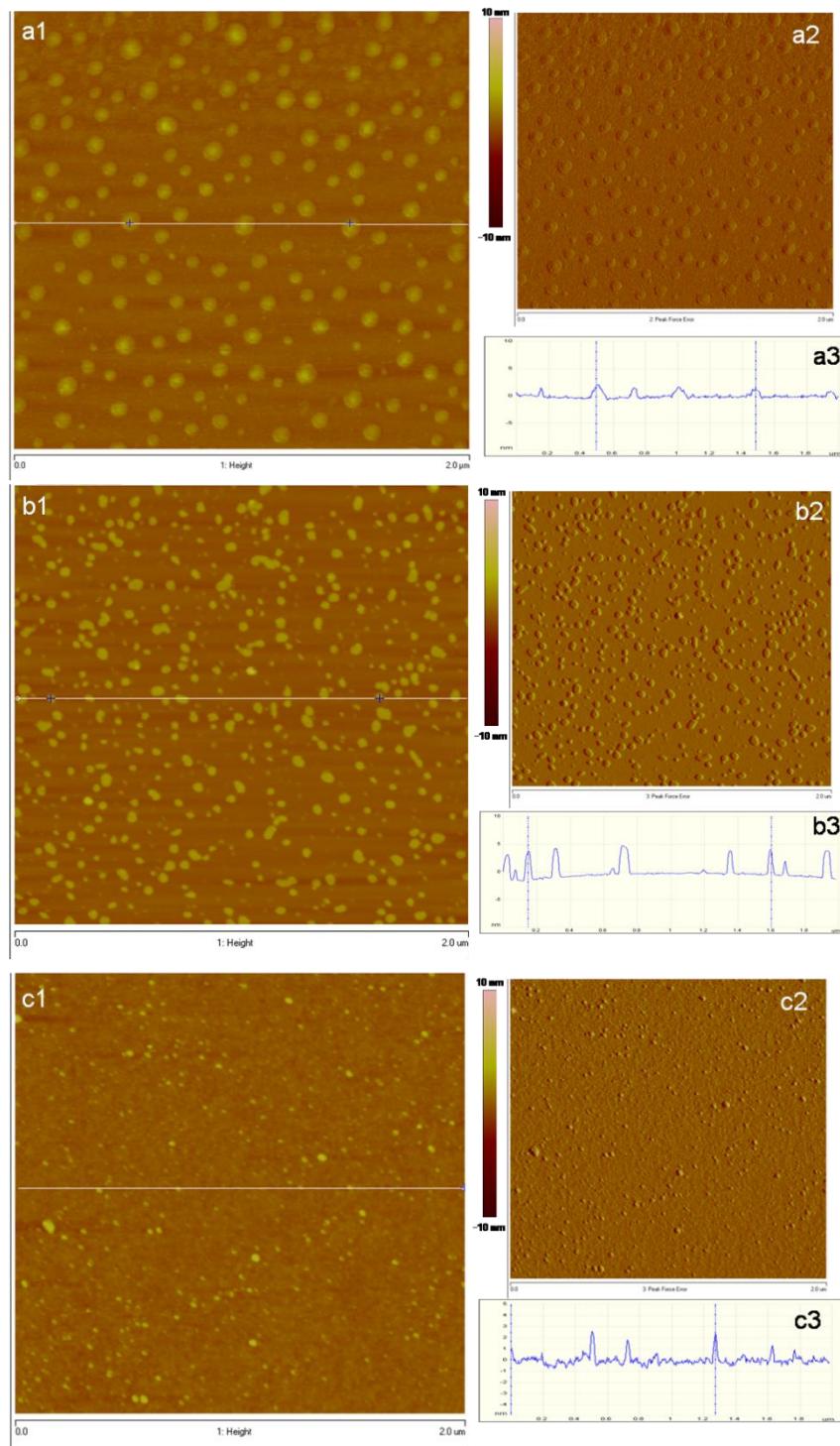


Figure 7.6 In situ AFM images of CMC (50 ppm) adsorbed onto silica surfaces in KCl solutions at pH 9 of different ionic strengths: (a) 1 mM; (b) 10 mM and (c) 100 mM.

Table 7.4 Rq surface roughness, apparent layer thickness (PTV distance) and surface coverage of adsorbed CMC (50 ppm) on silica surfaces in KCl solutions of different ionic strengths at pH 9.

KCl concentration (mM)	Rq (nm)	Layer thickness (nm)	CMC coverage (%)
1	0.51	2.27	24.5
10	1.27	2.43	35
100	2.19	2.79	19.3

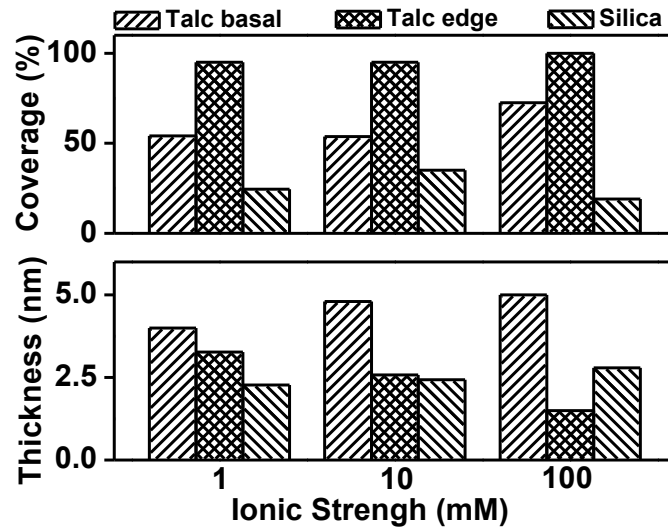


Figure 7.7 Summary of surface coverage and apparent layer thickness of adsorbed CMC on different surfaces in KCl solutions of different ionic strengths at pH 9.

Table 7.5 Summary of binding mechanisms of different surfaces (- Hinders, + Driving force).

Binding mechanism	Talc basal plane	Talc edge surface	Silica
Electrostatic	--	-	--
H-bonding	+	++	+
Hydrophobic	++	/	/
Chemical complex	/	+++	/

In order to facilitate comparison, the summary of the surface coverage and apparent layer thickness of adsorbed CMC on different talc surfaces and silica in KCl solutions of different concentrations at pH 9 are shown in Figure 7.7 and the possible binding mechanisms for each surface are summarized in Table 7.5. CMC interaction with the talc basal plane is dominated by hydrophobic interactions while bonding with the talc edge surface is mainly through chemical complexation reaction and hydrogen bonding. Compare to the silica surface, both the talc basal plane and edge surface have stronger binding with CMC, therefore, the effect of ionic strength of the solution on CMC adsorption on these mineral surfaces becomes less significant.

7.4 Summary

The adsorption of CMC on distinct talc basal planes and edge surfaces in KCl solutions at pH 9 of various ionic strengths is investigated by in situ AFM imaging technique. The morphology of adsorbed CMC on different talc surfaces is significantly different, due to different binding mechanisms involved. CMC interaction with the talc basal plane is dominated by hydrophobic interactions while bonding with the talc edge surface is mainly through chemical complexation reaction and hydrogen bonding. The amount of CMC adsorbed on both talc basal planes and edge surfaces increased upon increasing the ionic strength of the KCl solution. The methodology developed in this chapter opens the door to probe polymer adsorption on anisotropic phyllosilicate surfaces, which can help us better understand the mechanism of polymer adsorption on specific minerals surfaces. Practically, it may help us solve some problems related to selectivity of polymer adsorption in industrial processing and design novel synthetic polymers for mineral processing.

7.5 References

- [1] Pugh, R. J., 1989, "Macromolecular Organic Depressants in Sulphide flotation-a Review, 1. Principles, Types and Applications," *International Journal of Mineral Processing*, 25(1-2) pp. 101-130.
- [2] Laskowski, J. S., 2010, "Rheological Properties of Aqueous Suspensions of Anisotropic Minerals," 8th UBC-McGill-UA Symposium, M. Pawlik, ed. Vancouver, BC, Canada.
- [3] Liu, Q., Zhang, Y., Laskowski, J. S., 2000, "The Adsorption of Polysaccharides onto Mineral Surfaces: An Acid/Base Interaction," *International Journal of Mineral Processing*, 60(3-4) pp. 229-245.
- [4] Pawlik, M., Laskowski, J. S., Ansari, A., 2003, "Effect of Carboxymethyl Cellulose and Ionic Strength on Stability of Mineral Suspensions in Potash Ore Flotation Systems," *Journal of Colloid and Interface Science*, 260(2) pp. 251-258.
- [5] Khraisheh, M., Holland, C., Creany, C., Harris, P., Parolis, L., 2005, "Effect of Molecular Weight and Concentration on the Adsorption of CMC Onto Talc at Different Ionic Strengths," *International Journal of Mineral Processing*, 75(3-4) pp. 197-206.
- [6] Beaussart, A., Mierczynska-Vasilev, A., Beattie, D. A., 2010, "Evolution of Carboxymethyl Cellulose Layer Morphology on Hydrophobic Mineral Surfaces: Variation of Polymer Concentration and Ionic Strength," *Journal of Colloid and Interface Science*, 346(2) pp. 303-310.
- [7] Wang, J., and Somasundaran, P., 2005, "Adsorption and Conformation of Carboxymethyl Cellulose at Solid-Liquid Interfaces using Spectroscopic, AFM and Allied Techniques," *Journal of Colloid and Interface Science*, 291(1) pp. 75-83.
- [8] Cuba-Chiem, L. T., Huynh, L., Ralston, J., 2008, "In Situ Particle Film ATR FTIR Spectroscopy of Carboxymethyl Cellulose Adsorption on Talc: Binding Mechanism, pH Effects, and Adsorption Kinetics," *Langmuir*, 24(15) pp. 8036-8044.
- [9] Cuba-Chiem, L. T., Huynh, L., Ralston, J., 2008, "In Situ Particle Film ATR-FTIR Studies of CMC Adsorption on Talc: The Effect of Ionic Strength and Multivalent Metal Ions," *Minerals Engineering*, 21(12-14) pp. 1013-1019.

- [10] Bacchin, P., Bonino, J., Martin, F., 2006, "Surface Pre-Coating of Talc Particles by Carboxyl Methyl Cellulose Adsorption: Study of Adsorption and Consequences on Surface Properties and Settling Rate," *Colloids and Surfaces A-Physicochemical and Engineering Aspects*, 272(3) pp. 211-219.
- [11] Burdukova, E., Bradshaw, D. J., Laskowski, J. S., 2007, "Effect of CMC and pH on the Rheology of Suspensions of Isotropic and Anisotropic Minerals," *Canadian Metallurgical Quarterly*, 46(3) pp. 273-278.
- [12] Morris, G., Fornasiero, D., Ralston, J., 2002, "Polymer Depressants at the Talc-Water Interface: Adsorption Isotherm, Microflotation and Electrokinetic Studies," *International Journal of Mineral Processing*, 67(1-4) pp. 211-227.
- [13] Mierczynska-Vasilev, A., Beattie, D. A., 2010, "Adsorption of Tailored Carboxymethyl Cellulose Polymers on Talc and Chalcopyrite: Correlation between Coverage, Wettability, and Flotation," *Minerals Engineering*, 23(11-13) pp. 985-993.
- [14] Beaussart, A., Mierczynska-Vasilev, A. M., Harmer, S. L., Beattie, D. A., 2011, "The Role of Mineral Surface Chemistry in Modified Dextrin Adsorption," *Journal of Colloid and Interface Science*, 357(2) pp. 510-520.
- [15] Kagawa, G. B., Froebe, S., Huynh, L., Ralston, J., Bremmell, K., 2005, "Morphology of Adsorbed Polymers and Solid Surface Wettability," *Langmuir*, 21(10) pp. 4695-4704.
- [16] Beaussart, A., Parkinson, L., Mierczynska-Vasilev, A., Beattie, D. A., 2012, "Adsorption of Modified Dextrins on Molybdenite: AFM Imaging, Contact Angle, and Flotation Studies," *Journal of Colloid and Interface Science*, 368(1) pp. 608-615.
- [17] Beaussart, A., Mierczynska-Vasilev, A., Beattie, D. A., 2009, "Adsorption of Dextrin on Hydrophobic Minerals," *Langmuir*, 25(17) pp. 9913-9921.
- [18] Mierczynska-Vasilev, A., Ralston, J., Beattie, D. A., 2008, "Adsorption of Modified Dextrins on Talc: Effect of Surface Coverage and Hydration Water on Hydrophobicity Reduction," *Langmuir*, 24(12) pp. 6121-6127.
- [19] Beattie, D. A., Huynh, L., Mierczynska-Vasilev, A., Myllynen, M., Flatt, J., 2007, "Effect of Modified Dextrins on the Depression of Talc and their Selectivity in Sulphide Mineral Flotation: Adsorption Isotherms, AFM

- Imaging and Flotation Studies," *Canadian Metallurgical Quarterly*, 46(3) pp. 349-358.
- [20] Steenberg, E., Harris, P., 1984, "Adsorption of Carboxymethyl cellulose, Guar Gum, and Starch Onto Talc, Sulfides, Oxides, and Salt-Type Minerals," *South African Journal of Chemistry*, 37(3) pp. 85-90.
- [21] Du, H., Miller, J. D., 2007, "A Molecular Dynamics Simulation Study of Water Structure and Adsorption States at Talc Surfaces," *International Journal of Mineral Processing*, 84(1-4) pp. 172-184.
- [22] Schneider, C. A., Rasband, W. S., Eliceiri, K. W., 2012, "NIH Image to Image J: 25 Years of Image Analysis," *Nature Methods*, 9(7) pp. 671-675.
- [23] Chowdhury, F., Neale, S., 1963, "Acid Behaviour of Carboxylic derivatives of Cellulose.1. Carboxymethyl Cellulose," *Journal of Polymer Science: Part A*, 1pp. 2881-2891.
- [24] Shortridge, P., Harris, P., Bradshaw, D., 2000, "The Effect of Chemical Composition and Molecular Weight of Polysaccharide Depressants on the flotation of Talc," *International Journal of Mineral Processing*, 59(3) pp. 215-224.
- [25] Kagawa, G. B., Huynh, L., Ralston, J., Bremmell, K., 2006, "The Influence of Polymer Structure and Morphology on Talc Wettability," *Langmuir*, 22(7) pp. 3221-3227.
- [26] Laskowski, J. S., Liu, Q., O'Connor, C. T., 2007, "Current Understanding of the Mechanism of Polysaccharide Adsorption at the Mineral/Aqueous Solution Interface," *International Journal of Mineral Processing*, 84(1-4) pp. 59-68.
- [27] Karaman, M. E., Antelmi, D. A., Pashley, R. M., 2001, "The Production of Stable Hydrophobic Surfaces by the Adsorption of Hydrocarbon and Fluorocarbon Carboxylic Acids onto Alumina Substrates," *Colloids and Surfaces A: Physicochemical and Engineering Aspects*, 182(1-3) pp. 285-298.
- [28] Parks, G. A., 1965, "The Isoelectric Points of Solid Oxides, Solid Hydroxides, and Aqueous Hydroxo Complex Systems," *Chemical Reviews*, 65(2) pp. 177-198.

Chapter 8

Summary

8.1 General conclusions

This dissertation focuses on investigating anisotropic surface properties of phyllosilicates. In particular, systematic studies on the impact of pH and divalent cations in aqueous solutions on surface charging characteristic of two typical 2:1 (TOT) layer phyllosilicates (talc and muscovite) are presented. The anisotropic surface charge property of phyllosilicate suspensions related to their rheological behaviour is discussed. Also, some preliminary results on polymer adsorption on different talc surfaces are included.

In Chapter 3, the methodology to study anisotropic properties of phyllosilicates was established. The ultramicrotome cutting technique was employed to prepare molecularly smooth edge surfaces of talc and muscovite, which allowed direct measurement of interactions between AMF tips and prepared phyllosilicate surfaces in various electrolyte solutions. Commercial AFM silicon nitride tips instead of micron size probes were chosen in AFM force measurements to quantitatively evaluate surface charge properties of prepared surfaces. A theoretical model based on the geometry of this tip was used to fit the measured force profiles to the classical DLVO theory at different BC, which allowed direct determination of the Stern potentials of different phyllosilicate surfaces.

In Chapter 4, colloidal interaction forces between AFM tips and specific phyllosilicate surfaces as a function of solution pH were measured. The basal plane of both muscovite and talc were found to carry a permanent negative charge,

while the charge on their edge surfaces is highly pH-dependent. Although both talc and muscovite are platy 2:1 phyllosilicate minerals, the stern potential of muscovite basal planes is much more negative than that of talc basal planes due to its high degree of isomorphous substitution. The charges on edge surfaces of muscovite and talc basal planes exhibit different responses to solution pH. The observed differences in Stern potentials of basal planes and edge surfaces for both talc and muscovite are closely related to their crystal structure and ionization characteristics. The protonation reactivity and the contribution of each surface group to the surface charging behaviour are modeled using their protonation constants.

In Chapter 5, the effects of the concentration of two divalent cations: Mg^{2+} and Ca^{2+} on Stern potentials of different phyllosilicate mineral surfaces were investigated. Different responses of the Stern potential of the basal plane and the edge surface to the divalent cation addition in solutions are attributed to the different surface charging mechanisms and binding mechanisms of each type of surfaces with different divalent cations.

In Chapter 6, The Stern potential values of talc basal planes and edge surfaces from fitting of measured interaction force profiles in 1 mM KCl solution at different pH values (3.2-9) were obtained. Based on these fitted Stern potential values, interaction energies of various associations between talc surfaces, (basal plane-basal plane, edge-edge and basal plane-edge) were calculated. The attractive interaction between talc basal planes and edge surfaces was found to dominate the rheological behaviour of talc suspensions and the highest probability of card-house formation between talc edge surfaces and basal planes was found to correspond well with the measured highest yield stress of talc suspensions.

In Chapter 7, some preliminary results on CMC adsorption on different talc surfaces were presented.

In conclusion, this work clearly demonstrates the need for study on anisotropic surface characteristics if one wants to improve the understanding of colloidal behaviours of phyllosilicate minerals and hence better control their process performance.

Moreover, the methodology developed in this study opens the door to probe interactions of various mineral surfaces with process aids under various physicochemical conditions of the system, an extremely important subject in nano technology and resource engineering. The method of preparation of the phyllosilicate edge surface described in this study can be extended to other minerals or natural resources such as coal. For instance, the work of applying ultramicrotome technique to study anisotropic properties of chlorite surfaces, in collaboration with Professor Jan D. Miller's research group at the University of Utah is not included in this thesis but can be found elsewhere: *Yin, X., Yan, L., Liu, J., Xu, Z., Miller, J. D., 2013, "Anisotropic Surface Charging of Chlorite Surfaces", Clays and Clay Minerals, In press.*

8.2 Contributions to original knowledge

1. An ultramicrotome cutting procedure was developed to prepare molecularly smooth edge surfaces of phyllosilicates. More accurate results can be obtained without incurring complex finite element analysis to incorporate the effect of surface roughness in AFM interaction forces fitting.
2. The colloidal probe technique of AFM was proved to be a powerful tool to study the interactions between AFM tips and well-defined basal planes and

edge surfaces of phyllosilicates in aqueous solution.

3. A theoretical model based on the geometry of AFM tip was developed to fit the measured force profiles to the classical DLVO theory for mixed BC, which allows direct determination of Stern potentials of different phyllosilicate surfaces for the specific case at proper BC.
4. To the best of my knowledge, it is the first time that the effect of pH and the concentration of two divalent cations (Mg^{2+} and Ca^{2+}) in solutions on the Stern potential of different phyllosilicate surfaces were systematically and quantitatively investigated by direct force measurement using AFM.
5. Interaction energies of various associations between talc surfaces were calculated using the AFM-derived Stern potential values of talc basal planes and edge surfaces. The rheological behaviour of talc suspensions was better interpreted in terms of considering anisotropic surface charge characteristics of the talc particle, instead of blindly treating it as isotropic.

8.3 Recommendations for further work

It is my hope that the developed methodology and obtained results in this dissertation are interesting to those in the field of investigating the surface property of phyllosilicates, in particular of real clays. Should that be the case, I would like to suggest:

1. Develop a suitable technique to prepare a smooth edge surface for other phyllosilicate particles such as kaolinite which lacks of cleavage basal planes.
2. Probe interactions of polymers with well-defined basal planes and edge surfaces of phyllosilicates under various physicochemical conditions at a single molecule resolution using single molecule force spectroscopy.

Appendix A

Deposition of phyllosilicate particle suspensions

Procedure of orderly deposition of phyllosilicate suspensions

- (1) Suspensions of phyllosilicate particles are prepared at high concentration (6g/L).
- (2) After stirring and sonication, the pH of suspensions is adjusted to 10.
- (3) Suspensions are centrifuged at 1200 and 2400 rpm for 3 minutes successively, then 3000 rpm for 8 minutes.
- (4) A few drops of suspensions are spread over a sheet of cleaved muscovite basal plane which is put on a hot plate for a few seconds to quickly evaporate the water.
- (5) The muscovite sheet coated with phyllosilicate particles is flushed gently by MiliQ water to remove any loosely bound particles and then dried with nitrogen gas.

Then the coated sheet can be embedded in silicon mold filled with resin for further ultramicrotome cutting as shown in Figure A.1.

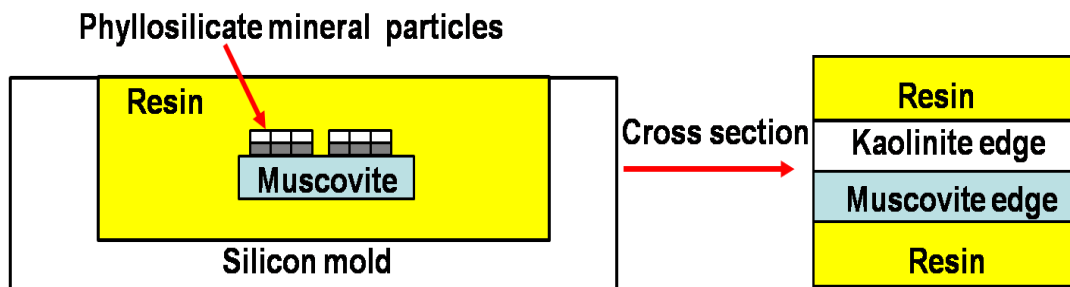


Figure A.1 Schematics of a muscovite sheet coated with phyllosilicate particles for ultramicrotome cutting and the proposed view of the cross section of the cutting result.

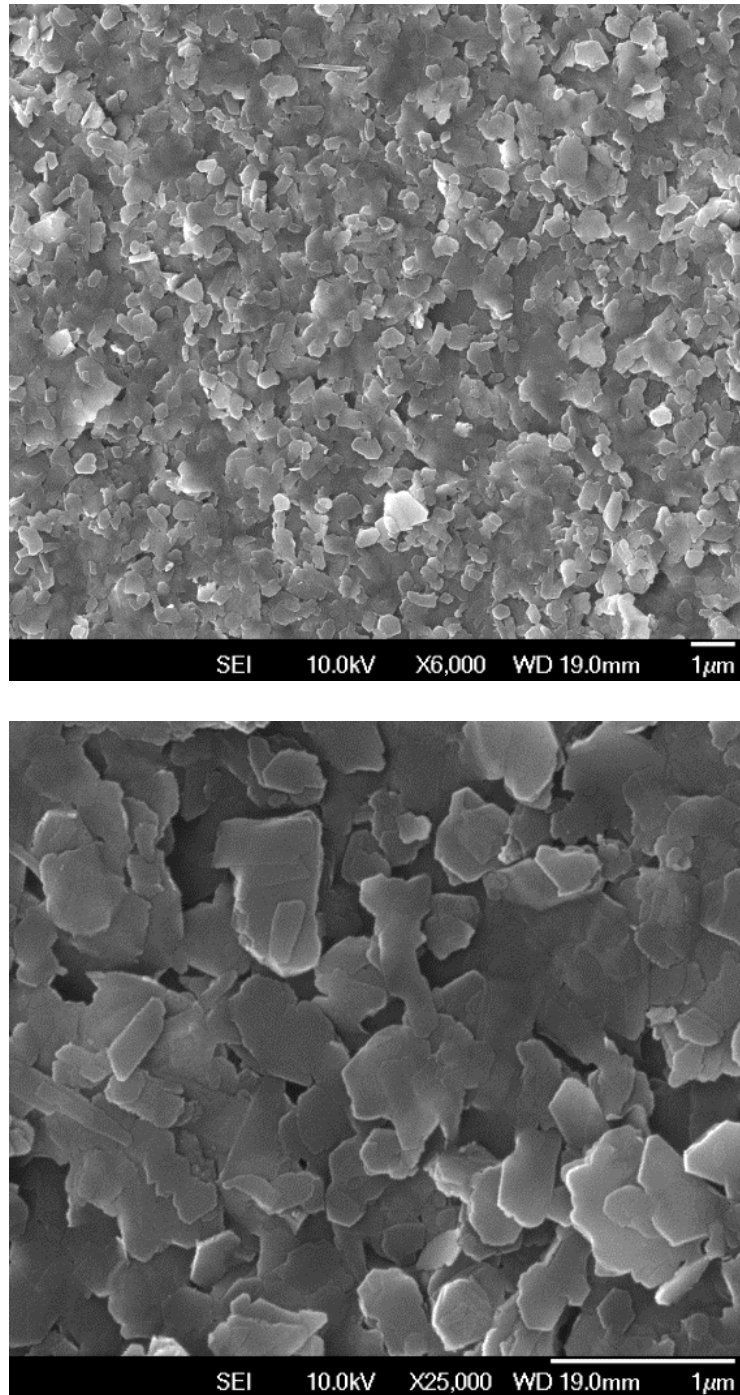


Figure A.2 SEM images of kaolinite particles deposited on muscovite substrate: (a) large area at low resolution and (b) small area at high resolution.

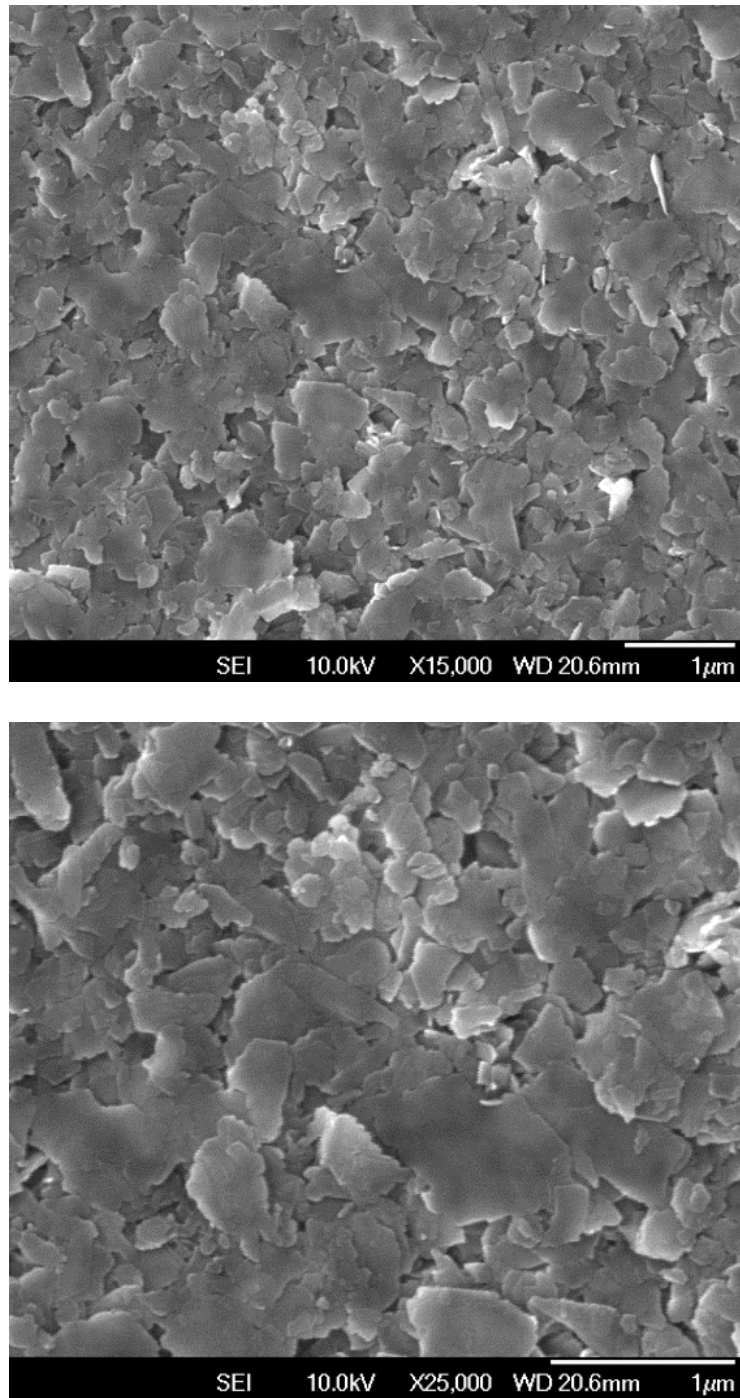


Figure A.3 SEM images of illite particles deposited on muscovite substrate: (a) large area at low resolution and (b) small area at high resolution.

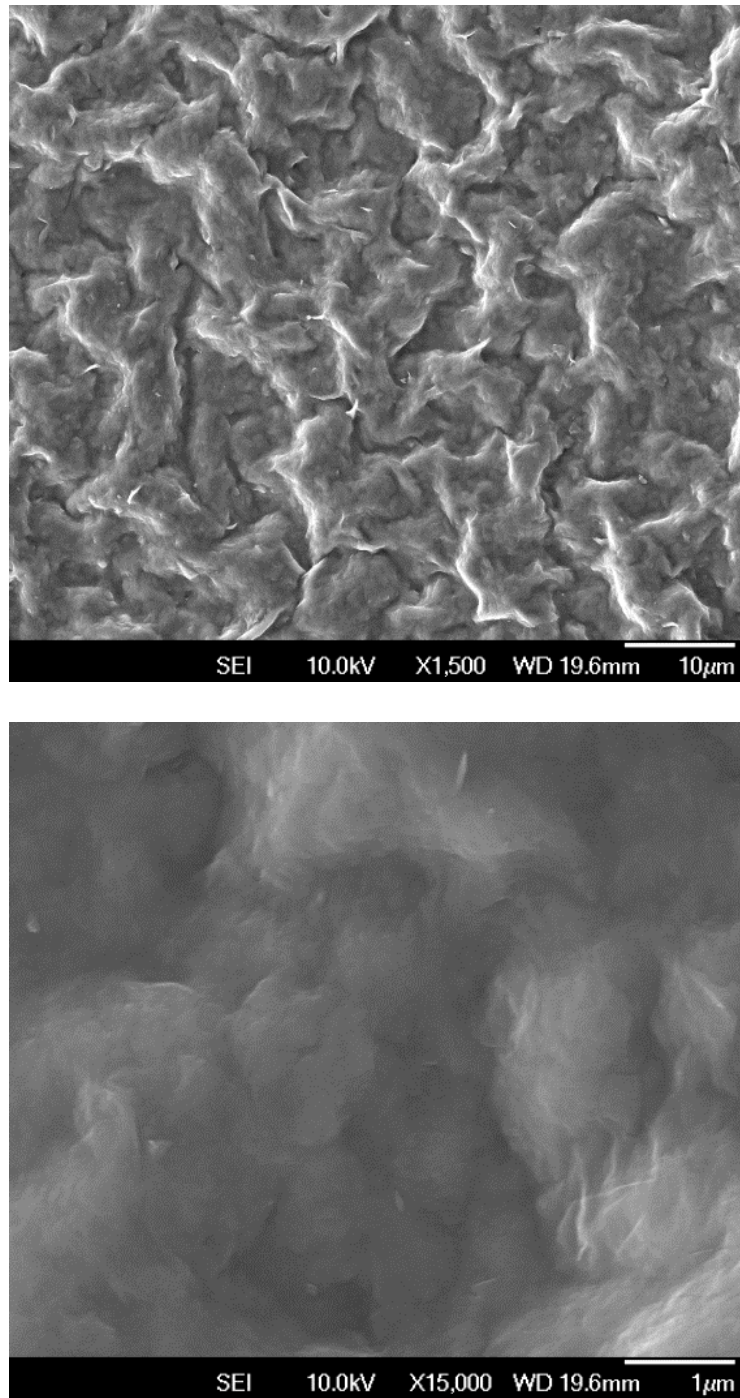


Figure A.4 SEM images of montmorillonite particles deposited on muscovite substrate: (a) large area at low resolution and (b) small area at high resolution.

Appendix B

Estimation of surface energy of different phyllosilicate surfaces

B.1 Good & Van Oss model

In the Good & Van Oss model, the surface energy can be written as [1, 2]:

$$\gamma = \gamma^{LW} + 2\sqrt{\gamma^+\gamma^-} \quad (\text{B.1})$$

where γ is the surface energy, γ^{LW} is the Lifshitz-Van der Waals interactions component and γ^+ and γ^- are Lewis acid-base components .

The relation between liquid contact angle (θ) and surface energy components of solid surface and liquid can be given by:

$$\gamma_L(1 + \cos\theta) = 2\left(\sqrt{\gamma_S^{LW}\gamma_L^{LW}} + \sqrt{\gamma_S^+\gamma_L^-} + 2\sqrt{\gamma_L^+\gamma_S^-}\right) \quad (\text{B.2})$$

where L and S represent the liquid and solid, respectively.

B.2 Three-probe-liquid contact angle measurement

The surface energy components of the solid (γ_S^{LW} , γ_S^+ and γ_S^-) were derived using the sessile drop method based on the contact angles of the three probe liquids, including one nonpolar (diiodomethane) and two polar (water and glycerol) liquids. The surface tension components were taken from literature [1-3].

Thus, the energy components of phyllosilicate surfaces can be determined by:

$$\begin{bmatrix} \gamma_s^d \\ \gamma_s^+ \\ \gamma_s^- \end{bmatrix} = \left\{ 2 \left[\begin{bmatrix} \sqrt{\gamma_{L1}^d} & \sqrt{\gamma_{L1}^-} & \sqrt{\gamma_{L3}^-} \\ \sqrt{\gamma_{L2}^d} & \sqrt{\gamma_{L2}^-} & \sqrt{\gamma_{L3}^-} \\ \sqrt{\gamma_{L3}^d} & \sqrt{\gamma_{L2}^-} & \sqrt{\gamma_{L3}^-} \end{bmatrix} \right]^{-1} \begin{bmatrix} \gamma_{L1}[\cos \theta_1 + 1] \\ \gamma_{L2}[\cos \theta_2 + 1] \\ \gamma_{L3}[\cos \theta_3 + 1] \end{bmatrix} \right\}^2 \quad (\text{B.3})$$

where L1, L2 and L3 denote the three different probe liquids, respectively.

Table B.1 Three probe liquids for measuring the surface energy of phyllosilicates.

Liquid	γ_L^{LW}	γ_L^+	γ_L^-	γ_L
Water	21.8	25.5	25.5	72.8
Glycerol	34	3.92	57.4	64
Diiodomethane	50.8	0	0	50.8

Table B.2 Contact angles of three probe liquids on different surfaces.

Surface	Contact angle θ (°)		
	Water	Glycerol	Diiodomethane
Muscovite basal	0	27.0	43.8
Talc basal	75.4	51.3	44.2
Silicon nitride tip	26.0	34.2	42.3
Silica	35.7	32.0	45.8

Table B.3 Surface energy of different surfaces.

Surface	Surface energy parameters (mJ/m ²)			
	γ^{LW}	γ^+	γ^-	γ
Muscovite basal	37.7	1.6	56	56.5
Talc basal	37.4	2.8	2.8	43.1
Silicon nitride tip	38.5	1.2	46.8	53.7
Silica	36.6	2.4	34.9	55

B.3 References

- [1] Van Oss, C. J., 1993, "Acid-Base Interfacial Interactions in Aqueous Media," *Colloids and Surfaces A: Physicochemical and Engineering Aspects*, 78 pp. 1-49.
- [2] Van Oss, C. J., Good, R. J., Chaudhury, M. K., 1986, "The Role of Van Der Waals Forces and Hydrogen Bonds in "Hydrophobic Interactions" between Biopolymers and Low Energy Surfaces," *Journal of Colloid and Interface Science*, 111(2) pp. 378-390.
- [3] Volpe, C. D., Siboni, S., 1997, "Some Reflections on Acid-Base Solid Surface Free Energy Theories," *Journal of Colloid and Interface Science*, 195(1) pp. 121-13.

Appendix C

AFM images of CMC adsorbed onto muscovite basal planes

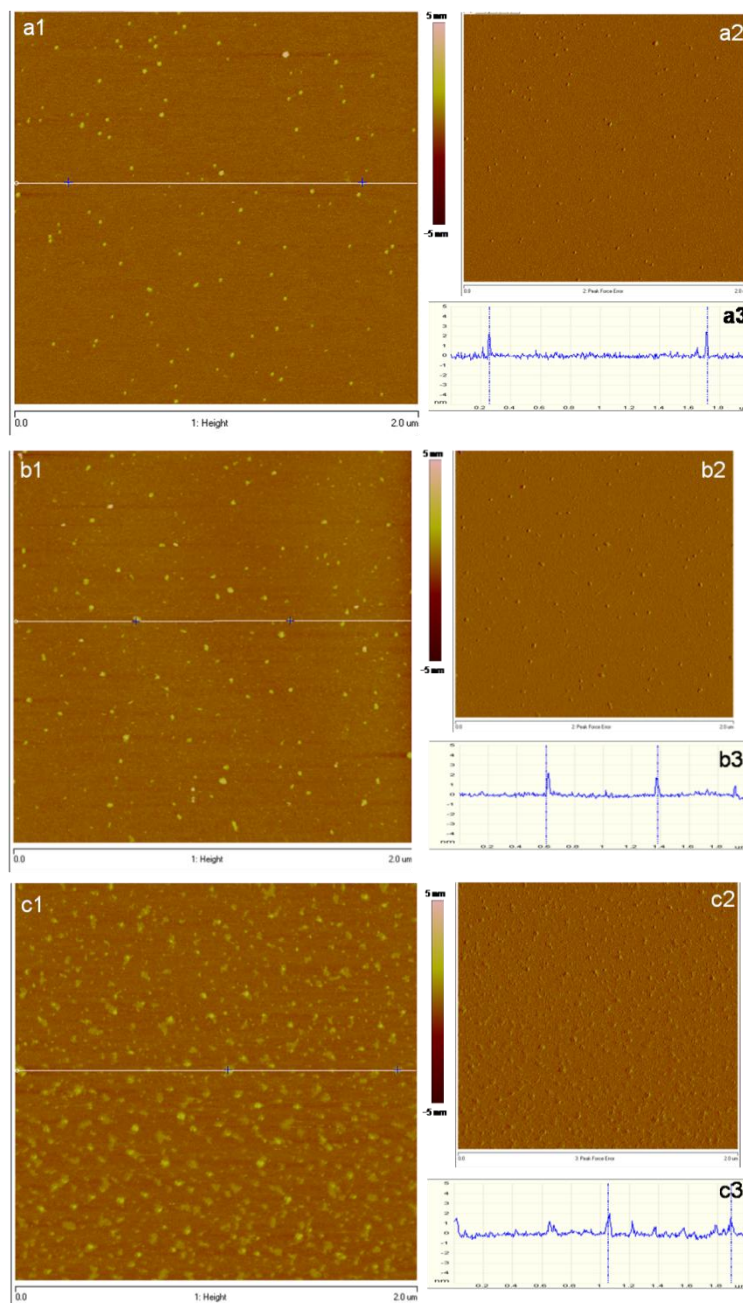


Figure C.1 In situ AFM images of CMC (50 ppm) adsorbed onto muscovite basal planes in KCl solutions at pH 9 of different ionic strengths: (a) 1 mM; (b) 10 mM and (c) 100 mM

Table C.1 Rq surface roughness, apparent layer thickness (PTV distance) and surface coverage of adsorbed CMC (50 ppm) on muscovite basal planes in KCl solutions of different ionic strengths at pH 9.

KCl concentration (mM)	Rq (nm)	Layer thickness (nm)	CMC coverage (%)
1	0.23	3.05	2.3
10	0.27	2.82	4.7
100	0.31	1.57	15.5